Automated path planning for additive friction stir deposition

A Dissertation Presented for the

Doctor of Philosophy

Degree

The University of Tennessee, Knoxville

Joshua Phillip Kincaid

May 2025

Copyright © 2025 by Joshua Kincaid
All rights reserved

DEDICATION

This dissertation is dedicated to my loving wife Anna.

ACKNOWLEDGEMENTS

First, I would like to thank my friends and family for their continuing support and encouragement. Next to my committee members, Dr. Bradley Jared, Dr. Tony Shi, and Dr. Michael Borish, for all of the helpful advice and feedback along this journey. Also, to all of my fellow lab mates, specifically Lauren Miller, Eli Charles, Brad Edwards, and Rob Patterson who have helped me with much work in AFSD.

Others I would like to specifically mention are Josh McQuaid and Jeff Burdick. Josh for his constant mentorship and to Jeff for validating and making use of my research. I also would like to thank Devon Goodspeed and Cole Franz for helping with some last-minute testing. Lastly, I would like to thank Dr. Tony Schmitz for helping and enabling me to pursue many research avenues and for opening many doors of opportunity. As well as growing me as a researcher, a learner, and as an individual. I could not have arrived here without your help.

ABSTRACT

Additive friction stir deposition (AFSD) is a solid-state metal additive manufacturing (AM) technology, which is favored for producing near net shape, fully dense parts at a relatively high deposition rate. Although path planning methods and software currently exist for other AM processes, such as fused filament fabrication for polymers and powder bed fusion for metals, no current path planning software supports AFSD path planning. This is because in AFSD when parallel tracks are deposited the tool should be allowed to overlap the prior track, reprocessing that material into the current track and ensuring that the deposit remains fully dense and that the neighboring tracks are fully bonded. However, process feed rates must be adjusted to prevent both an overfed condition which produces excess squeeze flash and increases process reactive forces while avoiding an underfed condition which can produce galling, voids, and/or a decrease in effective layer height. These defects when introduced often cause build failure. Currently, path planning and the subsequent computer code generation to command the machine motions for AFSD are completed manually. This approach is both time-consuming, often taking longer than the material deposition time, and prone to error. Additionally, the manual approach can limit geometric complexity, which sacrifices benefits often provided by AM. To address this issue, this dissertation presents a volume-based approach to compensating process parameters to varying overlap conditions in AFSD. Allowing for the creation of an automated path planning framework which also described and subsequently demonstrated.

TABLE OF CONTENTS

CHAPTER 1: INTRODUCTION AND GENERAL INFORMATION 1

Dissertation summary 2

Intellectual merit 2

Broader impacts 3

Dissertation organization 3

Background and motivation 4

AFSD process background and introduction 4

CHAPTER 2: LITERATURE REVIEW 7

Introduction 8

AFSD 8

Friction stir welding background 8

AFSD material studies 8

AFSD process studies 9

AFSD modeling studies 10

Path planning 10

Methods for approximating geometry 11

Path planning optimization 13

Originality 13

CHAPTER 3: OVERLAPPING TRACK FEED RATE COMPENSATION METHODS FOR AFSD 17

Manuscript introduction 18

Manuscript attributions: 18

Feed rate selection in additive friction stir deposition: compensation for overlapping tracks 18

Introduction 19

Methods 21

Experimentation 23

Results 26

Conclusion 40

Z-lift compensation **41**
Introduction **41**
Testing and results **41**
Conclusions **44**
Curvilinear overlap methods: **55**
Method **55**
Validation **58**
Conclusion and future work **61**
CHAPTER 4: ROBUST LEAST SQUARES ARC FITTING METHOD OF ORDERED POINT FOR PATH PLANNING IN ADDITIVE MANUFACTURING **62**
Introduction **63**
Manuscript author contributions: **63**
Robust least squares arc fitting method of ordered point for path planning in additive manufacturing **63**
Introduction: **64**
Methods: **66**
Results and discussion: **74**
Conclusions: **86**
CHAPTER 5: AUTOMATED AFSD OVERLAP COMPENSATION ALGORITHM FOR AM PATH PLANNING **87**
Introduction **88**
Method **89**
Method validation: Archimedes spiral **89**
Method validation: ogive layup mold **91**
CHAPTER 6: CONCLUSIONS AND RECOMMENDATIONS **94**
Summary **95**
Future work **95**
LIST OF REFERENCES **97**
APPENDICES **106**
A: Coordinate points for low resolution fish shaped test part: **106**

B: sample arc fitting function code written in MATLAB 107

VITA 120

LIST OF TABLES

Table 1: Twin track overlap second track adjusted MFR test parameters for each prescribed track centerline distance. 26
Table 2: Difference between track 1 and track 2 layer heights for every twin track test and measurement method. 35
Table 3: Average striation depth for every track of every twin track test. 36
Table 4: Height compensation amounts for each test. 46
Table 5: Derivation of both cases for circular overlaps. 57
Table 6: Nominal fitting parameters. 74
Table 7: STL tessellation parameters. 75
Table 8: Fish shaped test part fit errors. 75
Table 9: Archimedes spiral test results 78
Table 10: Coordinates points for fish shaped test part. 106

LIST OF FIGURES

Figure 1:Depiction of driving parameters in AFSD. 5
Figure 2: Illustration of AFSD deposition phases and force generation. Adapted from [1]. Note that P is the axial force, F_a. 6
Figure 3: Depiction of open-loop path (left), closed-loop path (center), and a space-filling infill pattern (right). Adapted from [44]. 12
Figure 4: Flowchart of AM model to part [45]. 12
Figure 5: Depiction of sample used of overlapping deposit study if Al 6061 from Phillips et al. [33]. 15
Figure 6: (a–c) Representative etched cross-sections with tool profile schematics of the AFSD overlap [36]. 15
Figure 7: Image of ribbed aerospace panel preform (on left) before and (on right) final geometry after machining. 16
Figure 8: Polished and etched cross-section of an Al 7075 deposit which shows distinct differences between each side. 16
Figure 9: Cross section of AFSD tool during deposition 21
Figure 10: Overlapping tracks. The distance between the toolpath centerlines for tracks 1 and 2 is d and the track widths are w. The shaded region is the overlap area. 22
Figure 11: Image of twin track test builds in both primary directions. The discoloration on the test number 1 A on R is due to water being spilled on the sample after scan was completed. 25
Figure 12: Image of quad track test build in both primary directions. 27
Figure 13: Cross section of real layer height plotted with the measured LVDT displacement data for test number 1 in both directions. 28
Figure 14: Images of control print layers. 29
Figure 15: Cross section of real layer height plotted with the measured LVDT displacement data for test number 2 in both directions. 31
Figure 16: Cross section of real layer height plotted with the measured LVDT displacement data for test number 3 in both directions. 32

Figure 17: Cross section of real layer height plotted with the measured LVDT displacement data for test number 4 in both directions. 34
Figure 18: Image of completed quad track build with alternating layer path direction. ... 37
Figure 19: Collage of scan frames for layers 1, 4, 5, and 8 of all quad track builds. 38
Figure 20: XZ plane cross section of all quad track build for all layers. 39
Figure 21: Image showing completed test of linear overlap compensation method over increasing overlap. 42
Figure 22: Plot showing a cross section of print height compared to the baseplate taken from a 3D structured light scan. 43
Figure 23: Spatial plot showing actuator force in different print locations. 43
Figure 24: Images of completed layer height compensated for twin track builds next to their respective uncompensated builds. Uncompensated on the left and compensated on the right. 45
Figure 25: Plotted results of the open loop compensation of A on R test 2. 47
Figure 26: Plotted results of the open loop compensation of A on R test 3. 48
Figure 27: Plotted results of the open loop compensation of R on A test 2. 49
Figure 28: Plotted results of the open loop compensation of R on A test 3. 50
Figure 29: Spatial plot colored by process actuator force for the A on R 2 test and direction with layer difference compensation on the right. 51
Figure 30: Spatial plot colored by process actuator force for the A on R 3 test and direction with layer difference compensation on the right. 52
Figure 31: Spatial plot colored by process actuator force for the R on A 2 test and direction with layer difference compensation on the right. 53
Figure 32: Spatial plot colored by process actuator force for the R on A 3 test and direction with layer difference compensation on the right. 54
Figure 33: Example of continuous curvilinear path. 56
Figure 34: Visual description of the 2 governing cases for circular overlaps where the shaded area is the covered area. 56

Figure 35: Curvilinear overlap considering a track with a nominal width of 40 mm and a distance between tracks of 30 mm. The radius that is displayed on the X-axis is the value of the larger radius for each case (e.g., if R1 > R2 than the radius input for that line is R1). 58
Figure 36: Image of completed Archimedes spiral build with indicators for all reload location which created squeeze flash 59
Figure 37: Large Archimedes spiral completed at the Additive Manufacturing Commercialization Center under GVME as a trial build. 60
Figure 38: Large raftlike build completed at the Additive Manufacturing Commercialization Center under GVME as a trial build. Courtesy of [74]. DISTRIBUTION STATEMENT A. Approved for public release; distribution is unlimited. OPSEC#9245. 60
Figure 39: Example of 3 points forming both a triangle and a circle segment. Used and altered with permission from [46]. 67
Figure 40: Flowchart of decision logic for primitive determination. Intended adjustable parameters are bolded and underlined. 71
Figure 41: Example of fit arc segments not landing on first and last coordinates on a noncircular arc with rounded data points. 72
Figure 42: Example of multiple center point solutions for the same radii. 73
Figure 43: Fish shaped test part fit plots. 76
Figure 44: Plotted Archimedes spiral results. 79
Figure 45: Plotted result of arc fit to spline chain sprocket. 81
Figure 46: Plotted fit to an abstract b-spline curve geometry. 82
Figure 47: Challenge STL 1 plotted fit. 83
Figure 48: Challenge STL 2 plotted fit. 84
Figure 49: Challenge STL 3 plotted fit. 85
Figure 50: AFSD deposited cone. 88
Figure 51: Flowchart of automated overlap compensation algorithm for AFSD. 90

Figure 52: a) Point data describing Archimedes spiral. b). Arcs fit and oriented over toolpath point. c). Deposit from posted code. 90
Figure 53: Hybrid manufacturing process flow for the ogive layup mold. 92
Figure 54: Final ogive mold part. 93

CHAPTER 1: INTRODUCTION AND GENERAL INFORMATION

Dissertation summary

The aim of this dissertation is to provide automated path planning procedures for additive friction stir deposition (AFSD). This solid-state deformation-based metal additive manufacturing technology uses a non-consumable tool clamped in a rotating spindle. The tool has a center hole so that wrought bar stock can be forced axially through the tool as it rotates with the spindle. The tool rotation generates frictional heating between the feed material and deposition surface that softens the material enabling plastic deformation. This plastic deformation also provides adiabatic heating. During this severe plastic deformation, there is mechanical intermixing between the deposit and substrate. As the tool follows the commanded path, a layer is produced. This layer-by-layer addition produces the desired preform geometry. Although path planning methods and software exist for other additive manufacturing (AM) processes, such as fused filament fabrication for polymers and powder bed fusion for metals, no solution exists for AFSD. Currently, path planning and the subsequent computer code generation to command the machine motions for AFSD are completed manually. This approach is both time-consuming (often taking longer than the material deposition time) and prone to error. Additionally, the manual approach can limit geometric complexity, which sacrifices benefits often provided by AM. This is accomplished through three primary contributions. The most important of which is the creation of novel overlap compensation methods for both linear and curvilinear paths. To complete this automated framework a robust arc fitting method is also derived, and a complete methodology for identifying and applying compensation as a post process to slicing are also described.

Intellectual merit

This project will advance the capabilities of AFSD by leveraging knowledge and techniques currently applied for path planning of other types of material extrusion AM. Further, it will develop new strategies specifically for AFSD. These advances are necessary for rapid production of complex geometries using AFSD. Also, there is little published work available on path planning in AFSD. This work will generate new knowledge in the AFSD discipline and will serve as an important resource for those who wish to implement AFSD AM.

Path planning methods and software already exist for many types of extrusion AM but cannot be directly implemented for AFSD based on several factors unique to this process. First, due to the large track width and flash generation at the edges of the solid-state deposits, the effective deposition track width is nonconstant and adjacent tracks must have significant overlap.

This overlap requires modified material deposition rate. Second, due to the combined rotation and translation of the tool, the material flow behavior is asymmetric in the tool travel direction. Therefore, the deposition direction must be considered in the path planning.

Broader impacts

The US is currently facing national and international supply chain challenges which can cause long lead times and/or unavailability of key components, especially for large castings and forgings. These obstacles are based, in large part, on the US dependence on foreign sources to provide manufacturing capabilities. This is an issue for US national defense, security, and economic health. AFSD could address current supply chain shortfalls by enabling parts to be produced through hybrid manufacturing (i.e., preform deposition using additive manufacturing, followed by measurement and machining to achieve the final geometry and surface finish). The primary advantage of AFSD is that the feed material is readily available (e.g., plate or bar stock) and convenient to store. For complex parts to be produced with a short lead time, automated path planning methods must be established. The reduced lead times would enable parts to reach the end user in a shorter time. Automated path planning protocols also allow AM parts to be produced with improved efficiency. This provides material, time, energy, and, therefore, cost savings. The combination of AFSD and automated path planning will address gaps in the US casting and forgings infrastructure by providing a viable alternative to traditional processes.

Dissertation organization

The remainder of this document is organized as follows. The remainder of this chapter outlines introductory information about AFSD for unfamiliar audiences. Chapter 2 provides a literature review into the current state of the art of AFSD, path planning, and arc fitting. Chapter 3 provides a description of overlap compensation methods for both linear and curvilinear pathing in AFSD. Chapter 4 provides a description of the robust least squares arc fitting process for use in AM processes. Chapter 5 combines the methods learned from Chapters 3 and 4 into an automated framework for overlap feed compensation. Chapter 6 summarizes the results, presents conclusions, and discusses opportunities for future research and work. The appendix contains sample code as well as samples point arrays for arc fitting.

Background and motivation

AFSD is a solid-state AM process where bonding between layers is not caused by melting and subsequent solidification (fusion bonding). Instead, bonding occurs by physical mixing and chemical diffusion which is enabled by disturbance to the material's surface oxidation layer. AFSD accomplishes this through severe plastic deformation of both the feed material and the substrate. Other examples of solid-state AM processes are cold spray AM and ultrasonic AM, which are depicted in **Figure 1**. In cold spray AM, metallic power is accelerated using a high velocity gas stream (normally an inert gas). The impact of the particles onto the substrate causes plastic deformation and bonding. Ultrasonic AM is a sheet lamination process where a sheet or strip of material is laid down and then fused using an ultrasonic welding process. Excess material is then machined away. Solid-state processes are favored due to their low energy cost (because no melting occurs), refined grain structures due to dynamic recrystallization caused by plastic deformation, lack of hot cracking defects, and low residual stress and porosity. These combined advantages allow for superior as-built material properties when compared to fusion-based processes, such as directed energy deposition (DED) and selective laser melting (SLM). AFSD is set apart from other solid-state AM process because it can use cast or extruded bar stock instead of powders (cold spray) or foils/thin sheets (ultrasonic AM). This means that the feed material is less expensive and more widely available. AFSD is also scalable due to high deposition rates, can be used to both build and repair parts, and tends to produce more homogenous grain structures than the alternatives.

AFSD process background and introduction

As previously stated, AFSD is a solid-state deformation-based metal additive manufacturing technology that uses a non-consumable tool with a center hole for material feed through a rotating spindle. The tool rotation generates frictional heating between the feed material and deposition surface that softens the material enabling plastic deformation (depicted in **Figure 1**). This plastic deformation also provides adiabatic heating. During this severe plastic deformation, there is mechanical intermixing between the deposit and substrate. As the tool follows the commanded path, a layer is produced. This layer-by-layer addition produces the desired preform geometry.

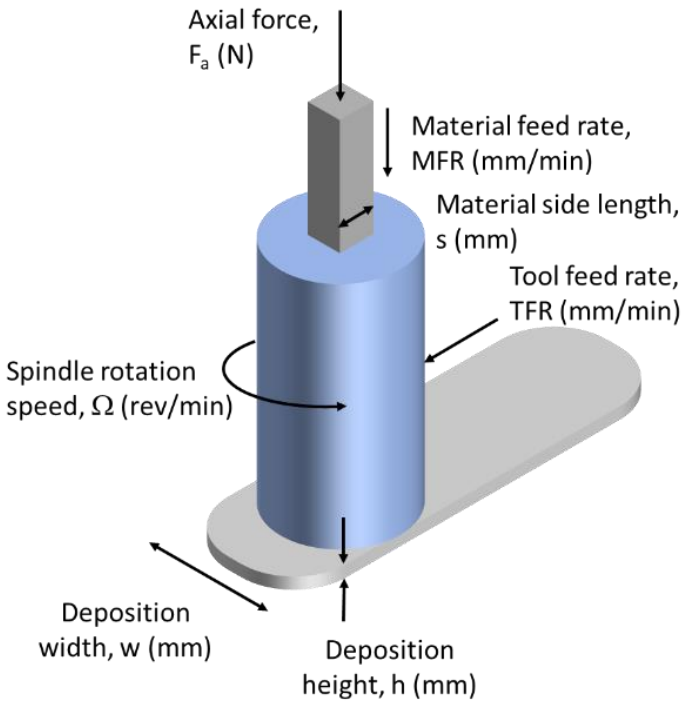


Figure 1:Depiction of driving parameters in AFSD.

A typical deposition begins with locating the flat face of the AFSD tool to the desired/appropriate distance (h) from the substrate surface which may include interaction between tool geometry and substrate as depicted in **Figure 2-I** with the tool rotating at the selected spindle speed (Ω). At this point the feed stock is forced through the rotation spindle at the material feed rate (MFR) resulting in an axial force (F_a) which causes frictional heat generation and a reduction in the feed (and substrate) material yield strength as shown in **Figure 2-II**. As the material deforms, it is forced into the space between the substrate and tool creating a larger friction area, increasing the heat generation (**Figure 2-III**). The required Fa will increase until the feed material experiences plastic failure (**Figure 2-IV**), which also provides adiabatic heating. With the feed and substrate materials being plastically deformed, in-plane motion is initiated at the tool feed rate (TFR) creating a deposition track.

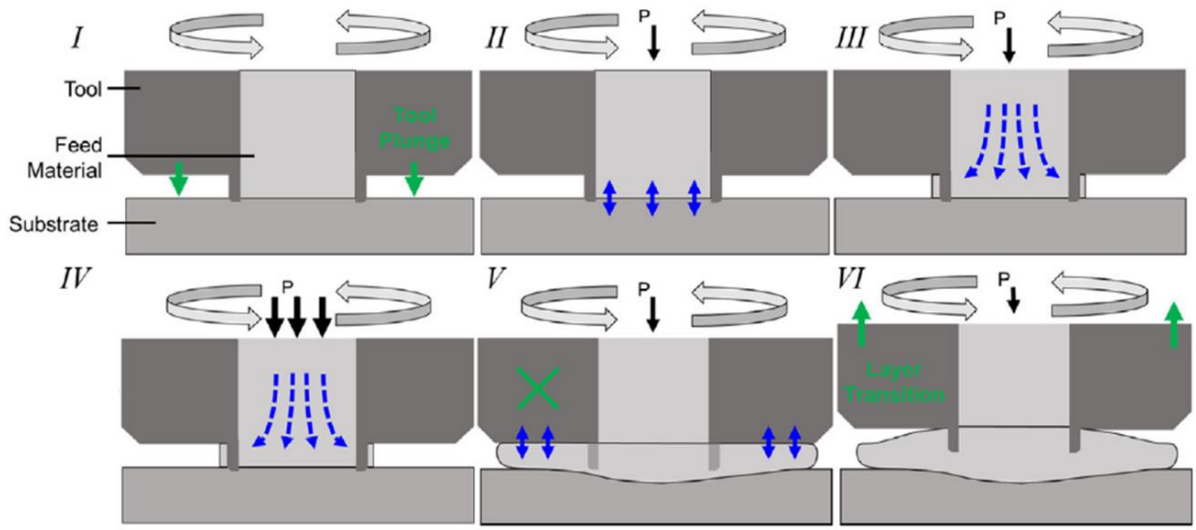


Figure 2: Illustration of AFSD deposition phases and force generation. Adapted from [1]. Note that P is the axial force, F_a.

CHAPTER 2: LITERATURE REVIEW

Introduction

This Chapter includes previous work in AFSD and path planning. The AFSD section is divided into background in friction stir welding (FSW) from which AFSD is derived, an AFSD overview, AFSD materials studies, AFSD process studies, and AFSD modeling studies. The path planning section is divided into a path planning overview, methods for approximating geometry, and optimization.

AFSD

AFSD is a solid-state AM process which shows promise for its high deposition rates (9 kg/hr for Al, and 2.5 kg/hr for Ti) [2], energy efficiency, and ability to deposit materials such as ductile metals such as aluminum alloys Al 7075 and Al 7050, magnesium alloy WE43, and titanium alloy Ti-6Al-4V, which offers flexibility relative to conventional AM approaches [3-4].

Friction stir welding background

AFSD is derived from friction stir welding (FSW) which is a solid-state welding technique that relies on bonding through severe plastic deformation [5]. Many elements of FSW, including force, torque, and tool temperature, have been modeled analytically [6-10] and numerically [10-13]. Babu et al. investigated reproducing friction stir processed material using rapid hot torsion [14]. Arora et al. computed strains and strain rates along streamlines [15]. Other work included inclusion of ceramic powders into the weld to create metal matrix composites (MMCs) [16-17]. Several authors have emphasized that knowledge from FSW can be applied to AFSD [1], [3-4].

AFSD material studies

Initial AFSD studies have focused on process to material property relationships for aluminum alloys. Gang et al. found that the ultimate tensile strength (UTS) is positively correlated with spindle speed and traverse feed rate for Al 6061 [18]. Anderson-Wedge et al. analyzed fatigue behavior in deposited Al 2219. They found local optimal parameters which produced good fatigue life using microhardness and grain size measurements [19]. Avery et al. assessed the viability of using AFSD to repair Al 7075. The study found that, while the process shows promise, the samples had reduced fatigue life to failure [20]. Ghadimi et al. found that in Al 2050 the post process material has a much larger distribution of hardness [21]. Perry et al. investigated material flow and deposit morphology using x-ray computed tomography (XCT) of a mixed material interface (Al 2024 in Al 6061) [22]. Perry et al. continued this work by adding

tracer particles to improve the resolution and draw conclusions on the fundamentals of material deformation [23]. Mason et al. investigated process to property relationships on deposited Al 7050, specifically the deposition was divided into three zones which received different amounts of heating. They found during tensile testing that the samples failed because the material was over aged [24]. Yoder et al. found that proper heat treatment of Al 7075 can return mechanical properties back to 95% of the yield strength (YS), 94% of the UTS, and 78% of the elongation for wrought material [25]. Agrawal et al. investigated the deposition of recycled Ti-6Al-4V chips using AFSD and found that the resulting tensile properties were greater than those of competing AM processes [26].

AFSD process studies

Authors have also investigated AFSD parameter selection and applications. An early study by Phillips et al. investigated the relationship between process parameters, microstructure, and mechanical properties of deposited Al 6061 and found that process parameters played little role in the microstructure and suggested that visual non-destructive inspection may be sufficient to evaluate build quality. The authors also suggested that further study be made into thermal gradients of the process and post process heat treatment [27]. Glenn et al. and Merritt et al. investigated the use of a tool with an embedded thermocouple and PID controller to control the process temperature by varying the spindle speed. These studies found that temperature control produces more consistent performance [28-29].

Schmitz et al. embedded a QR code coupon into a pocket milled into deposited material which was subsequently sealed into using AFSD. The QR code was then imaged using XCT, which has applications for part qualification/authentication [30]. Kincaid et al. successfully completed a hybrid manufacturing process to produce a ribbed aerospace panel by depositing a preform which included overlapping paths making a grid. The preform was then 3D scanned to acquire accurate dimensional data, which was used as the stock model to generate tool paths for machining the final geometry [31].

Griffiths et al. investigated how changes in parameters affected resultant microstructure in AFSD Al 6061 and copper (Cu). They found that the aluminum strain depends on the ratio of rotation speed to traverse feed rate, and that the copper strain depends only on traverse feed rate [32].

Phillips et al. investigated the tensile properties of overlapped (by 6.35 mm) parallel deposition tracks on the tensile properties of deposited Al 6061 and compared them to tensile properties of

wrought and single pass samples. They found that oxides were not well mixed in the overlapping region, but this had little impact on the tensile properties. It was observed that the single-track samples performed similarly to the overlapped tensile samples, though fractographic analysis found that oxides may have been a key element in sample failure [33]. Garcia et al. investigated heat generation mechanisms in Al 6061 and Cu with the goal of finding key relationships between processing conditions and heat generation. They found that heat generation systems are different and proposed temperature to process condition equations fit from the collected temperature data [34]. Phillips et al. evaluated the effects of lubricant on the microstructural and mechanical properties of deposited Al 5083. They observed delamination between deposited layers. This was explained as inefficient dispersion of the carbon graphite lubricant used to assist wrought material flow through the rotating spindle, which prevented bonding between layers [35]. Catalan et al. conducted a parametric study designed to analyze the impact of varying overlap on the microstructure, hardness, and tensile strength between overlapping tracks deposited with AFSD. The study found that minimum of 25% of the tool diameter must re-engage with the prior track for optimal strength [36].

AFSD modeling studies

Modeling efforts have also been completed. Stubblefield et al. modeled strain and temperature in AFSD using a mesh free smooth particle hydrodynamics model (SPH) model and compared results of the computation with physical experiments [37]. Stubblefield et al. continued their work by investigating several constitutive models including Johnson-Cook (JC), Fraser-Kiss-St-Georges (FKS), and Sellars-Tegart (ST) models which are used in FSW modeling [38]. Kincaid et al. modeled an Al 6061 deposit by creating a finite volume simulation in the open-source computational fluid dynamics (CFD) software OPENFOAM. The model was validated with experimental data [39] and for a multi-layer deposit [40]. Shi et al. have developed physics-based machine learning models for modeling temperature development in AFSD [41-42]. Wu et al. developed an analytical model incorporating tool kinematics to calculate imparted strain then stress and was validated through experimentation.

Path planning

In general, AM toolpath generation begins with a fully defined 3D computer aided design (CAD) model of the desired geometry. This model is then simplified by tessellating the object into a watertight triangulated mesh and is typically stored as Standard Tessellation Language, or

STL, filetype. Geometric details may be lost during this process, but this simplification is often necessary to provide computationally inexpensive slicing which is the process of dividing the geometry into discrete layers of a specified height. For each layer, the geometry is identified, and the paths are chosen based on whether the path must be open-loop (path start and end point is different), closed-loop (path start and end point is the same), or space-filling (typically infill, or support structure pathing). See **Figure 3**. The layers are then linked, and a script is written that contains a list of machine coordinates for the AM tool to follow at provided feed rate(s) [43], [44]. A flowchart of this general process is shown in **Figure 4**.

Methods for approximating geometry

Because information about geometry is often lost in the tessellation process, authors have investigated methods to infer the original geometry from the created points for each layer. For instance, Wade and Borish proposed a hybrid method for reconstruction of arcs and splines to reduce the complexity of output machine code while improving the surface finish of the final geometry without substantially increasing total slicing workflow time [46]. Drysdale et al. developed an algorithm which best approximates an open polygon with arcs [47]. Huang et al. suggested eliminating the tessellation step entirely and instead using binary images of cross sections from the original CAD file to preserve the curvature [48]. Outside of the path planning literature, there has also been work accomplished in fitting geometry to data point for use in metallurgy and for use with coordinate measurement machines. Forbes compiled a list of mathematical methods for fitting coordinate points to various geometries both 2D and 3D [49]. Umbach and Jones listed five methods for fitting circles to coordinate to 2D data points and compared their stability. Based on the findings of the study a method for fitting a circle in a 3D point set was also derived [50]. Comparable fitting methods have been proposed for computer-aided design and manufacturing (CAD/CAM) in computer numerical control CNC milling processes. Yeung et al. [51] presented a general framework for fitting arc splines to NC toolpath motions. Other investigations have targeted particular geometries, including precision cams [52] [53] and non-uniform scroll components [54]. Arc-fitting techniques have also been developed and employed in areas such as digital graphical interpretation [55], [56] as well as shape recognition, noise filtering, and vectorization [57]. However, because these approaches vary widely in source data, intended outputs, and overall purpose, it remains difficult to apply them directly to AM path planning especially for AFSD.

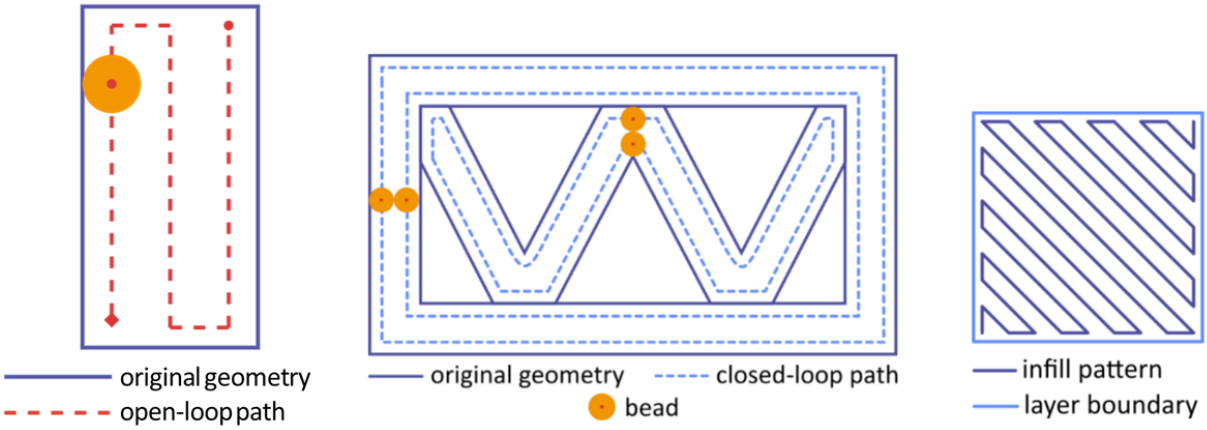


Figure 3: Depiction of open-loop path (left), closed-loop path (center), and a space-filling infill pattern (right). Adapted from [44].

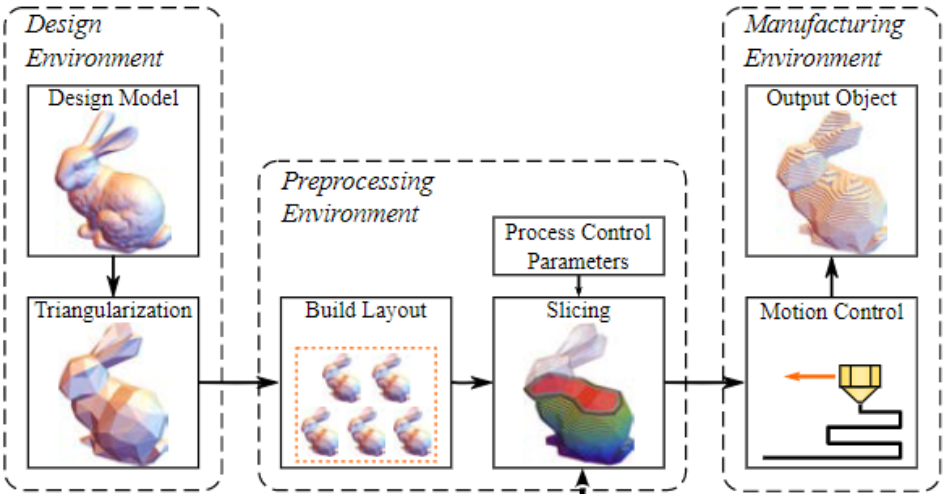


Figure 4: Flowchart of AM model to part [45].

Path planning optimization

Many recent publications have focused on saving time and/or material through optimizing tool paths to reduce unnecessary support material or reduce time where material is not being deposited. Other research focuses are on improving infill quality and geometric or surface accuracy [58]. Jin et al. proposed a method to improve build efficiency and build quality by reducing the number of sub paths required to infill a given geometry [59], including methods for increasing strength to weight ratio of a given thin-walled part using a sinusoidal wave infill pattern [60]. Jin et al. also proposed a combined method to improve infill density, prevent corner void defects, and improve surface quality of AM parts by removing sharp corners and forcing neighboring paths to be more parallel [61]. Ding et al. proposed a toolpath generation method for wire arc additive manufacturing (WAAM) which decomposes each geometric slice into polygons. This gives longer infill passes which provides increased cooling between neighboring beads and improved bead quality [62]. Ding et al. also proposed a corner path optimization algorithm which eliminates gaps in sharp corners [63]. Lastly, Steuben et al. proposed an implicit slicer which includes physics simulations in the slicing algorithm to produce infill that meets design requirements [45].

Originality

Many AFSD investigations focus on process to property relationships, modeling the process physics, or determining characteristics of deposited material. Some knowledge gaps that motivate this dissertation are:

- Research into part scale defects, such as squeeze flash, or bonding defects (must be prevented for successful prints).
- Interactions between overlapping or intersecting paths (essential for large scale parts).
- Best practices for selecting layer geometry, such as maximum overhang, and predicting deposition geometry.
- Path planning procedures specifically for AFSD.

For many of these topics, no prior work is available in open literature. Two published studies include overlapping tracks: [33] and [36]. Both studies focus on metallurgy and mechanical properties. In the study by Phillips et al. [33] that considers material properties between overlapping tracks, the MFR on the return pass was decreased to reduce flash. The MFR was calculated using an amount of “overbuild”, or material that escaped the width of the tool, and

halving that amount of overbuild. It was found that the selected operating parameters produced 11% overbuild, so the parameters used on the return pass were reduced to create a 5.5% overbuild. Using this methodology, no squeeze flash was observed. See **Figure 5**.
Cahalan et al. [36] conducted a parametric study to analyze the impact of overlap variation on the microstructure, hardness, and tensile strength between the deposited tracks. Nine samples were deposited varying in overlap from -6.4 mm (-0.25 in) to 19.1 mm (0.75 in) in increments of 3.2 mm (0.125 in) (see **Figure 6**, where the positive and negative overlaps are depicted). The MFR and TFR remained constant for each build and squeeze flash was generated. A study conducted by Kincaid et al. produced an aerospace panel by hybrid manufacturing, which included AFSD, structured light scanning, and computer numerical control (CNC) machining [31]. See **Figure 7**.

Prior research into AFSD path planning is not available. Many slicer/path planning approaches exist for extrusion AM but cannot be directly used for AFSD. One of the major reasons is the constant bead width approximation [44] conventionally applied in AM, where a single bead width (typically is the size of the nozzle) is used for an entire print. If bead width is constant, then the ratio of travel speed to material feed is also constant throughout the entire print. Due to the necessary overlaps in AFSD, this ratio is not constant. This is both a constraint and a benefit as it allows for production of fully dense parts.

Another primary difference from AFSD is the inherent inhomogeneity of the process. Because the tool is rotating while traversing, the surface speed vector on one side of the tool matches the travel direction; this is referred to as the advancing side (AS). On the other side of the tool, the surface speed vector opposes the feed motion; this is referred to as the retreating side (RS). The material temperature is higher on the AS than the RS and, therefore, the material is softer which increases the flow. This effect can be observed in deposit microstructure [21-23] and shown in **Figure 8**. Because of this, the order and direction of deposition tracks must be considered during path planning. This research leverages pre-existing path planning methods and adapts them to address AFSD challenges. The goal is to create a working algorithm and develop machine code which will perform deposition to provide parts without defects. Existing methods which rebuild original geometry (such as arcs) from point data will be leveraged [43-50].

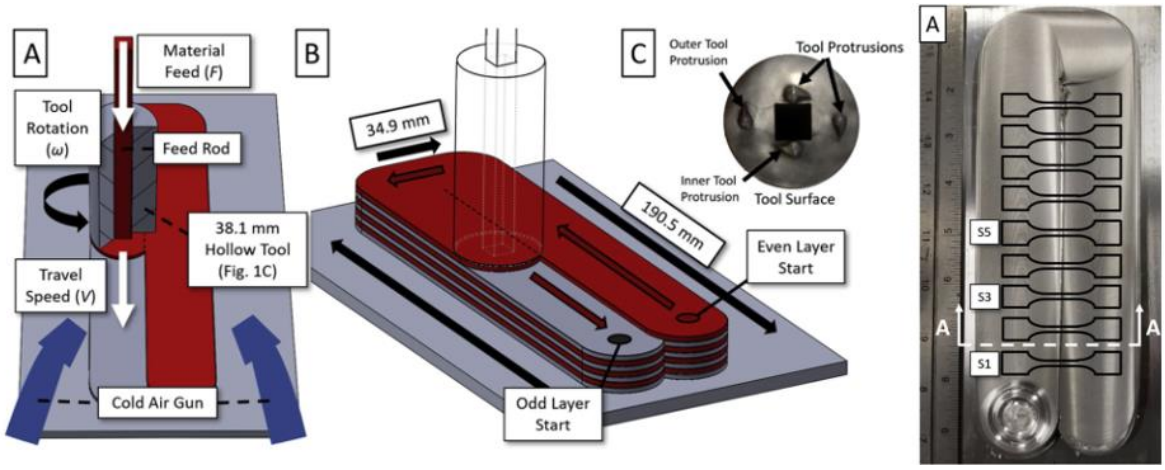


Figure 5: Depiction of sample used of overlapping deposit study if Al 6061 from Phillips et al. [33].

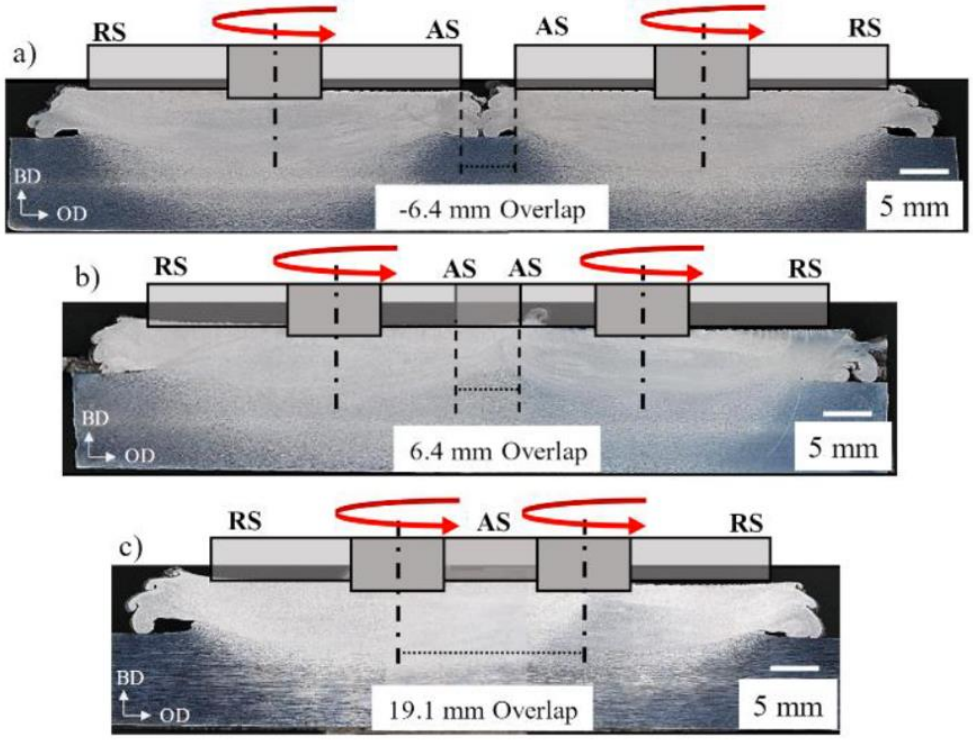


Figure 6: (a–c) Representative etched cross-sections with tool profile schematics of the AFSD overlap [36].

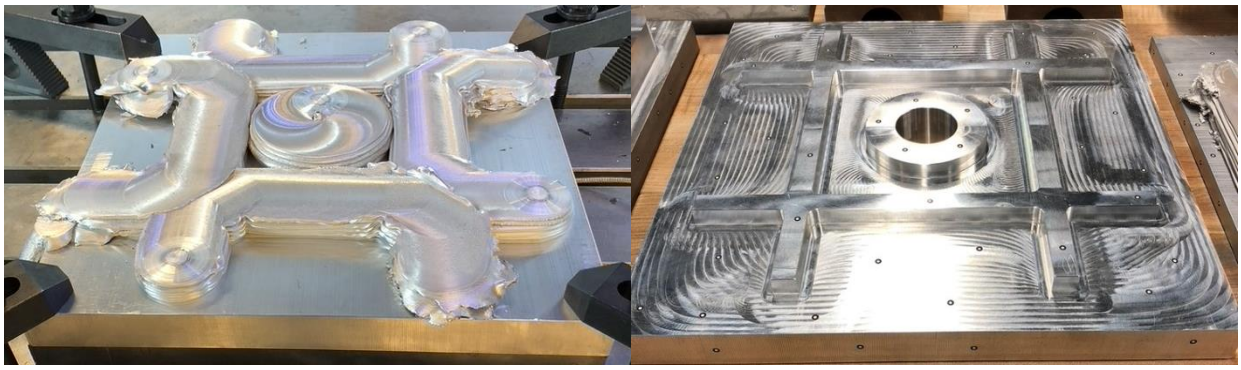


Figure 7: Image of ribbed aerospace panel preform (on left) before and (on right) final geometry after machining.

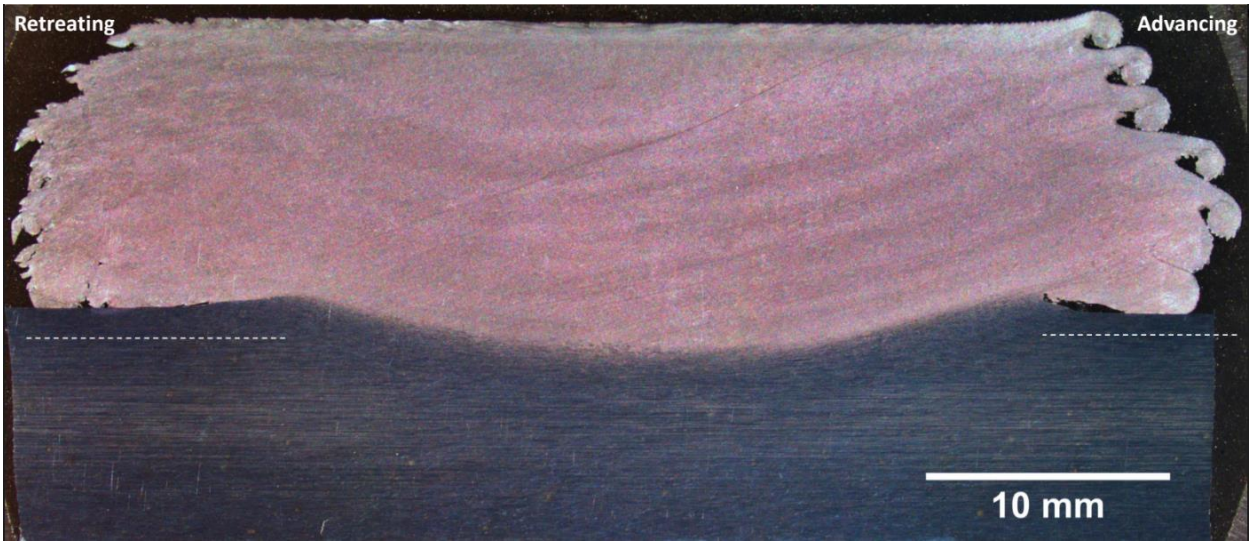


Figure 8: Polished and etched cross-section of an Al 7075 deposit which shows distinct differences between each side.

CHAPTER 3: OVERLAPPING TRACK FEED RATE COMPENSATION METHODS FOR AFSD

Manuscript introduction

This Chapter is divided into 3 sections the first of which includes a manuscript describing a volume based linear overlap compensation method for AFSD. The second and third sections expand upon this manuscript by incorporating layer height compensation in the second and compensation for curvilinear overlaps in the third. The manuscript which is currently in draft form represents a primary contribution of this dissertation and addresses a major initial knowledge gap in the path planning for the production of component preforms using AFSD.

Manuscript attributions:

Joshua Kincaid: wrote the original draft, derived the method, and was responsible for data collection and interpretation.

Jeffrey Burdick: provided helpful technical feedback and additional testing which could not be included in this document.

Tony Schmitz: edited the manuscript and provided technical advising.

Feed rate selection in additive friction stir deposition: compensation for overlapping tracks

Joshua Kincaid[1], Jeffrey Burdick[3], Tony Schmitz[1,2]

[1]The University of Tennessee, Knoxville

[2]Oak Ridge National Laboratory

[3]US Army Ground Vehicle Systems Materials Engineering Directorate

Abstract:

Additive friction stir deposition (AFSD) is an emerging solid-state metal additive manufacturing (AM) technology, which is favored for producing near net shape, fully dense parts at a relatively high deposition rate. In AFSD when parallel tracks are deposited the tool should be allowed to overlap the previous track, reprocessing that material into the current track, ensuring that the deposit remains fully dense and that the neighboring tracks are fully bonded. However, process feed rates must be adjusted to prevent both an overfed condition which produces excess squeeze flash and increases process reactive forces while avoiding an underfed condition which can produce galling, voids and/or a decrease in effective layer height. These defects when introduced often cause build failure. This paper proposes a method for determining appropriate process feed rates, either material feed rate or tool traverse feed rate, by calculating the appropriate volume of material from a track. This method is then demonstrated to reduce defect formation, mitigate squeeze flash creation, and prevent print failure.

Introduction

Additive friction stir deposition (AFSD) is a solid-state metal additive manufacturing (AM) process based off of friction stir welding [5], [9], [14], [15], [64], [65] and relies on severe plastic deformation to disturb metallic oxidation layers and force mixing between the substrate (build plate or prior layer) and the feed materials into the deposit [1-3]. This deformation is driven by a non-consumable rotating tool that has one or more holes for material extrusion. Tool rotation during extrusion generates frictional heat lowering the yield strength allowing for lower force plastic deformation. Due to the tool rotation travel AFSD experiences direction dependance following the small change in relative strain rates; the side where the vector of rotation and vector of travel align is called the advancing side (AS); and the side where the vector of rotation and vector of travel are opposed is called the retreating side (RS). The AS experiences relatively higher mass transport and temperature and, therefore, offsets the deposition track towards the AS [1-3].

Much initial research in AFSD has been focused on process to property relationships many studies focusing on deposition of Al 6061 [18], [27], [33], [66], [67], [68]. Many other studies are focused on high strength Al alloys 2xxx and 7xxx alloys [19], [21], [24], [36]; with a few focusing on heat treatment of Al 7075 by Yoder et al. [25], [69] and Ding et al. [70]. Garcia et al. [34] and Griffiths et al. [32] deposited and compared results between Al 6061 and Cu deposits. Perry et al. [22] investigated material flow in AFSD by x-ray computed tomography (XCT) scanning a mixed alloy deposit of Al 2024 and Al 6061. Perry et al. [23] extended this research by adding tracing particles to improve the resolution. Other studies have made progress on process modeling of AFSD. Stubblefield et al. [37] investigated the use of a smooth particle hydrodynamics model and comparing that to results of a physical experiment. Additionally, the authors expanded onto their efforts by comparing several constitutive models [38]. Kincaid, K et al. modeled a single layer Al 6061 deposit using a finite volume approach in the open-source computation fluid dynamics software OPENFOAM, validating the model with experimental data [39]; this process was repeated for a multilayer deposit [40]. Shi et al. [42] created a machine learning algorithm to elucidate some of the underlying physics of temperature evolution in AFSD and found good agreement between the model and preformed measurements. Shi et al. continued this worked by developing a new model which is physics informed [41].

Other studies investigate use cases for AFSD. Avery et al. [20] assessed the viability of AFSD repair in Al 7075. Hartley et al. [71] evaluated AFSD for cladding of thin automotive parts. Schmitz et al. investigated the embedding of a QR coded coupon sealed into a part using AFSD; the QR was then read using XCT, which has application in part qualification.

Currently, very little research has focused on process planning methods with only a few papers including studies on overlapping paths. Phillips et al. [33] created an overlapping deposit in Al-6061 T6 and evaluated the resulting material properties the MFR was adjusted in this study by evaluation of overbuild for a single track. Kincaid, J et al. [31] produced an aerospace panel via hybrid manufacturing using AFSD, structured light scanning and milling; this study adjusted MFR in the overlapping tracks. Finally, Cahalan et al. [36] conducted a study to compare the microstructure, hardness, and tensile property differences over a range of overlaps from $-6.4\ mm$ ($-0.25\ in$) to $19.1\ mm$ ($0.75\ in$) in increments of $3.2\ mm$ ($0.125\ in$) each deposit was completed such that the advancing side of each track was included in the overlap.

In the context of path planning in AM at this time no studies can be located for AFSD. However, in wire arc directed energy deposition (DED-Arc) (also called wire arc additive manufacturing (WAAM)) a few studies can be found where path and bead width are adjusted to improve layer surface quality. Xiong et al. [72] proposed a framework to create adaptive toolpaths for DED-arc using a level-set method to allow contours to be nonconstant bead width; using this method the authors successfully printed several thin wall samples. Hu et al. [73] created a model to predict optimal bead spacing in DED-arc based on a number of variables with the goal of improving layer surface finishes, the model was compared to a multi-bead deposit. Jin et al. [61] proposed an implicit algorithm to remove sharp corners from deposition to avoid issues with voids and local overbuild.

This paper outlines a method for approximating resultant track geometry and necessary feed parameter changes in response to overlaps in AFSD for linear paths. This method makes assumptions based on the volume fraction of material included in each subsequent track. Due to the large process forces in AFSD the real-world machine changes position in response to different processing parameters and thus is also discussed. The goal of this method to reduce defect formation and prevent print failure. Method validation will include multiple twin track builds featuring multiple overlap conditions and directions, and to simulate a larger build 3 quad track builds are also completed.

Methods

Approximating deposit geometry

First, a method for predicting the deposited track geometry is derived. The volumetric flow rate of the feed material is $\dot{V}_{extrude} = MFR \cdot A_c$, where MFR is the material feed rate in units of distance per time and A_c is the cross-sectional area of the feed material. Assuming constant density and mass, the volume of deposited material $V_{deposit}$ must be equal to the extruded volume. Approximating the bead geometry as a rectangle with height h and width w gives $\dot{V}_{deposit} = h \cdot w \cdot TFR$, where TFR is the tool traverse feed rate (**Figure 9**). The two flow rates are set equal in Equation 1:

$$w \cdot h \cdot TFR = A_c \cdot MFR \tag{1}$$

The deposit height h is fixed due to standard slicing and path planning procedures and is ideally fixed throughout a print. The deposit width is calculated using Equation 2:

$$w = \frac{MFR}{TFR}\frac{A_c}{h} \tag{2}$$

Assuming constant h and Ac, it follows that the deposit width will become a function of the ratio between TFR and MFR.

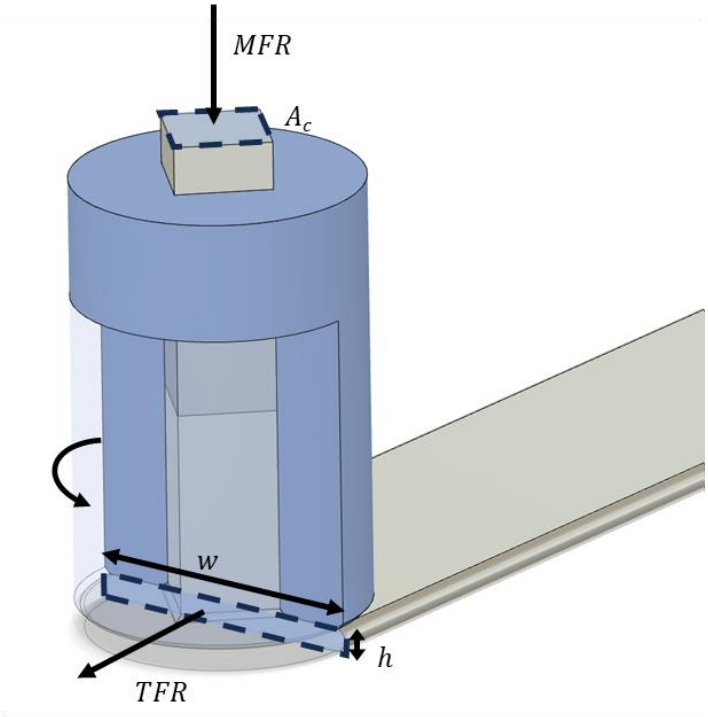


Figure 9: Cross section of AFSD tool during deposition

Overlap feed compensation

Utilizing the predicted track width, a method for compensating feed rates for an overlap condition is now derived. The goal of this method is to prevent both the creation of squeeze flash from overfed conditions (i.e., excess volume of material in the system) and the creation of voids from underfed conditions (i.e., too little volume under tool face). A volumetric analysis approach will be used that will calculate the width of a track that is already occupied with material from a prior track. For this method, it is assumed that differences in material deposited on the AS and RS (will thoroughly describe these in introduction) are either repeated (i.e., all paths are in the same direction as the prior track) or negligible.

Suppose that two parallel linear tracks are deposited where track 1 is produced using process parameters which create a track of width w_1 where d is the distance between toolpath centerlines and is bounded by $0 \leq d \leq w_1$. It follows that the volume of material in track 2, and subsequently the track 2 width (w_2), must decrease as d decreases to avoid an overfed condition. The geometry is shown in **Figure 10**.

To ensure the proper amount of material is deposited, w_2 must be calculated. This value informs the selection of MFR, TFR, or some combination. This is shown by Equation 3.

$$w_2 = w_1 \frac{w_1 - \left(\frac{w_1}{2} + \frac{w_1}{2} - d\right)}{w_1} = w_1 \frac{d}{w_1} \tag{3}$$

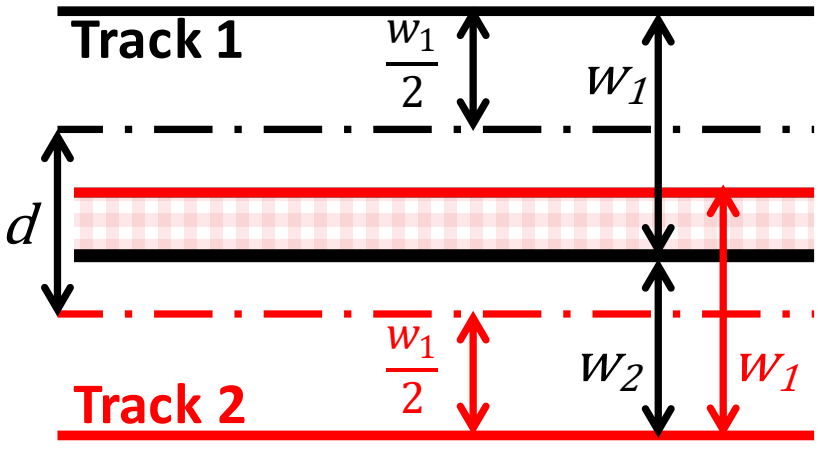


Figure 10: Overlapping tracks. The distance between the toolpath centerlines for tracks 1 and 2 is d and the track widths are w. The shaded region is the overlap area.

Substituting in from (2) and canceling the h and A_c terms, which are assumed constant, gives Equation 4.

$$\frac{MFR_2}{TFR_2} = \frac{MFR_1}{TFR_1}\frac{d}{w_1} \tag{4}$$

This method can be repeated for any number of parallel linear tracks. To generalize, the 1 subscript is dropped from the track width variable as shown in Equation 5.

$$\frac{MFR_2}{TFR_2} = \frac{MFR_1}{TFR_1}\frac{d}{w} \tag{5}$$

This relationship can be further simplified into limiting cases by holding either TFR or MFR constant as shown in Equations 6 and 7.

$$MFR_2 = MFR_1\frac{d}{w} \quad (6); \qquad TFR_2 = TFR_1\frac{w}{d} \quad (7)$$

Maintaining MFR means maintaining the material deposition rate while increasing the rate that the tool face interacts with material since the machine must now process the same amount of feed material with now the additional material from the prior track. In contrast, maintaining TFR means a reduction in material deposition rate while maintaining the rate the tool face interacts with material.

Summary

First, a method for predicting the deposited track geometry based on volumetric flow is derived. That method is used to define feed rate compensation for linear overlapping toolpaths. The two primary equations which will be used in the following experimental section are repeated for convenience.

$$w = \frac{MFR}{TFR}\frac{A_c}{h} \tag{2}$$

$$MFR_2 = MFR_1\frac{d}{w} \tag{6}$$

Experimentation

Experiments were conducted to validate this method. In the first series of tests a range of overlap amounts evaluated using the method prescribed overlap compensation in the overlapping track for two print directions for twin tracks. During these tests the cantilever-based deflection of the z-axis spindle assembly deflection was monitored using a commercially available HGSI ILPS-19S linear variable inductive transformer (LVIT) mounted in the XZ plane with the tool center.

The second series of tests use a single overlap amount for four tracks and more layers to simulate method effectiveness for larger parts. For all testing the substrate and feed material are commercially available Al6061-T6. The feed material was coated in a graphite lubricant to reduce friction between the interior of the tool and the feed material. All initial AFSD deposits are accomplished with a MELD Manufacturing L3 discrete feed system which requires an actuator to extrude that material. When one unit of feed material (12.7mm (0.5") square bar by 508mm (20.") length) is fully consumed the deposition tool must leave the build so that additional material may be loaded. For all experiments each layer was 3D scanned with a GOM (now Zeiss) ATOS Q. All tests were carried out at a PID controlled tool face temperature of $T_{tool} = 410\ °C$. The tool was a H13 steel with four teardrop shaped nubs protruding from the surface to a depth of 2.3 mm (0.090 in). The nominal process parameters were $TFR = 254\ mm/min$ $(10\ ipm)$, $MFR = 152.5\ mm/min$ $(6\ ipm)$, and $h = 2\ mm$ $(0.080\ in)$ producing a nominal track width of $w = 47.625\ mm$ $(1.875\ in)$. MFR was the parameter adjusted in the overlaps.

Twin tracks overlap range tests

A total of 9 twin track builds were completed over 4 overlap distances and compensation amounts as shown in **Table 1**. Each overlap was completed for two print orientations. The first orientation is where the advancing side of the second track is intermixed with the retreating side of the first track (A on R) and the second orientation is the inverse of this (R on A). The setup for this is shown in **Figure 11** where the second track for each setup is offset such that the start-up point is not already overlapping so that flash generation does not occur prematurely due to process start interactions. For each build, 4 total layers were completed. All travel was in the $-Y$ coordinate direction. During all depositions displacement data was collected via the LVIT sensor at a rate of 300Hz. After each layer was completed, a 3D scan was collected and aligned using reference coordinate dots. In this testing an additional build was completed with no feed rate compensation as a control. The control was completed using the same nominal feed rates for each track at a distance of $d = 25.4\ mm$ $(1.\ in)$ between path centerlines in the A on R direction as this direction is the most favorable in preventing machine damage as discussed later.

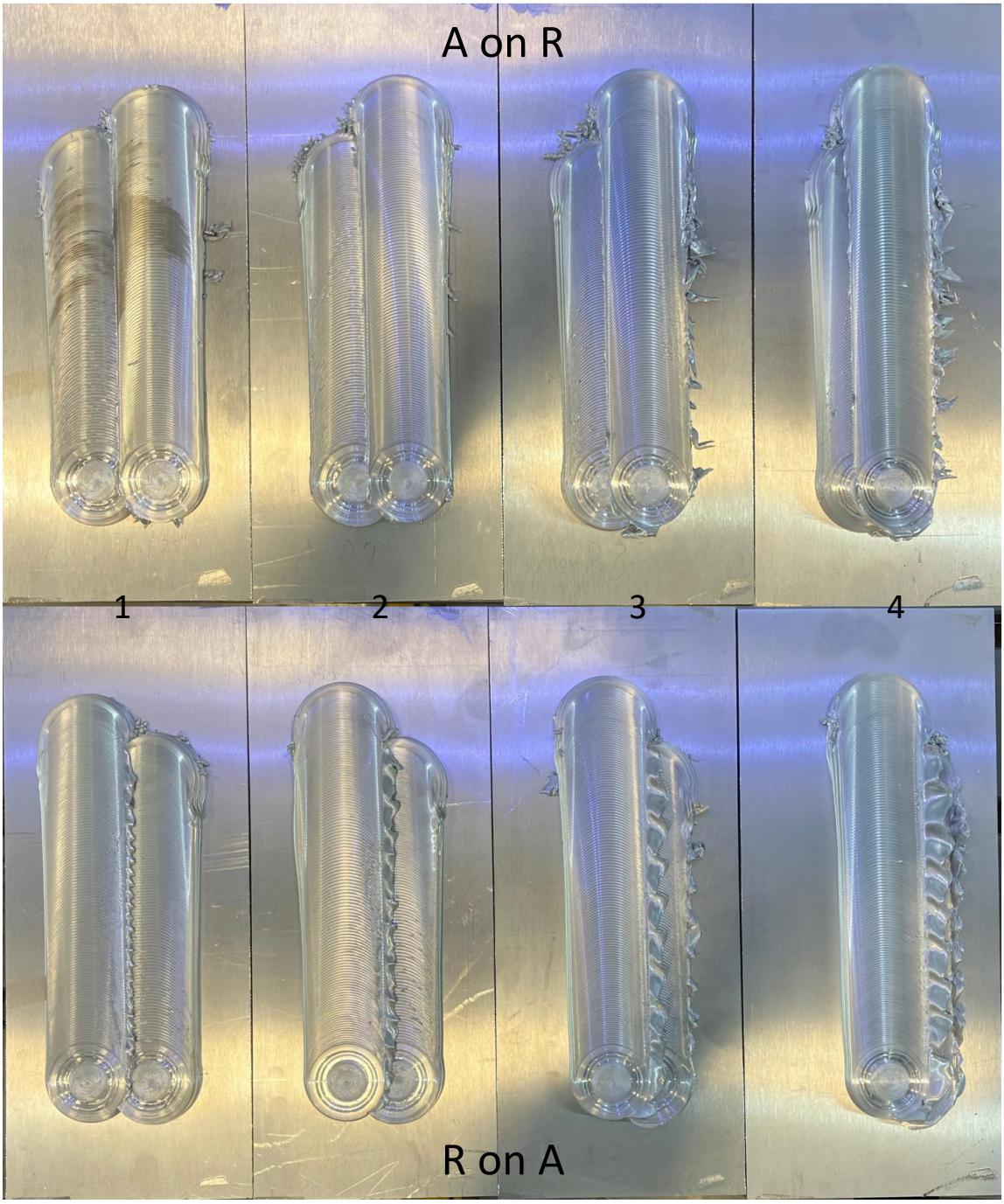


Figure 11: Image of twin track test builds in both primary directions. The discoloration on the test number 1 A on R is due to water being spilled on the sample after scan was completed.

Table 1: Twin track overlap second track adjusted MFR test parameters for each prescribed track centerline distance.

Test number:	**1**	**2**	**3**	**4**
Distance *mm* (*in*)	31.75 (1.25)	25.40 (1.00)	19.05 (0.75)	12.70 (0.50)
MFR2 *mm/min* (*ipm*)	101.60 (4.0)	81.280 (3.2)	60.960 (2.4)	40.640 (1.6)

Quad track build

Three quad track builds were completed. For the first build on each layer the advancing side of the new track is intermixed with the retreating side of the prior track (A on R). The second build is the inverse of this where the retreating side of the new track is intermixed with the advancing side of the prior track (R on A). The third alternates build direction starting with the advancing onto retreating side setup. For each build, 8 layers were completed and between each layer a 3D scan was taken. The overlap selected was a track centerline distance of $d = 25.4\ mm$ $(1.00\ in)$ or test setup 2 when referencing Table 1.The track start and ends are outside of the overlapping are to avoid interfering with the overlap compensation results this is shown in **Figure 12**.

Results

Each build was successfully completed without failure though some squeeze flash was created in the extreme overlap cases in this section the overall quality of the overlap builds is discussed along with results shown in cross sections of the 3D scans for both the twin track and quad track builds. Conclusions about the effects of deflection, eccentric tool motion, and directional effects on the generation of squeeze flash are also discussed. For all cases a moving mean filter of width of 300 is applied to the LVDT data such to filter out the impact of the X coordinate direction motion caused by the process and tool motion which was impacting data readability. Images of the completed builds referenced in the prior section.

Twin track builds

This section is divided initially into groups by overlap amount for the presentation of the large amount of point data collected. Then discussion of the overall results for these tests are presented and compared showing a large difference between samples by travel direction with flash be pushed towards the retreating side for all cases.



Figure 12: Image of quad track test build in both primary directions.

Control test: $d = 25.40\ mm$

The control test failed during layer 3 when a small piece of squeeze punctured the cooling water jacket seal on the rotation tool purging chilled onto the build. On layer 2 the system was oscillating near the system maximum actuator force capacity where reaching a limit (~25000 N) causes the machine to halt tool motion and slow to $MFR = 12.7\ mm/min$ (0.5 ipm), often this condition is irrecoverable and prints often fail without operator inference to decrease volume flow into the build. An image of each layer of the control build is shown in **Figure 13**.

Test number 1: $d = 31.75\ mm$

For both the A on R and R on A cases, this test produced very little squeeze flash with the R on A sample producing a small amount of repeating squeeze flash pushing from the 2nd track onto the 1st. As the volume of this squeeze flash is small and is repeating, it is unlikely to impact and build. However, this slight change in MFR did result in a slight decrease in h which in the R on A case which exacerbated the squeeze flash generation. This theme is repeated between all tests. Cross sections of the 3D scans are combined with the LVDT data and shown in **Figure 14** for both directions.

In the plots, both the LVDT data and the 3D scan cross sections are shown. For all cases, the track 1 height is higher than the track 2 height and the scan data always shows a greater

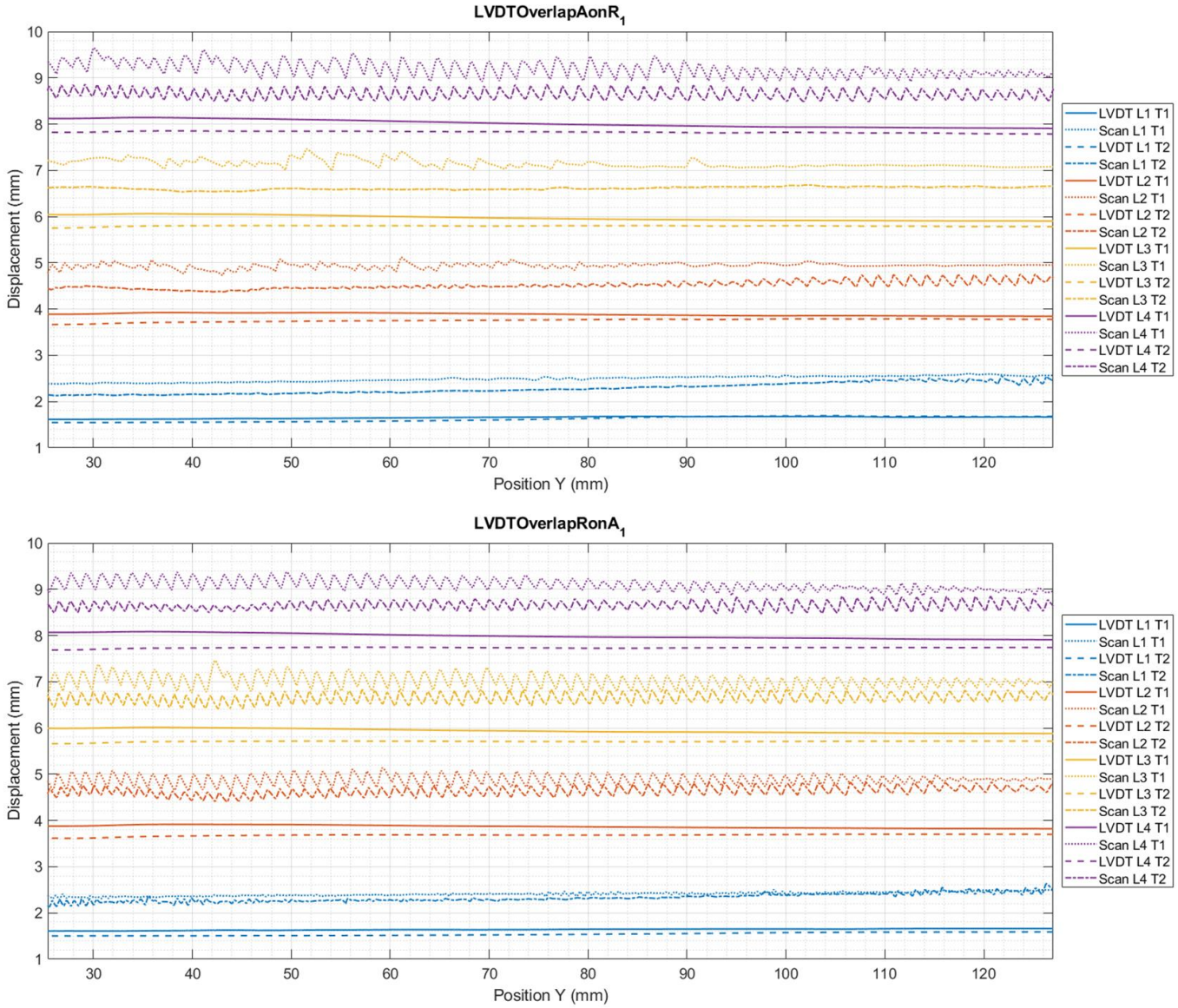


Figure 13: Cross section of real layer height plotted with the measured LVDT displacement data for test number 1 in both directions.

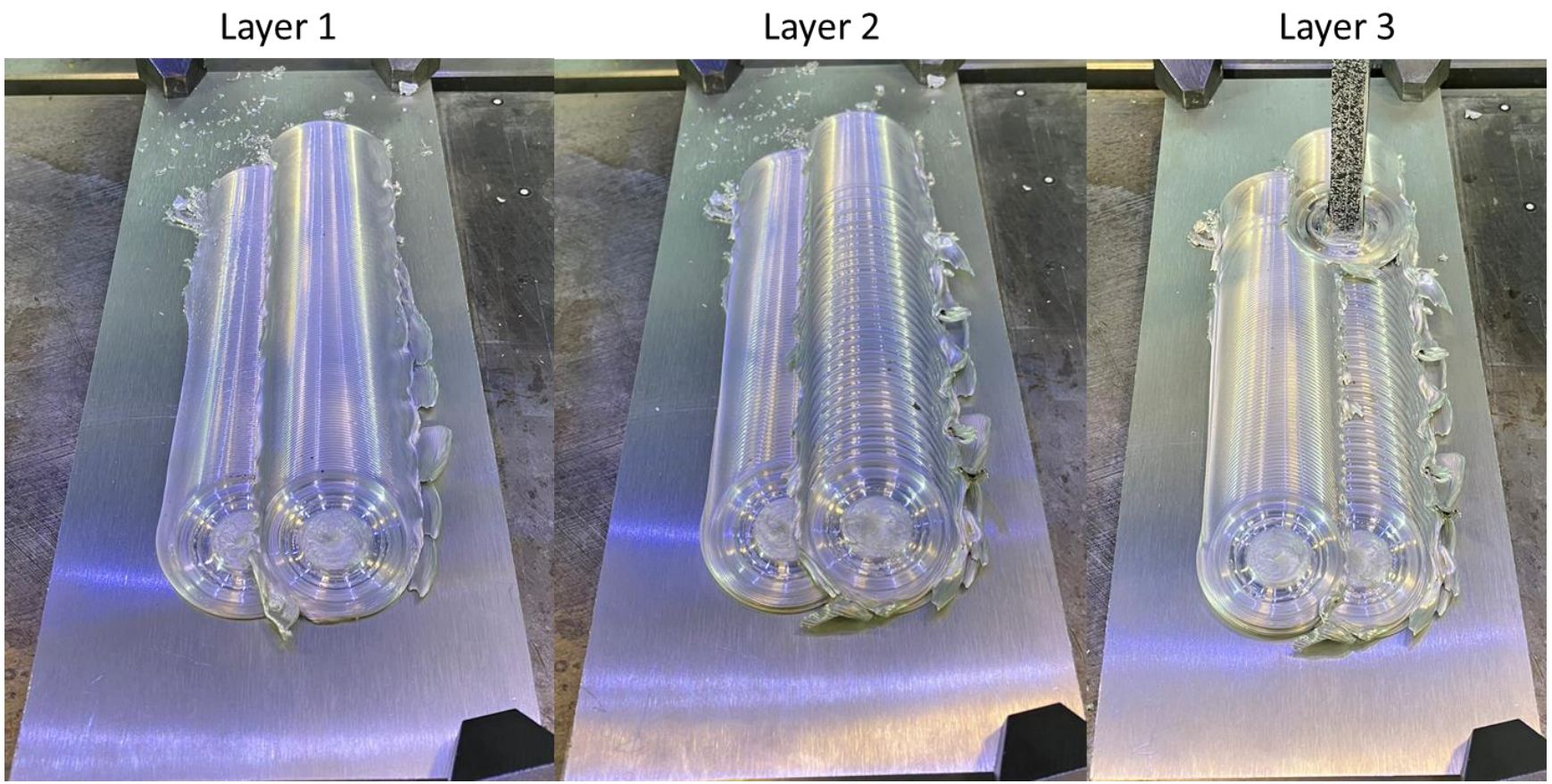


Figure 14: Images of control print layers.

displacement than the LVDT which indicated that the cantilever motion that the LVDT sensor is measuring is not encapsulating all modes of deflection though the characteristic deflection is captured which is discussed later. Another notable feature is the striation pattern which is recorded in the 3D scan data as the apparent ridge pattern in the displacement. There appears to be very little striation depth or clarity on the 1st layer of any sample and in the case of the A on R test number 1 there is very little repeatable pattern except on layer 4.

Test number 2: $d = 25.40\ mm$

For both the A on R and R on A cases, this test produced very little squeeze flash (though more than test 1) with the R on A sample producing a small amount of repeating squeeze flash pushing from the 2nd track onto the 1st. As the volume of this squeeze flash is small and is repeating, it is unlikely to impact and build. However, this change in MFR did result in a decrease in h in the R on A case which exacerbated the squeeze flash generation. This theme is repeated between all tests. Cross sections of the 3D scans are combined with the LVDT data and shown in **Figure 15** for both directions.

In the plots, both the LVDT data and the 3D scan cross sections are shown. For all cases, the track 1 height is higher than the track 2 height and the scan data always shows a greater displacement than the LVDT. In these tests the striation pattern is more consistent between the tests and all layers above 1.

Test number 3: $d = 19.05\ mm$

In this test, a small amount of squeeze flash was generated for the A on R case and pushed to the R side of the 2nd track outside of the build. For the R on A case, a larger amount of flash was generated, while still repeating some further parameter adjustment may be required as the impact of the change in h appears to increase as the distance between the tracks decreases. Cross sections of the 3D scans are combined with the LVDT data and shown in **Figure 16** for both directions.

In the plots both the LVDT data and the 3D scan cross sections are shown. For all cases the track 1 height is higher than the track 2 height and the scan data always shows a greater displacement than the LVDT. In these tests the striation pattern disappears slightly on the R on A case, especially on track 1. This effect may be due to tool engagement with the prior track being near 50% and thus canceling out some tool motion.

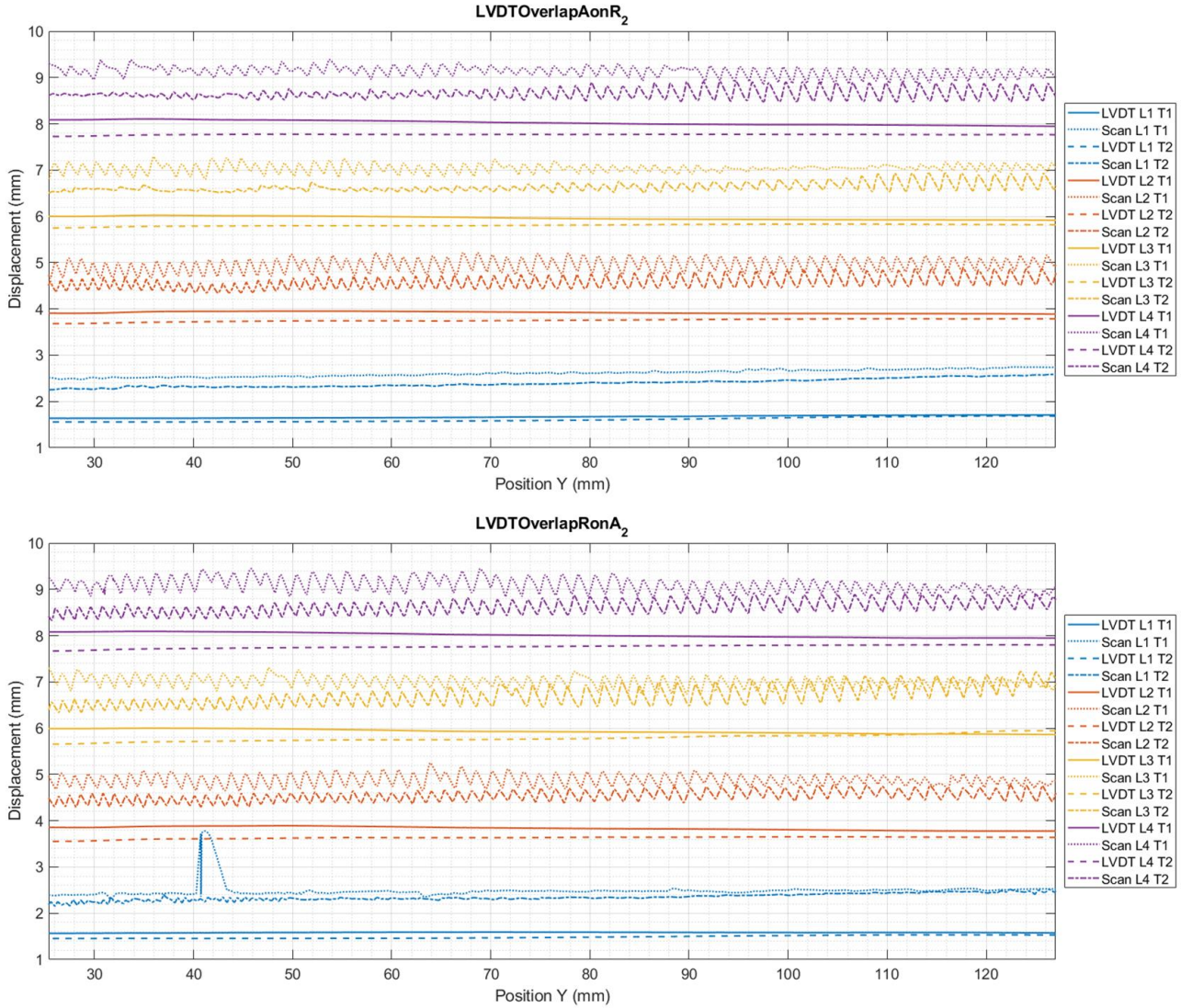


Figure 15: Cross section of real layer height plotted with the measured LVDT displacement data for test number 2 in both directions.

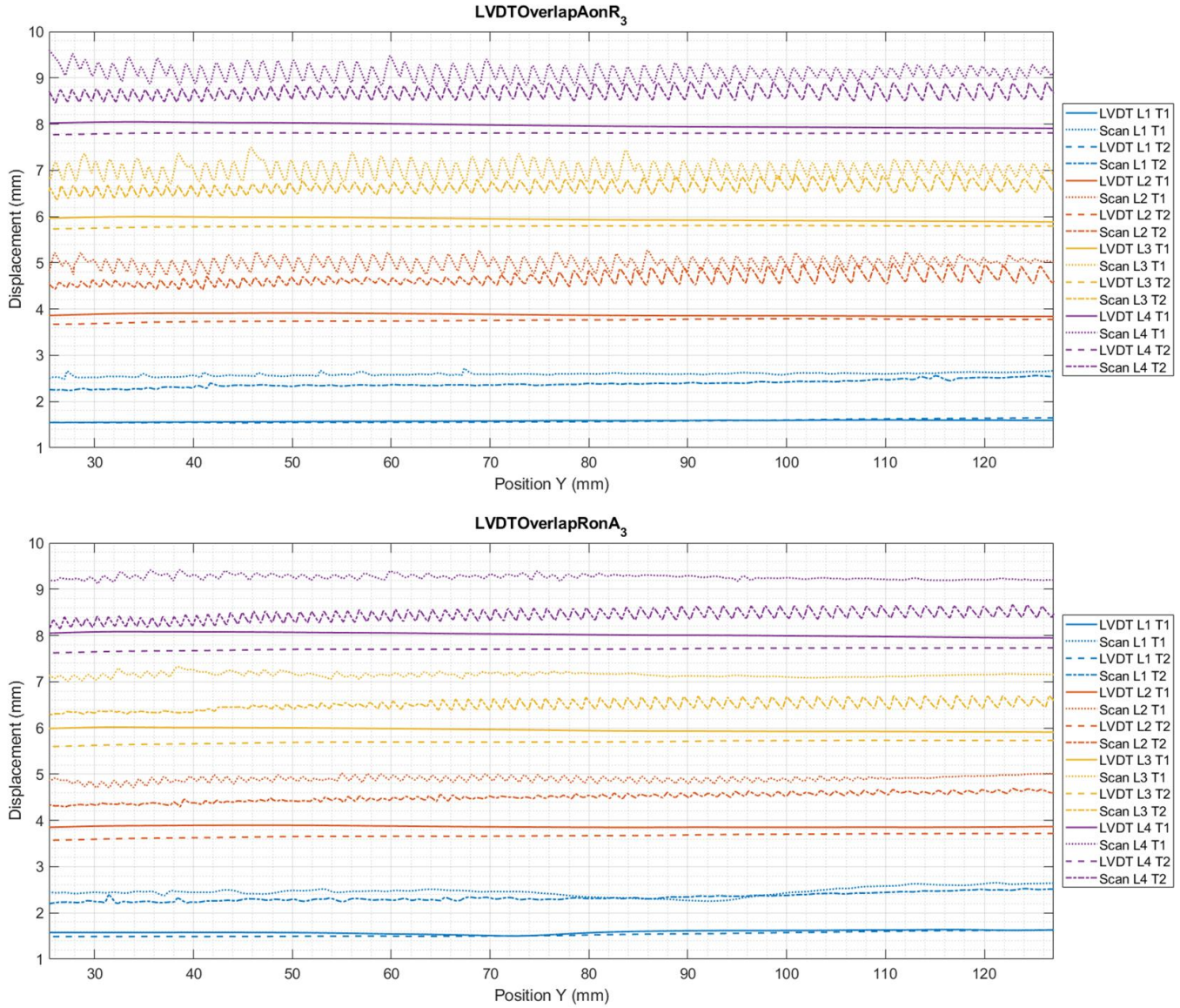


Figure 16: Cross section of real layer height plotted with the measured LVDT displacement data for test number 3 in both directions.

Test number 4: $d = 12.70\ mm$

In this test, a small amount of squeeze flash was generated for the A on R case and pushed to the R side of the 2nd track outside of the build. For the R on A case, a larger amount of flash was generated. The generated flash increased slightly on subsequent layers, meaning further parameter adjustment may also be required for overlaps as severe as this in the R on A case. Cross sections of the 3D scans are combined with the LVDT data and shown in **Figure 17** for both directions.

In the plots, both the LVDT data and the 3D scan cross sections are shown. For all cases, the track 1 height is higher than the track 2 height and the scan data always shows a greater displacement than the LVDT. The track 1 scan data for the R on A case does appear in the figure as after layer 1 the entirety of track 1 was obscured by flash.

General discussion

For all tests, the described method successfully reduced the amount of squeeze flash generated and was especially successful at reasonable overlaps and in the A on R direction. The method may find greater success if the layer height was controlled through either closed or open loop. General trends between all tests are as follows:

- Any squeeze flash generated was always formed on the advancing side and pushed into the retreating where in the R on A case as onto the prior track, and in the A on R case was outside of the build which reduced any impact on build success.
- Motion in the tool a appears to be responsible for the scale of the striation which is consistent with literature for FSW [64], [65]. The striation pattern on the surface may indicate microstructural changes in the deposit though that is outside the scope of this study.
- Changes in process parameters change the required total z direction force which changes the layer height by changing system deflections which can also worsen squeeze flash generation.

Results for average layer height difference for every twin track test and measurement method are shown in **Table 2**, and striation depth is shown in **Table 3**. In general, the layer height difference between tracks 1 and 2 increases for each layer deposited and increases as the distance between tracks decreases. The clearest data for these trends is the LVDT data though for the over tests where more than half the tool was engaged in the overlap the change decreased per layer. The valley data is shown as it is likely that the striations do not well support tool load and do not contribute to effective layer height.

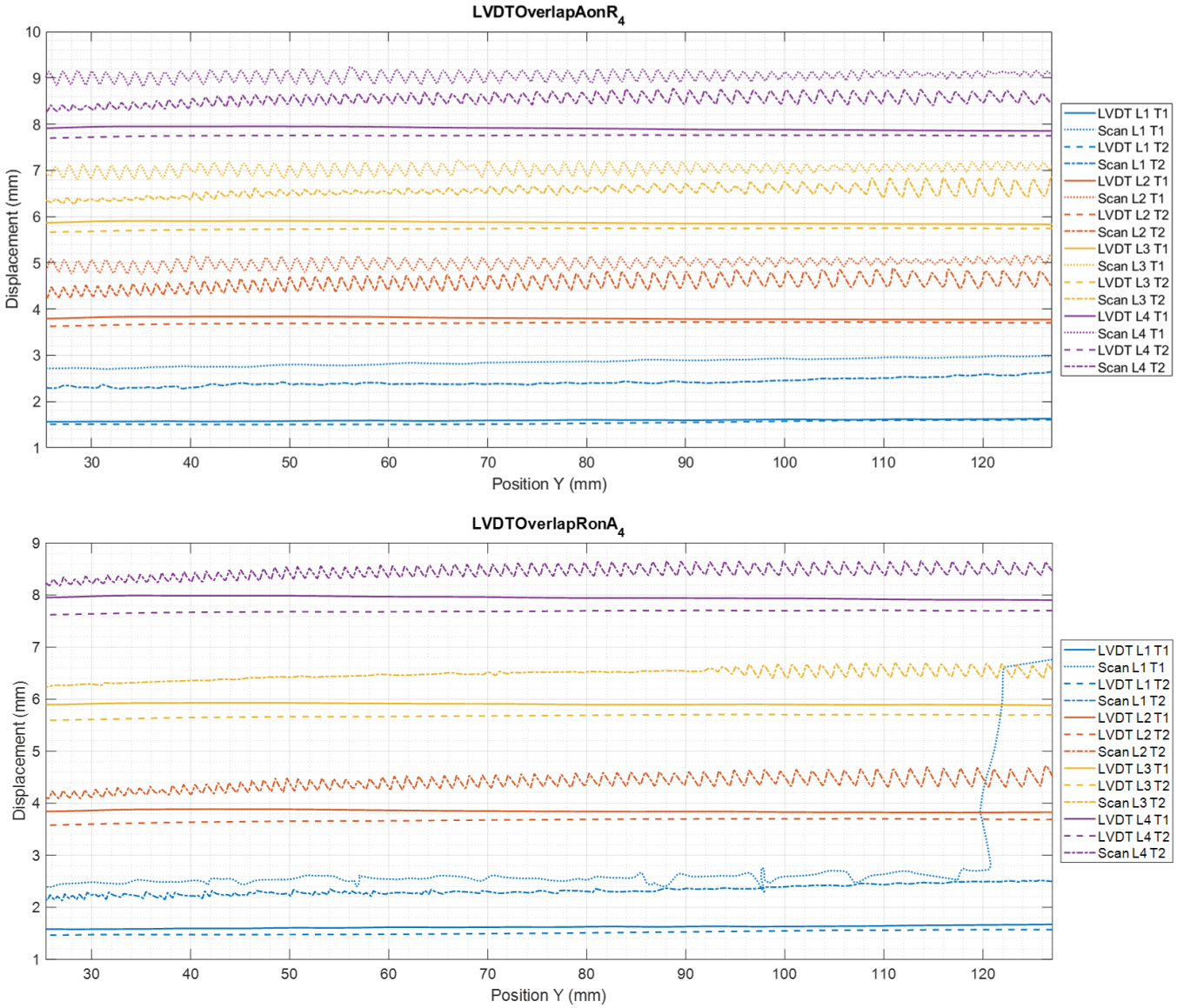


Figure 17: Cross section of real layer height plotted with the measured LVDT displacement data for test number 4 in both directions.

Table 2: Difference between track 1 and track 2 layer heights for every twin track test and measurement method.

Track 1 to track 2 height difference (mm)						
Direction	**Test #**	**Layer**	**Striation Valley Average**	**LVDT Average**	**GOM Average**	**Peak to Valley Average**
A on R	1	1	-	0.03444	0.20207	-
		2	0.39734	0.12731	0.41995	0.40278
		3	0.49679	0.16931	0.54005	0.55423
		4	0.32529	0.18237	0.55483	0.50455
	2	1	-	0.06544	0.22384	-
		2	0.34324	0.16883	0.39760	0.37180
		3	0.38723	0.15393	0.40444	0.40549
		4	0.47209	0.25619	0.47567	0.46453
	3	1	-	0.00979	0.21000	-
		2	0.29953	0.11818	0.33778	0.33426
		3	0.30477	0.15097	0.38982	0.37460
		4	0.38142	0.16971	0.40960	0.40921
	4	1	-	0.06006	0.44869	-
		2	0.46325	0.09999	0.40736	0.41633
		3	0.42868	0.13482	0.47318	0.47226
		4	0.48797	0.15387	0.48696	0.48298
R on A	1	1	-	0.10326	0.09351	-
		2	0.21647	0.18385	0.26460	0.25124
		3	0.31632	0.22865	0.36676	0.34879
		4	0.44430	0.25172	0.45706	0.45196
	2	1	-	0.10134	0.16077	-
		2	0.31786	0.20395	0.34895	0.34551
		3	0.34022	0.14987	0.30017	0.29518
		4	0.46068	0.24701	0.48928	0.47699
	3	1	-	0.04994	0.00491	-
		2	0.36402	0.19413	0.01544	0.38437
		3	0.70500	0.25758	0.02571	0.64903
		4	0.91244	0.31899	0.03258	0.83051
	4	1	-	0.11073	-	-
		2	-	0.17210	-	-
		3	-	0.22512	-	-
		4	-	0.26422	-	-

Table 3: Average striation depth for every track of every twin track test.

		Striation Depth (mm)					
		Layer 2		**Layer 3**		**Layer 4**	
	Test	Track 1	Track 2	Track 1	Track 2	Track 1	Track 2
A on R	1	0.112	0.101	0.173	0.058	0.352	0.293
	2	0.361	0.304	0.205	0.168	0.253	0.268
	3	0.333	0.264	0.421	0.281	0.389	0.333
	4	0.239	0.333	0.258	0.171	0.250	0.260
R on A	1	0.301	0.231	0.357	0.292	0.252	0.236
	2	0.314	0.258	0.314	0.404	0.371	0.338
	3	0.122	0.082	0.089	0.201	0.095	0.258
	4	-	0.246	-	0.203	-	0.233

Quad track builds

The quad track geometry was chosen to simulate a larger build with multiple overlaps and the alternating directional scheme was implemented to test the effectiveness of a common path planning strategy which is to alternate direction. Images of the completed build in the A on R and R on A direction are found in the previous section in **Figure 12**, and an image of the alternating build is found in **Figure 18**. Frames of the 3D scans for layers 1, 4, 5, and 8 are shown in **Figure 19**. Visually in comparison of the builds the only notable change between tracks was in the single directional samples as the squeeze flash generation was much worse between the 1st and 2nd tracks than between the 2nd and 3rd tracks or the 3rd and 4th tracks. This difference is especially clear in the R on A sample. Scan cross sections of all layers of all samples in the XZ plane are shown in **Figure 20**. From that figure, it is observed that the single direction samples at higher layers have a greater layer height on the first track, subsequently decreasing with track number. The alternating sample, however, exhibits the most stable behavior with the most consistent layer height. The impact of the layer height change between the tracks is much more severe in the R on A case. Even for the unidirectional samples, there is a limit for the change in layer height as the tool deflection will not go negative. Another way to limit tool deflection would be a stiffer system.

In general, further testing should be done with failure point analysis, but in the 8 layers deposited the volume of flash did not worsen, even in the R on A samples, and no evidence for future failure is shown. Therefore, the methods successfully allowed for the completion of all quad track builds and were helped by alternating the layer directions.



Figure 18: Image of completed quad track build with alternating layer path direction.

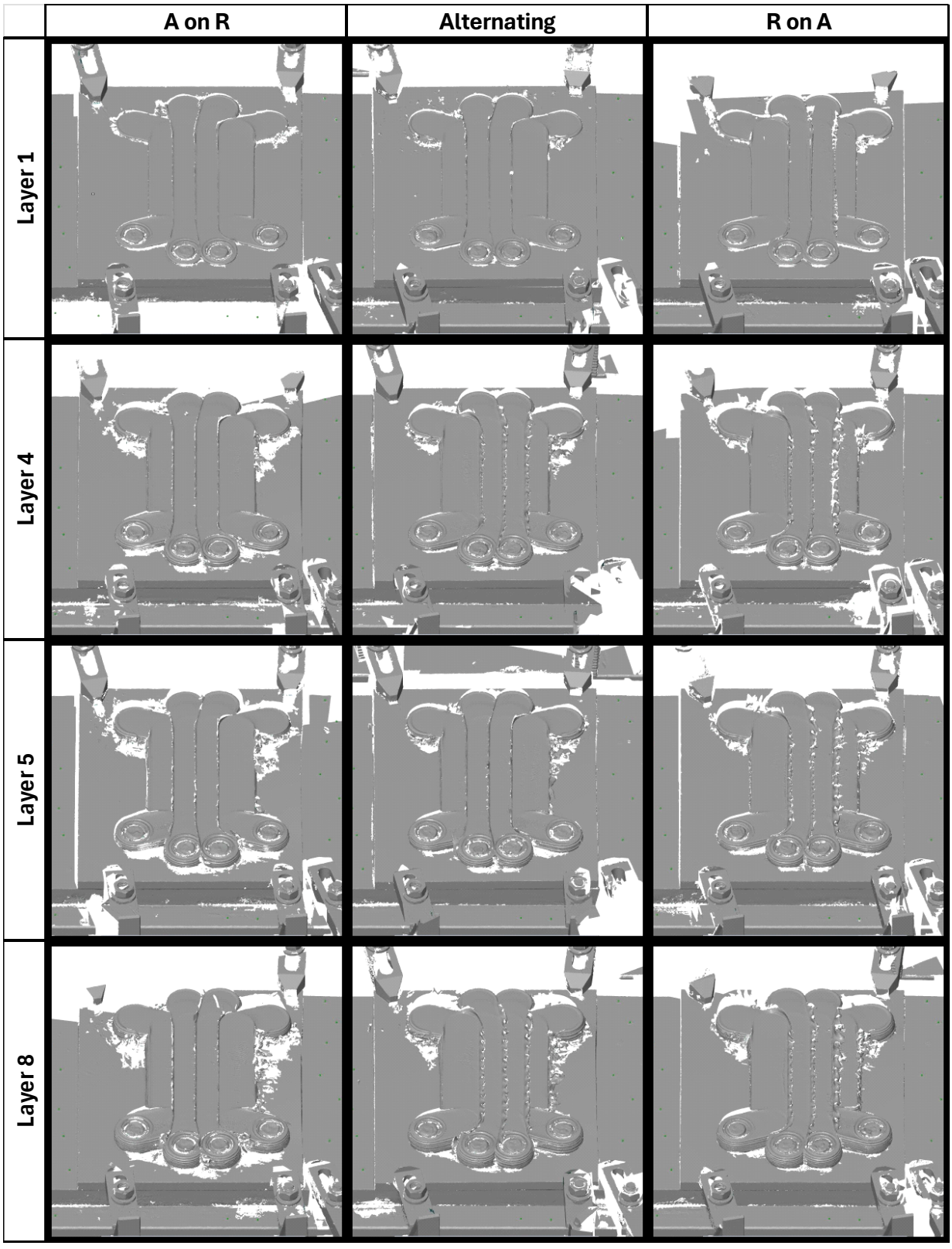


Figure 19: Collage of scan frames for layers 1, 4, 5, and 8 of all quad track builds.

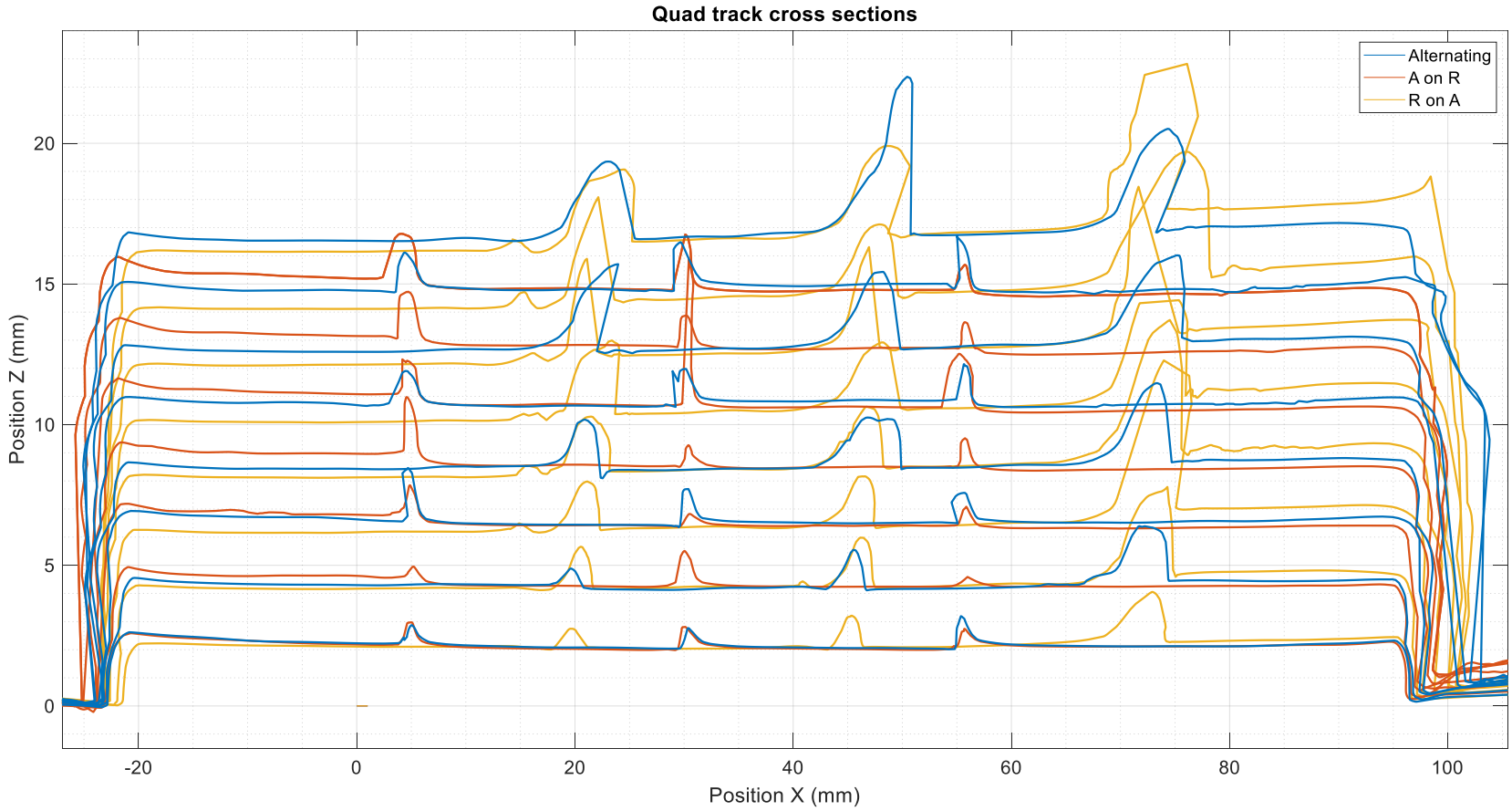


Figure 20: XZ plane cross section of all quad track build for all layers.

Conclusion

A method was proposed to reduce squeeze flash generation in overlap condition in AFSD by determining appropriate process feed rates, either material feed rate or tool traverse feed rate, by calculating the appropriate volume of material required. This method was then validated through two track build testing over two print directions (advancing onto retreating, and retreating onto advancing), four overlap conditions, and through three quad track builds at the same overlap one advancing onto retreating, one retreating onto advancing, and one which alternated between directions. The method allowed limited flash generation for all overlaps in the A on R case and for all reasonable overlap cases in R on A. It was also demonstrated that path planning methods can further reduce squeeze flash generation. The inclusion of open or closed-loop layer height control may also decrease squeeze flash generation in overlapping tracks. This research is motivated by the need for further path planning research in AFSD and this study helps to address the knowledge gap in process planning in overlap conditions.

Future work

Several studies from this research could be done to broaden the results including:

- Testing with the traverse feed rate (TFR) compensation method or some combination of the TFR and material feed rate (MFR) compensation methods.
- Investigation advancing onto advancing and retreating onto retreating overlaps which may require some testing on parameter relationship to advancing side material placement preference.
- Research into open or closed loop feedback control of layer height may also refine the results.
- Further efforts can also expand these studies towards curvilinear pathing.
- The impact of overlap parameter changes on the resultant material properties should also be explored.
- The impact of machine stiffness on process stability.
- Exploration of parameters of that impact the material which is favorably placed towards the advancing side of each track.

Z-lift compensation

Introduction

In the manuscript prior, it was discussed that changes in process forces change the displacement of the non-ridged AFSD system impacting the layer height of a track especially in an overlap where process parameters are changing. This change in layer height exacerbates the generation of squeeze flash and alters layer shape and material placement. Since layer height is a fundamental assumption in AM if a given process does not tend towards layer height stability builds tend towards underbuilding or overbuilding which can impact resultant material properties. An example of this reaction is seen in the following test where a range of overlap amounts were tested in a single sample. The deposit, **Figure 21**, has ten parallel paths where the initial distance between tracks is 45 mm. Each subsequent path distance decreases by 5 mm per step with a final distance of 5 mm. The start positions of each parallel track are offset such that the tool does not contact the prior track during startup. Six layers were deposited using a MELD Manufacturing L3 using a 12.7 mm (0.5 in) square rod discrete feed system. The Al 6061-T6 rods were coated in a carbon graphite lubricant. The nominal process parameters were $TFR = 254\ mm/min$ $(10\ ipm)$, $MFR = 152.5\ mm/min$ $(6\ ipm)$, and $h = 2\ mm$ $(0.080\ in)$. MFR was the parameter was adjusted in the overlaps. PID control was used on the build to maintain tool face temperature at $T_{tool} = 420\ °C$. The tool face had four teardrop shaped nubs protruding from the surface to a depth of 2.3 mm (0.090 in). During the deposit, squeeze flash was generated on the final three tracks. This was discovered to be related to the decrease in force over each track, **Figure 23** which is a spatial plot of actuator force from recorded machine data. This resulted in a reduction in layer height shown in **Figure 22**. The print height plot was generated using cross sections from a 3D structed light scan. The future work section of the manuscript discussed the inclusion of open or closed loop control for layer height. This section discusses the use of open loop control to determine the overall impact of controlling layer height on flash formation.

Testing and results

Based on the twin track builds from the prior section, tests 2 and 3 (shown in **Table 1**) are repeated for each direction as these were considered to be the most realistic overlaps as test number 1 may not always be substantial enough of an overlap to guarantee bonding and test number 4 is an extreme amount of overlap. Compensation amounts are selected for the desired

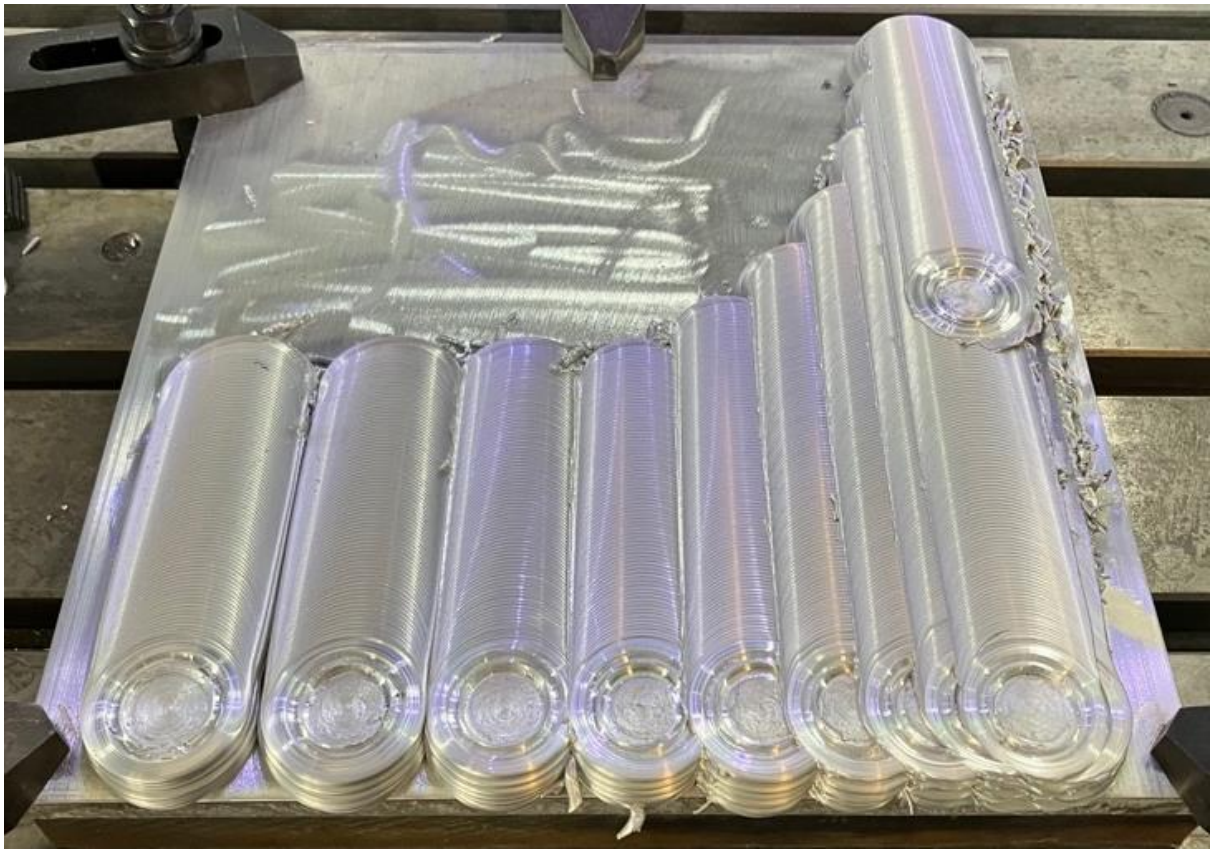


Figure 21: Image showing completed test of linear overlap compensation method over increasing overlap.

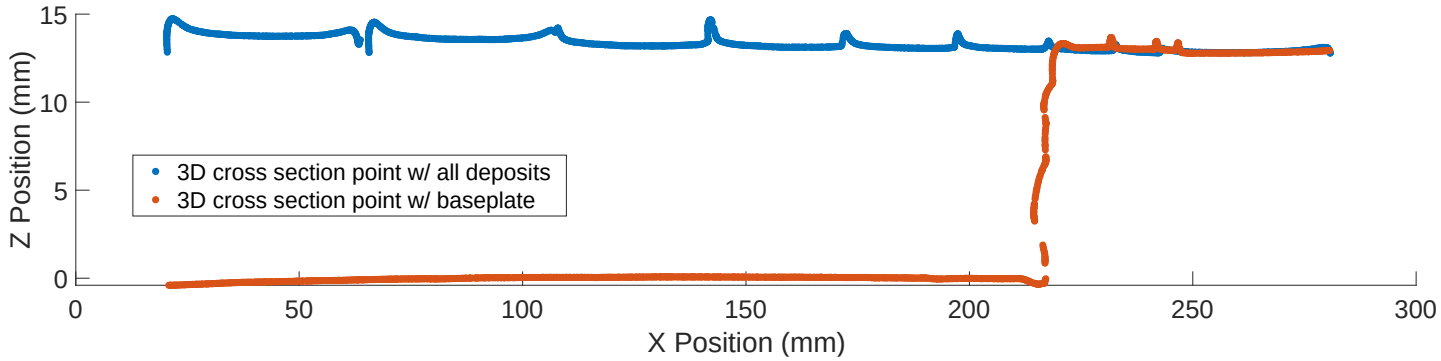


Figure 22: Plot showing a cross section of print height compared to the baseplate taken from a 3D structured light scan.

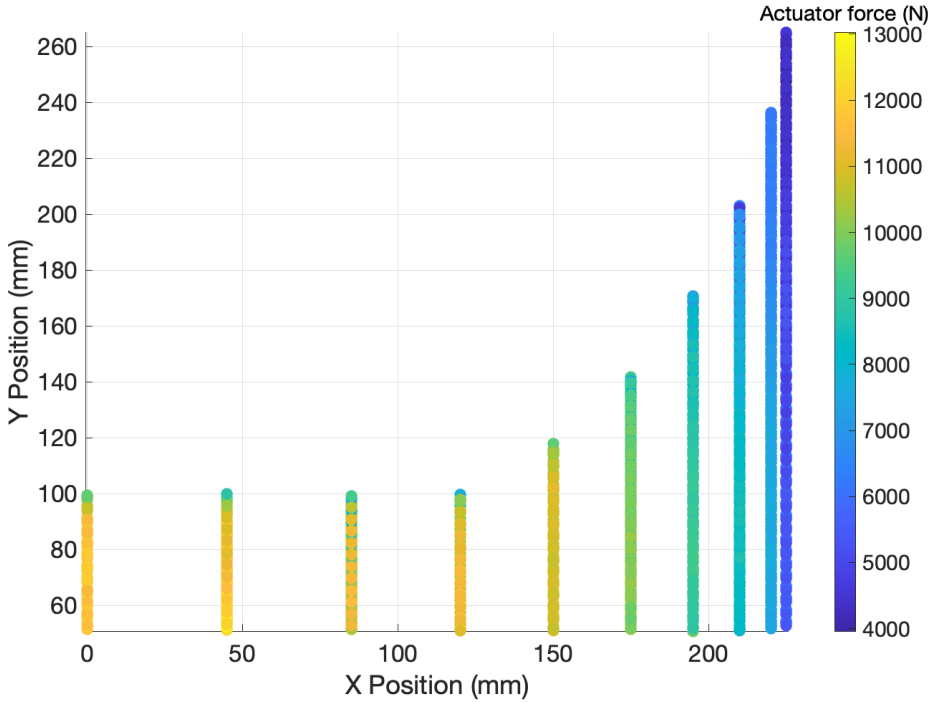


Figure 23: Spatial plot showing actuator force in different print locations.

track 2 height (nominal track height). Images of the completed builds are shown in **Figure 24**. The compensation parameters that were used and the tabulated summary of results are shown in **Table 4**. The plotted results for the A on R 2 test are shown in **Figure 25**. The plotted results for the A on R 3 test are shown in **Figure 26**. The plotted results for the R on A 2 test are shown in **Figure 27**. The plotted results for the R on A 3 test are shown in **Figure 28**.

To visual observation, the test number 2 sample for both directions have little change from the control test samples. This may be because the amount of flash produced in these cases was already minimal. The test number 3 samples however show a sharp decrease in in squeeze flash generation. Interpreting the LVDT data shows that the impact of the cantilever deflection was greatly reduced and even overcompensated for on the first layer reducing the overall difference in track heights from well above $100\ \mu m$ to often well below. In the 3D scan data, however, layer 1 saw improvement in all except A on R 3, but layer 4 saw a slightly more significant increase in track difference the exception of R on A 3 which saw improvement on every layer. Further investigation is required to elucidate the reason behind this difference though the scope of this study is to improve flash generation.

Spatial plots of the change in actuator force between the compensated and uncompensated tests are shown for the A on R 2 direction and overlap condition in **Figure 29**, for the A on R 3 direction and overlap condition in **Figure 30**, for the R on A 2 direction and overlap condition in **Figure 31**, and for the R on A 3 direction and overlap condition in **Figure 32**. From the force plots, it can be observed that in general the required process actuator force decreased in the 2nd track, but the variation in that force decreased greatly for all tests.

Conclusions

From the presented tests it can be shown that applying layer height compensation can reduce squeeze flash generation and mitigate changes in layer height. As a side effect, the process actuator force also stabilizes in the 2nd track of a twin track build as the force variation decreases. Future work should include testing the quad track build to verify this solution with multiple tracks and the measurement of the total process change. Research should also be completed on closed loop control schemes for layer height or modulation of feed parameters to adjust total z directional force.

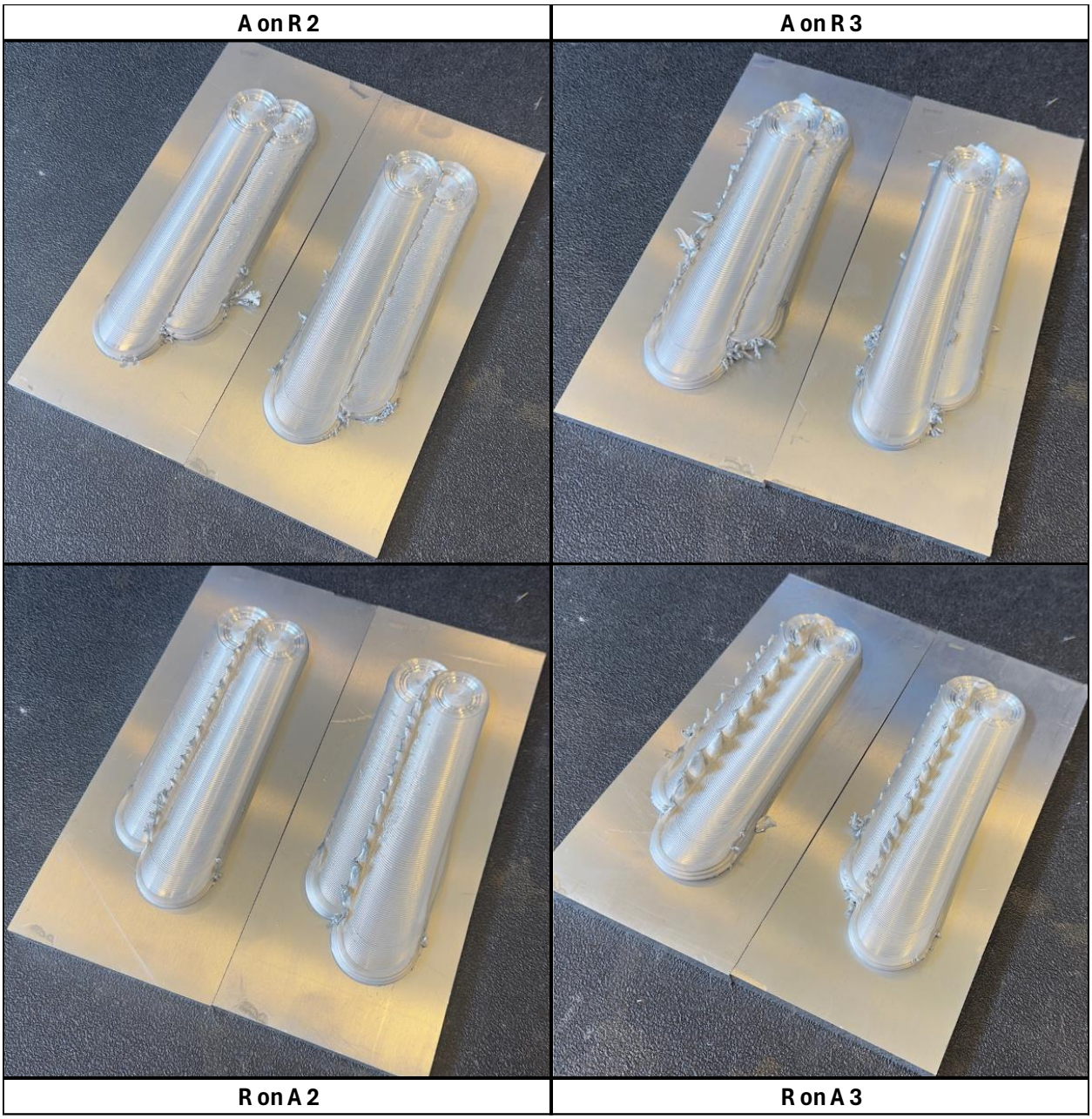


Figure 24: Images of completed layer height compensated for twin track builds next to their respective uncompensated builds. Uncompensated on the left and compensated on the right.

Table 4: Height compensation amounts for each test.

Average measured difference in track 1 to track 2 layer height (mm)									
Test overlap & direction	**Compensation amount**	**Average difference LVDT**				**Average difference 3D Scan**			
		Layer 1	Layer 2	Layer 3	Layer 4	Layer 1	Layer 2	Layer 3	Layer 4
A on R 2	0	0.065	0.169	0.154	0.256	0.224	0.398	0.404	0.476
	0.183	-0.072	0.004	0.057	0.092	0.077	0.302	0.456	0.554
A on R 3	0	0.010	0.118	0.151	0.170	0.210	0.338	0.390	0.410
	0.244	-0.066	-0.020	0.033	0.028	0.239	0.362	0.467	0.513
R on A 2	0	0.101	0.204	0.150	0.247	0.161	0.349	0.300	0.489
	0.224	-0.032	0.076	0.119	0.153	0.107	0.294	0.450	0.509
R on A 3	0	0.050	0.194	0.258	0.319	0.125	0.392	0.653	0.828
	0.262	-0.080	0.004	0.048	0.102	0.112	0.232	0.366	0.484

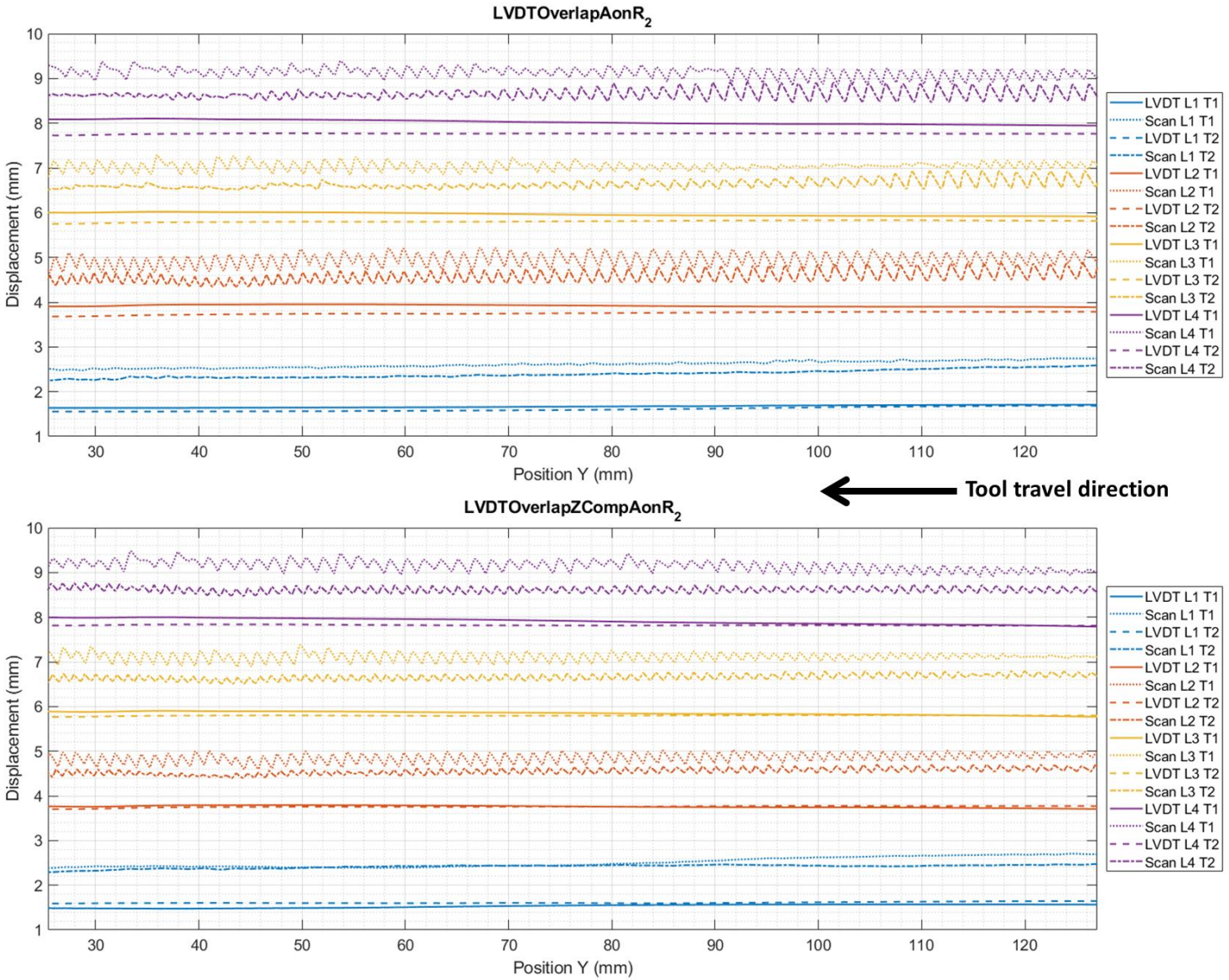


Figure 25: Plotted results of the open loop compensation of A on R test 2.

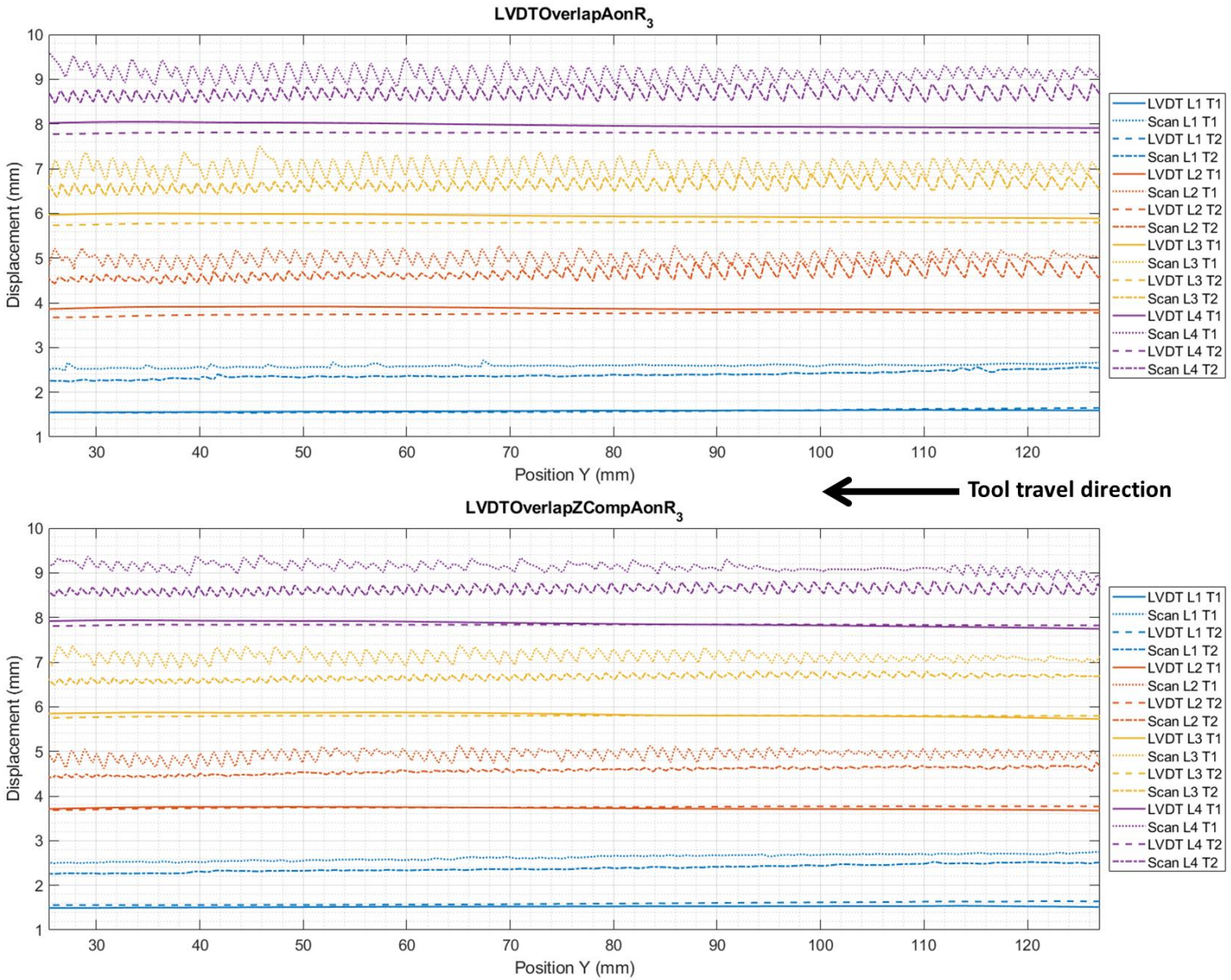


Figure 26: Plotted results of the open loop compensation of A on R test 3.

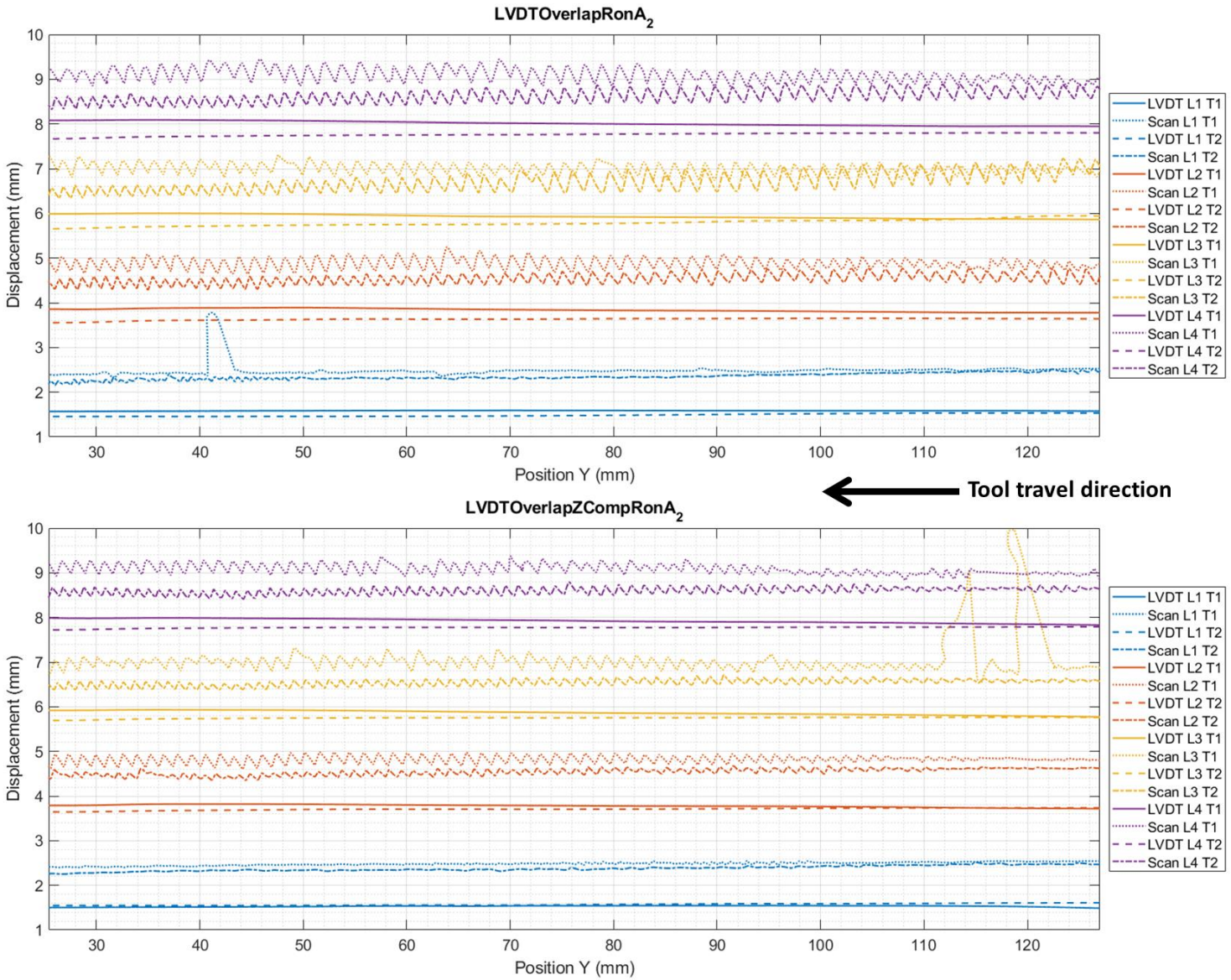


Figure 27: Plotted results of the open loop compensation of R on A test 2.

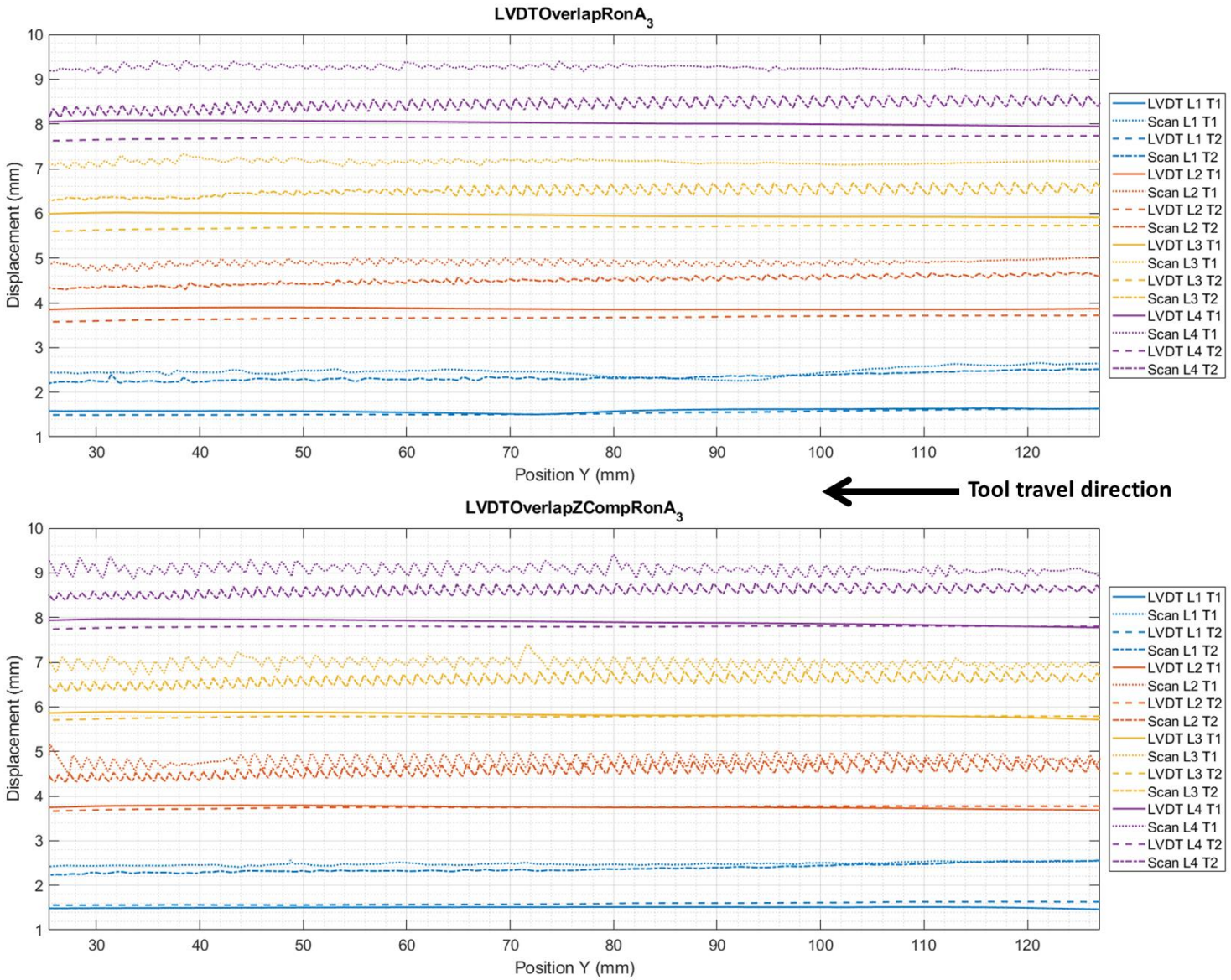


Figure 28: Plotted results of the open loop compensation of R on A test 3.

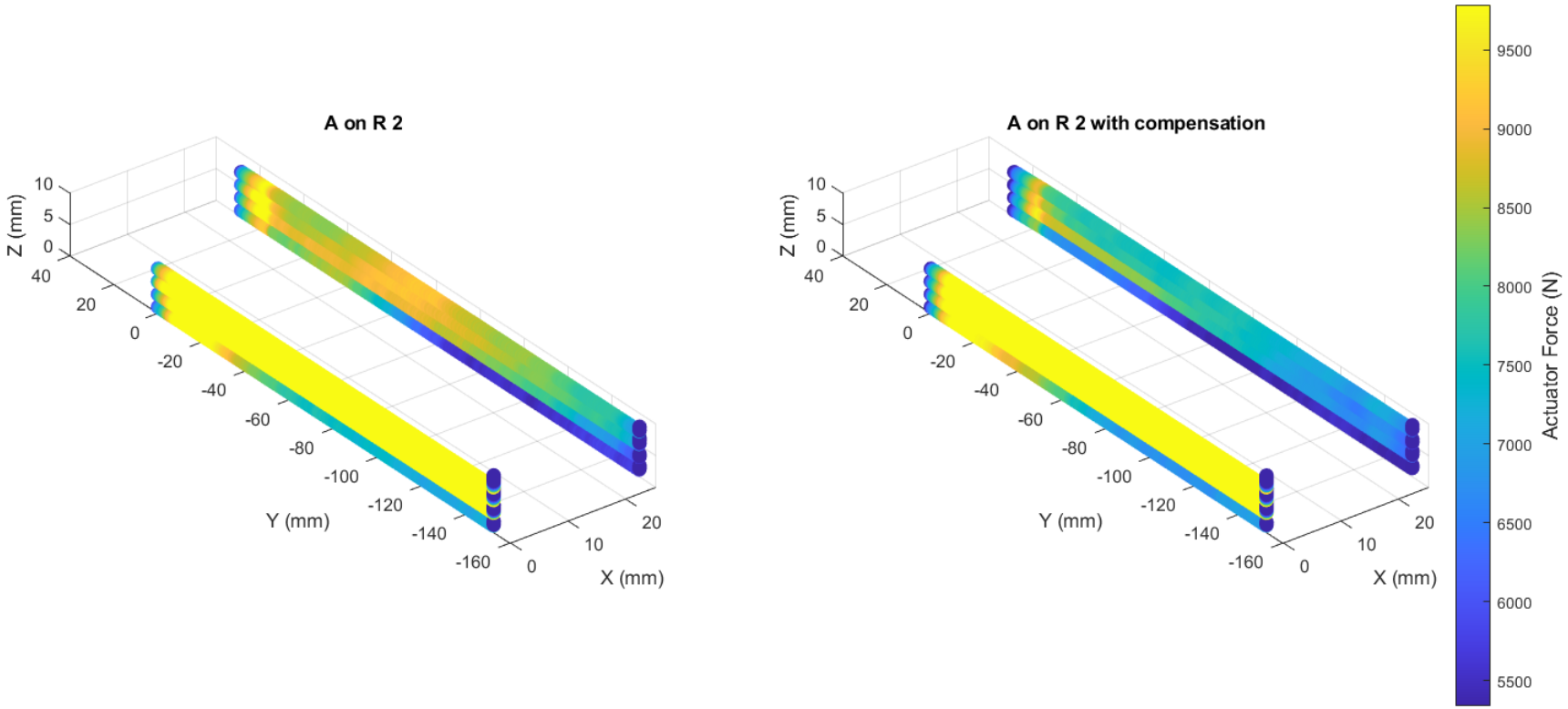


Figure 29: Spatial plot colored by process actuator force for the A on R 2 test and direction with layer difference compensation on the right.

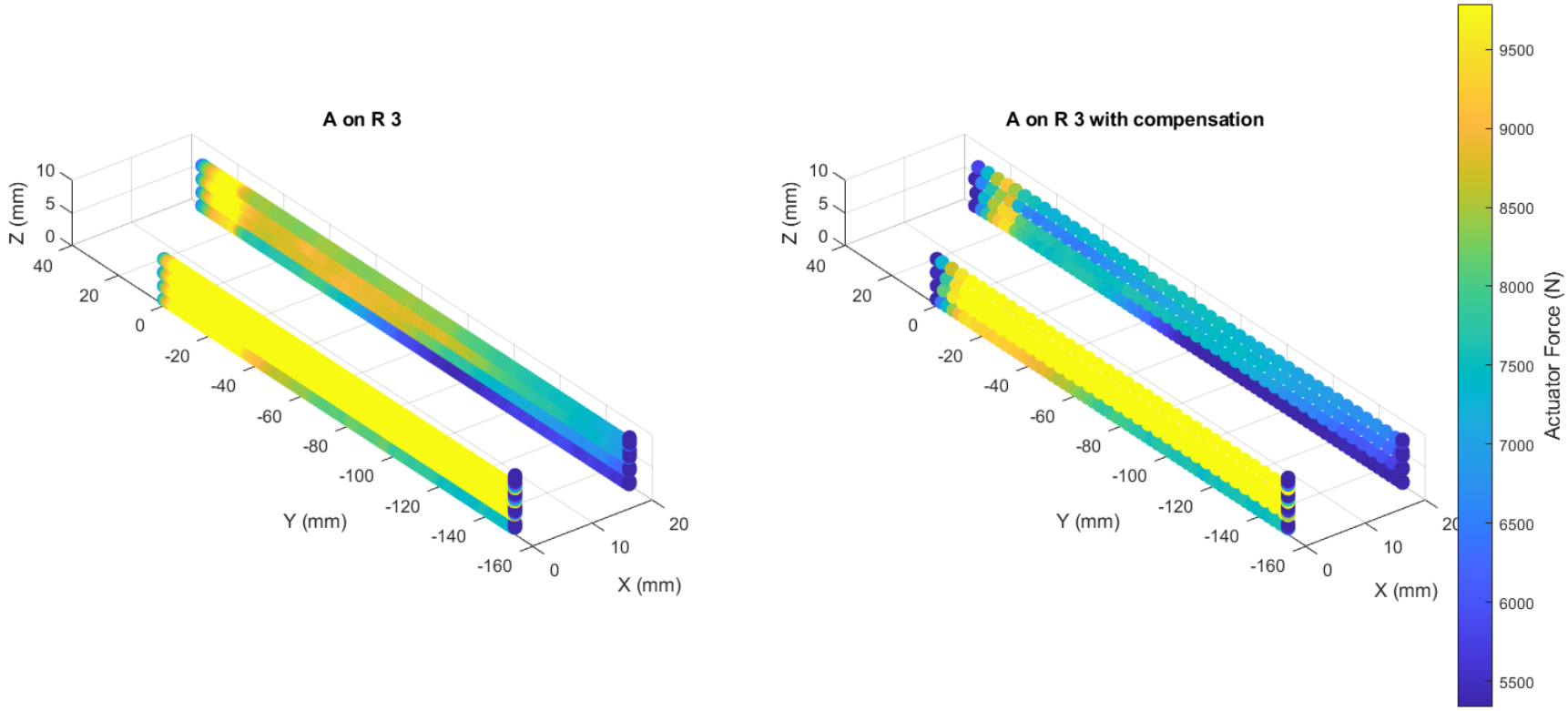


Figure 30: Spatial plot colored by process actuator force for the A on R 3 test and direction with layer difference compensation on the right.

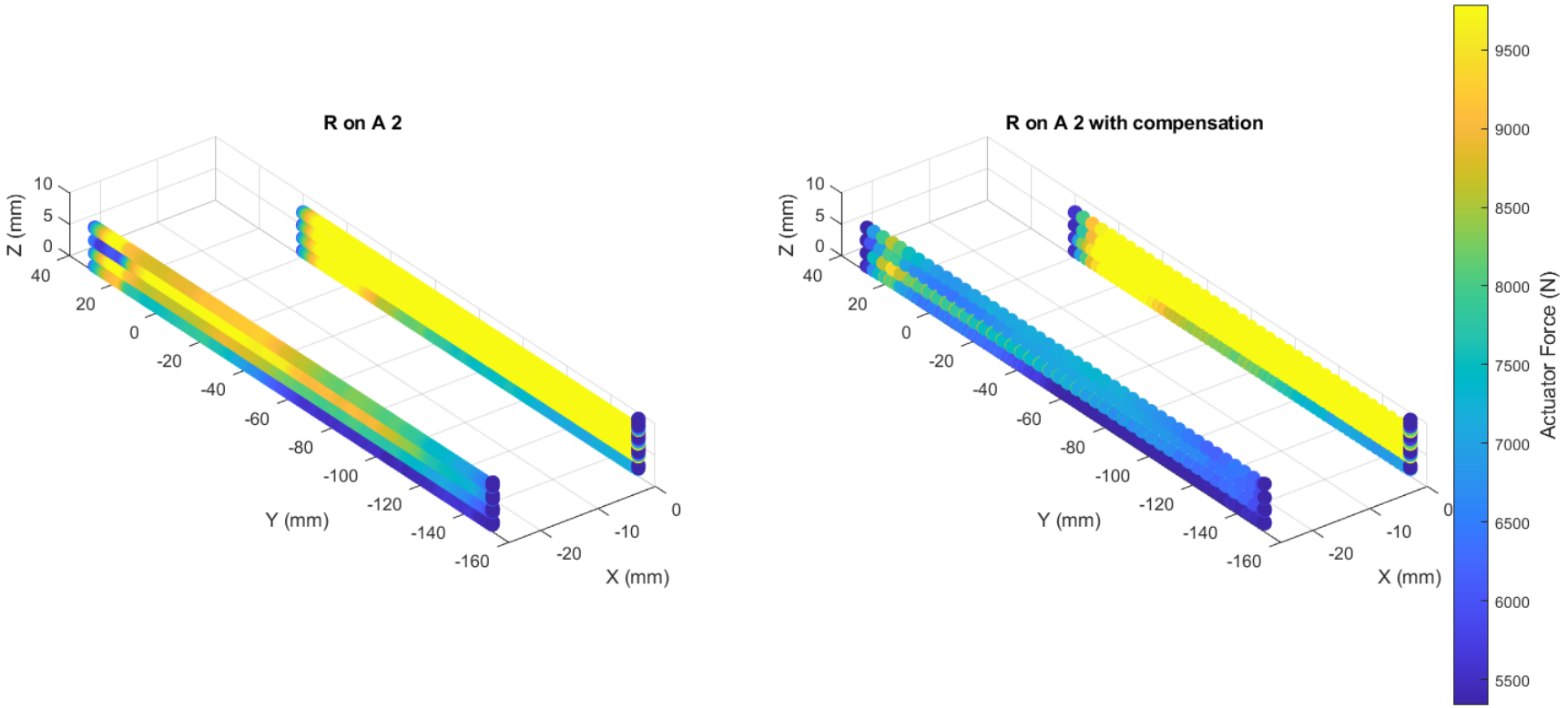


Figure 31: Spatial plot colored by process actuator force for the R on A 2 test and direction with layer difference compensation on the right.

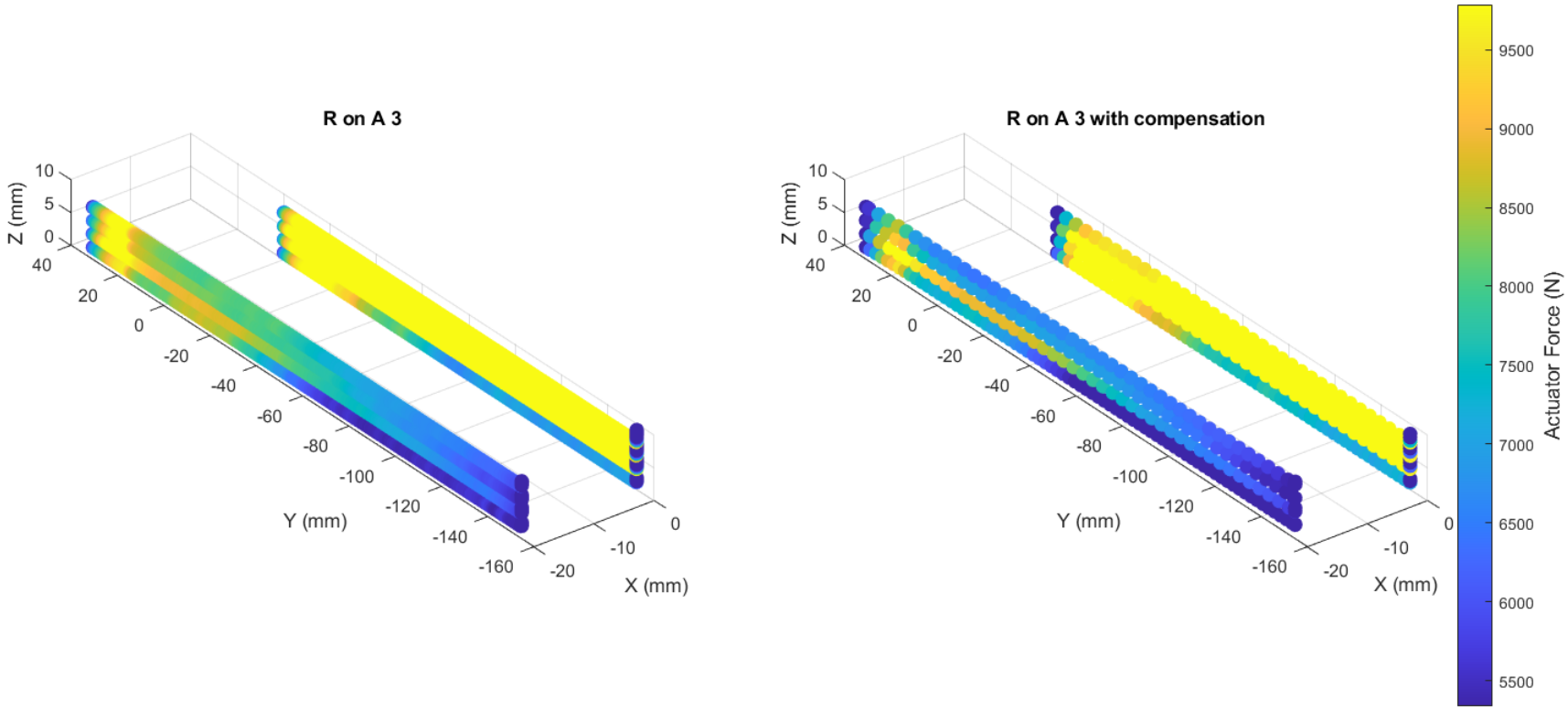


Figure 32: Spatial plot colored by process actuator force for the R on A 3 test and direction with layer difference compensation on the right.

Curvilinear overlap methods:

To continue the work done in the linear overlap method, a curvilinear method is described and initially validated with an Archimedes spiral print. For larger scale build simulation in collaboration with the US Army Ground Vehicle Systems Materials Engineering Directorate (GVME) conducted trials at the Advanced Manufacturing Commercialization Center on their hybrid Jointless Hull Subsection Tool (JHSST) using this method to simulate the production of large-scale components using AFSD. Images of trial builds have been included in this document.

Method

Due to the relatively wide tracks deposited in AFSD (typically 38-50mm), toolpath curvature introduces nonlinear effects on volume placement during deposition such that the volume on each side of the toolpath centerline cannot be assumed equal. A new method must be derived for curvilinear toolpaths. Since any curve can be well approximated using a series of circular arcs, the new method will be based on an overlap condition for a circle segment. The curvilinear overlap method will use an analysis of covered and uncovered areas to calculate an effective track width relative to the nominal track width. The general relationship is shown in Equation 8. The u subscript references uncovered while the c subscript references covered. A specific relationship will be derived for area in circular arcs as shown in **Figure 33** and **Figure 34**.

$$w_u = w\frac{Area_u}{Area_u + Area_c} \qquad (8)$$

Two cases are considered. Case 1 represents the situation where the radius of the initial track is less than the overlapping track $R_1 < R_2$, and case 2 where $R_1 > R_2$, as shown in **Figure 34**. R_o is the outer radius of the overlapping track, R_i is the inner radius of the overlapping track, and R_p is the interacting radius of the prior track. Relevant expressions for each case are provided. The derivation of the final equation for both cases is shown in **Table 5**. For both cases, the difference between R_2^2 and R_1^2 must be positive. So, a simplified final equation that applies to both cases is shown in Equation 9.

$$w_u = w\frac{|R_2^2 - R_1^2| + w(R_2 - R_1)}{2R_2 w} \qquad (9)$$

Substituting Equation 2 and simplifying subscript convention gives Equation 10.

$$\frac{MFR_2}{TFR_2} = \frac{MFR_1}{TFR_1}\frac{|R_2^2 - R_1^2| + w(R_2 - R_1)}{2R_2 w} \qquad (10)$$

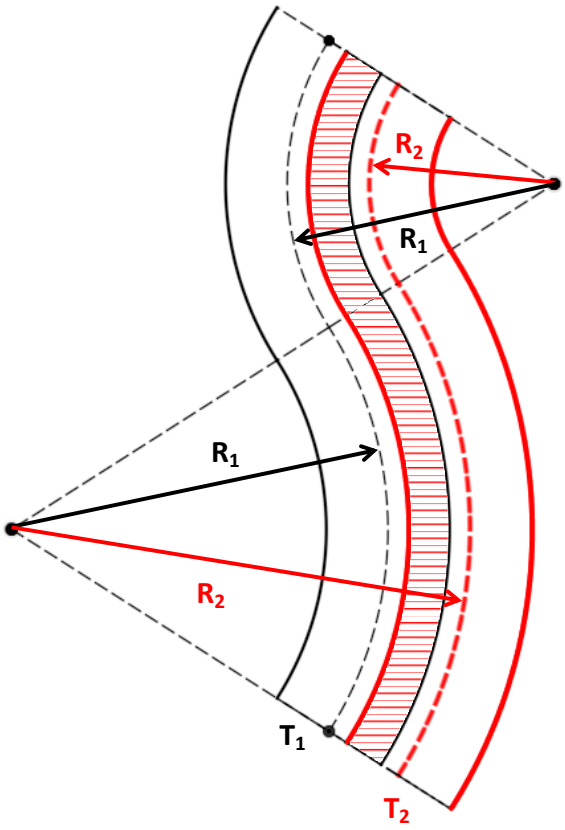


Figure 33: Example of continuous curvilinear path.

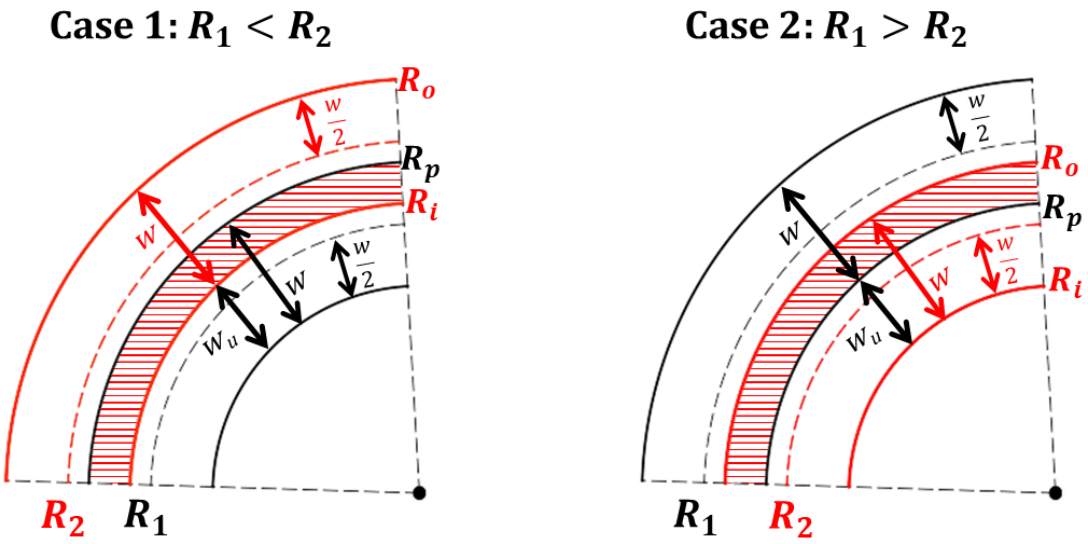


Figure 34: Visual description of the 2 governing cases for circular overlaps where the shaded area is the covered area.

Table 5: Derivation of both cases for circular overlaps.

Case 1: $R_1 < R_2$		**Case 2: $R_1 > R_2$**	
$w_u = w\frac{\pi R_o^2 - \pi R_p^2}{\pi R_o^2 - \pi R_i^2}$	$R_o = R_2 + \frac{w}{2}$ $R_i = R_2 - \frac{w}{2}$ $R_p = R_1 + \frac{w}{2}$	$w_u = w\frac{\pi R_p^2 - \pi R_i^2}{\pi R_o^2 - \pi R_i^2}$	$R_o = R_2 + \frac{w}{2}$ $R_i = R_2 - \frac{w}{2}$ $R_p = R_1 - \frac{w}{2}$
$w_u = w\frac{\left(R_2 + \frac{w}{2}\right)^2 - \left(R_1 + \frac{w}{2}\right)^2}{\left(R_2 + \frac{w}{2}\right)^2 - \left(R_2 - \frac{w}{2}\right)^2}$		$w_u = w\frac{\left(R_1 - \frac{w}{2}\right)^2 - \left(R_2 - \frac{w}{2}\right)^2}{\left(R_2 + \frac{w}{2}\right)^2 - \left(R_2 - \frac{w}{2}\right)^2}$	
$w_u = w$ $\frac{\left(R_2^2 + R_2 w + \frac{w^2}{4}\right) - \left(R_1^2 + R_1 w + \frac{w^2}{4}\right)}{\left(R_2^2 + R_2 w + \frac{w^2}{4}\right) - \left(R_2^2 - R_2 w + \frac{w^2}{4}\right)}$		$w_u = w$ $\frac{\left(R_1^2 - R_1 w + \frac{w^2}{4}\right) - \left(R_2^2 - R_2 w + \frac{w^2}{4}\right)}{\left(R_2^2 + R_2 w + \frac{w^2}{4}\right) - \left(R_2^2 - R_2 w + \frac{w^2}{4}\right)}$	
$w_u = w\frac{R_2^2 - R_1^2 + R_2 w - R_1 w}{2R_2 w}$		$w_u = w\frac{R_1^2 - R_2^2 + R_2 w - R_1 w}{2R_2 w}$	

Simplifying for limiting cases gives Equations 11 and 12.

$$MFR_2 = MFR_1 \frac{|R_2^2 - R_1^2| + w(R_2 - R_1)}{2R_2 w} \tag{11}$$

$$TFR_2 = TFR_1 \frac{2R_2 w}{|R_2^2 - R_1^2| + w(R_2 - R_1)} \tag{12}$$

A graph of the behavior of Equation (9) as a function radius and overlap can be found in **Figure 35**.

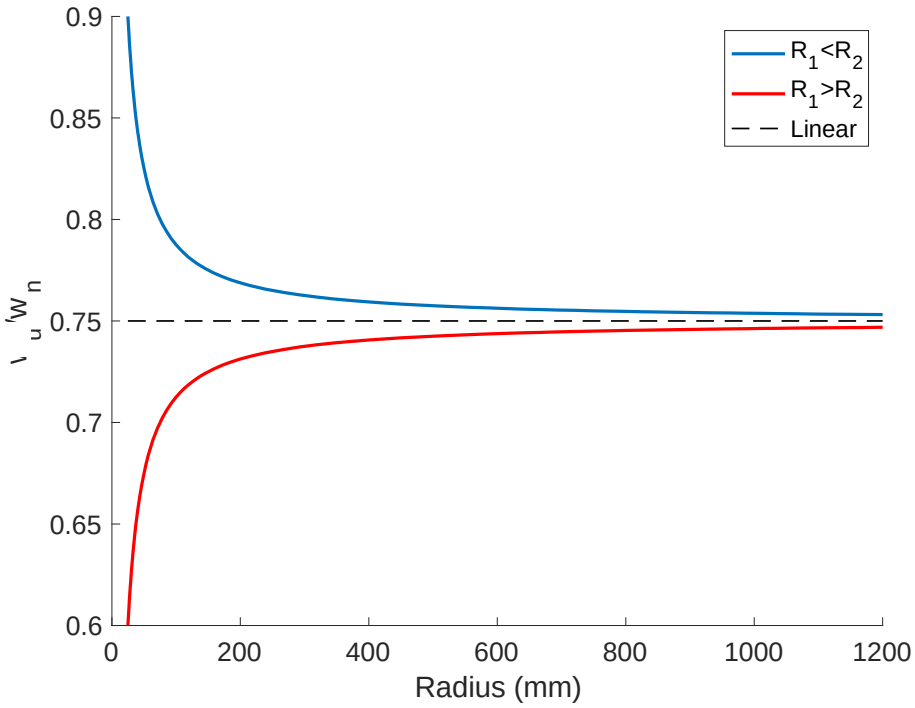


Figure 35: Curvilinear overlap considering a track with a nominal width of 40 mm and a distance between tracks of 30 mm. The radius that is displayed on the X-axis is the value of the larger radius for each case (e.g., if $R_1 > R_2$ than the radius input for that line is R_1).

Validation

To validate this method, circular arcs were fit onto an Archimedes spiral, and with the comparison of radii, Equation 11 was used to compensate feed parameters. The g-code script was generated such that the radius of the spiral increases by 25.4 mm every full rotation; five layers were deposited in alternating directions using a MELD Manufacturing L3 equipped with a 12.7 mm (0.5 in) square rod discrete feed system. The substrate and feed material were AA6061-T6 the feed material was coated in a carbon graphite lubricant. The nominal process parameters were $TFR = 254\ mm/min$ $(10\ ipm)$, $MFR = 152.5\ mm/min$ $(6\ ipm)$, and $h = 2\ mm$ $(0.080\ in)$. MFR was the parameter was adjusted in the overlaps. PID control was used on the build to maintain tool face temperature at $T_{tool} = 420\ °C$. The tool face had four teardrop shaped nubs protruding from the surface to a depth of 2.3 mm (0.090 in). During the deposit, there was no evidence of underfeeding, and excess squeeze flash was only generated in the five reload locations which occurred due to the discrete feed system requiring a mid-layer reload. The operator only engaged in the process during the reload process. An image of this is shown in **Figure 36**.

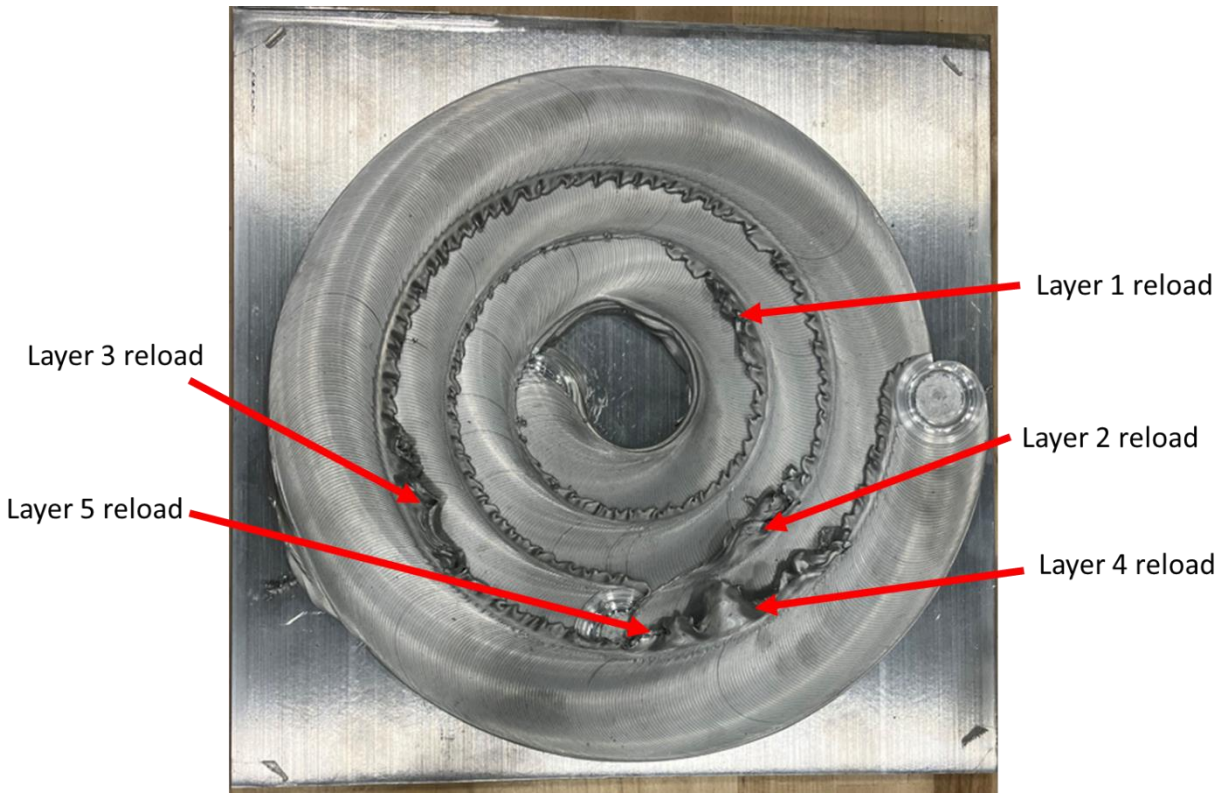


Figure 36: Image of completed Archimedes spiral build with indicators for all reload location which created squeeze flash

The method was also demonstrated at GVME using a MELD manufacturing continuous feed system to trial for full-scale production. Two builds were completed. The first is a larger Archimedes spiral, **Figure 37**. This build was completed in AA6061-T6 and the bars were coated in a carbon graphite lubricant. The final path radius is 300 mm (11.8 in), and initial path radius is 173 mm (6.8 in). Distance between subsequent tracks is 31.75 mm (1.25 in). The second is a large raftlike structure with linear overlapping straight sections and curvilinear corners, **Figure 38**. This build was completed in AA6061-T6 without graphite using the *TFR* adjustment method. 80 Layers at 3 mm height, ~2,200 feed rods, ~600 kg (1320 lbs) of deposited material, 45 total print hours, with a track distance of 31.75 mm (1.25 in). The nominal parameters were $TFR = 540\ mm/min$ and $MFR = 480\ mm/min$. Both builds were completed with minimal allowed squeeze flash generation. Notable squeeze flash locations in the Archimedes spiral build are due to graphite buildup between bar segments becoming dislodged and interrupting the build process. The raftlike build includes several days of deposition at nearly the maximum system feed rate for many layers.



Figure 37: Large Archimedes spiral completed at the Additive Manufacturing Commercialization Center under GVME as a trial build.

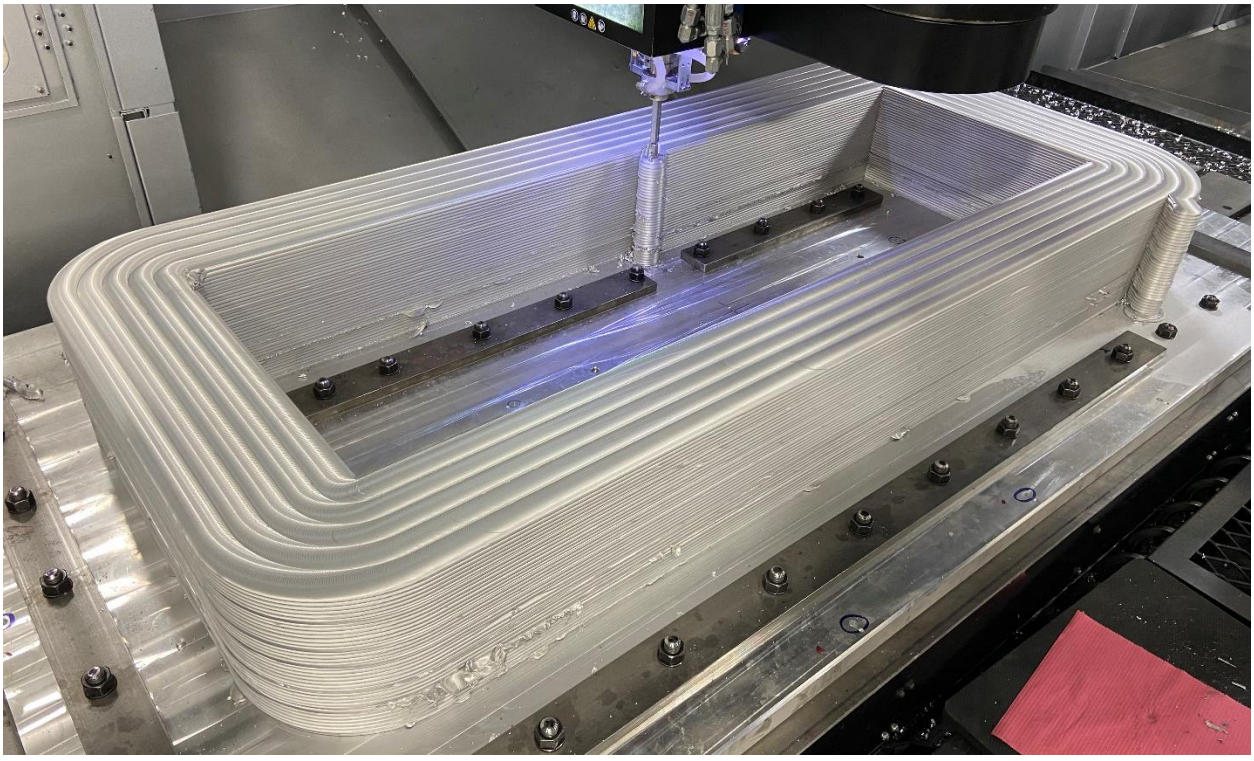


Figure 38: Large raftlike build completed at the Additive Manufacturing Commercialization Center under GVME as a trial build. Courtesy of [74]. DISTRIBUTION STATEMENT A. Approved for public release; distribution is unlimited. OPSEC#9245.

Conclusion and future work

A method for compensating feed rates in curvilinear overlaps in AFSD has been derived and shown to successfully complete an Archimedes spiral build along with several full-scale components and is currently being utilized for production scale testing by GVME and their collaborators.

CHAPTER 4: ROBUST LEAST SQUARES ARC FITTING METHOD OF ORDERED POINT FOR PATH PLANNING IN ADDITIVE MANUFACTURING

Introduction

This Chapter includes a manuscript currently in draft form detailing a method for fitting arcs to ordered point coordinate data. This is included in this dissertation as information about component geometry is required to apply the correct overlap method as discussed in Chapter 3. Currently in most slicing processes for AM, which takes input of a simplified mesh, the model curvature information is lost. This method allows for much of that information to be reclaimed. This method is incorporated into the larger automated path planning framework.

Manuscript author contributions:

Joshua Kincaid: derived the method, wrote the original draft, and was responsible for data collection and interpretation.

Michael Borish: provided helpful technical feedback, assisted in editing the document and contributed several test cases.

Tony Schmitz: edited the manuscript and provided technical advising.

Robust least squares arc fitting method of ordered point for path planning in additive manufacturing

Joshua Kincaid[1], Michael Borish[2], Tony Schmitz[1,2]

[1]The University of Tenneessee, Knoxville

[2]Oak Ridge National Laboratory, Manufacturing Demonstration Facility

Abstract:

Traditional slicing in additive manufacturing (AM) takes input of simplified triangulated mesh as they are a widely supported, low-complexity format for geometric data representation. However, representing surfaces solely with linear segments often produces faceted part surfaces and can necessitate an excess of motion commands to capture the intended geometry. Moreover, losing explicit curvature data limits the ability to tailor process parameters to specific features. While certain hybrid or CAM solutions do incorporate curved motion commands, these capabilities are not yet widespread in AM slicers. To address this issue, this paper proposes an arc fitting method for use in AM path planning that takes input of the ordered points output by slicing and sections the data into three geometric primitives which are either an arc, a line, or a corner. Arc fitting is accomplished through a least squares approach, which is followed by a refinement step to conserve path continuity. This arc fitting process avoids many ambiguities that are symptomatic of path planning for AM process geometries.

Introduction:

In additive manufacturing (AM), the process of producing a part can normally be divided into three component environments: design, slicing, and printing. In the design environment, a conceptualized part modeled as a fully defined 3D solid in a computer aided design (CAD) software, then the solid 3D model is simplified into a mesh (typically a stereolithography or STL filetype) via a process called tessellation or triangularization. This is done as STLs are open source and are a basic representation of the intended geometry. Also, it is often more computationally efficient to offset and cross section the explicit part representation than the fully defined implicit model. The tessellation of a fully defined model into an STL, however, causes the loss of curvature or geometric information. In the slicing environment, the mesh is sliced (or cross sectioned) into layers and the cross section is filled by a planned toolpath. Then, user or manufacturer determined process parameters are injected, and a toolpath is generated, which is often in the form of g-code which is a standardized set of instructions for computer-controlled machines that instruct a controller what coordinate to move to and how fast. The g-code file is then uploaded into the printer environment and executed to produce the near-net or net shaped component. The geometric simplification and loss of curvature information means that the majority of g-code files are executed by only linear moves causing the resultant surface to be faceted, and, therefore, the surface quality of as-printed parts is limited to the resolution of the mesh. Additionally, a printer's computational capacity can restrict the maximum mesh resolution. Sending an excessive number of movement commands over a short time may cause stuttering, which disrupts the material deposition to travel rate ratio changing layer shape, height, and impacting machine kinematic stability thereby increasing the risk of print failure [43], [44].

These issues have led some authors to propose differing algorithms to infer the original model geometry from the discrete point data provided post slicing. Wade and Borish [46] proposed a hybrid curve fitting approach which uses change in curvature to add both arc and spline motion commands to a sliced part which was able to reduce motion commands in machine script and reduce faceted surface while maintaining path continuity and being computationally efficient but falls short when files with large error or noise are introduced. Valdivieso [75] proposed a method of using a greedy algorithm to find boundaries between arcs which the author selected to call knots then fitting arcs between knots to maintain collinearity within some error bound. This process however does not guarantee that the result will fit withing the original

polyline and too small of an allowed collinearity error can create large amounts of interpolated circular arcs and increase computation time. Other authors have suggested skipping the meshing step entirely and slicing directly from solids. Huang et al. [48] proposed using binary image cross sections to generate contour maps. While this method is faithful to the original topology, it has yet to be adopted into current software.

Similar fitting procedures have been proposed for computer aided design and computer aided manufacturing (CAD/CAM) of computer numerical control (CNC) milled components. Yeung et al. [51] proposed a general framework for fitting arc splines to g-code toolpath motions. Other studies have focused on specific geometries such as precision cams [52], [53], as well as non-uniform scroll components [54]. Arc fitting has also been developed and implemented for uses such as digital graphical interpretation [55], [56]; and for shape recognition, noise filtering, or vectorization [57]; these methods, however, differ greatly in source data, desired output, and intended usage making it difficult to utilize their work for AM path planning.

The method proposed in this work takes input of the ordered points output by slicing and sections the data into three geometric primitives which are either an arc, a line, or a corner. Corners are included in this case as in some AM processes like additive friction stir deposition, and directed energy deposition processes such as wire arc additive manufacturing small parameter changes are necessary in tight corners as they impact material properties and print success though are not a necessary classification for all AM processes nor would be included in the eventual machine script. Arc fitting is then accomplished first through a least squares approach which utilizes least squares circle fitting equations shown by Umbach and Jones [50], and Forbes [49], which are detailed in the following section. This initial fit is followed by a refinement step to conserve path continuity. This arc fitting process avoids many ambiguities that are symptomatic of path planning for AM process geometries following the described design criteria. Any method developed for use in path planning for additive manufacturing must:

- Produce a unique result for any reasonable input. (Stable)
- Handle error in source data while producing reasonable results. (Robust)
- Have meaningful, and intuitive adjustment parameters. (Intuitive)
- Be able to maintain path continuity, and report path directionality (Aligned)

- At worst, not fit an arc to a series of points i.e., with proper settings must fail to fit an arc to unintended points. (Selective)
- Avoid minimum point fits. (Holistic)

In fulfilling these requirements, no single method currently exists. In this work, two methods are applied to achieve the preceding criteria. Method one provides an initial guess of the radius and center point while being stable, robust, and intuitive. The second method moves and reorients the arc by moving the center point of the arc defined in the initial guess such that the first and last point fall into the defined arc. This guarantees path continuity.

Methods:

Mathematical background of arc fitting

A circle in cartesian coordinates is described mathematically using Equation 13 where R is the circle's radius, (x, y) describe cartesian coordinates, (a, b) describe the center of the circle.

$$R^2 = (x - a)^2 + (y - b)^2 \tag{13}$$

The minimum information required to fully describe any arc (or circle segment) is three ordered points since three distinct and non-colinear points fully describe both a circle and a triangle where the circle is called the circumcircle. This is shown in **Figure 39** where (θ) is the angle between the center coordinate and the exterior coordinates and (i) is the relative point iterator position. Point order required for the arc description as the direction (clockwise (CW) or counterclockwise (CCW)) is ambiguous without it. Another way to find the radius of an arc drawn by three point is using Equation 14, where R is equal to the multiplied value of the side lengths of the inscribed triangle divided by four times that triangle area (A) [76]. If using this method, Equation 1 is used to calculate for (a, b).

$$R = \frac{\sqrt{[(x_i - x_{i-1})^2 + (y_i - y_{i-1})^2][(x_{i+1} - x_i)^2 + (y_{i+1} - y_i)^2][(x_{i-1} - x_{i+1})^2 + (y_{i-1} - y_{i+1})^2]}}{4A} \tag{14}$$

The area can be defined using a simplified Gauss's area formula (Equation 15). The area found by this formula will be positive if the points are arranged CCW about the center and negative if arranged CW; this attribute is used to determine arc direction for use in g-code creation.

$$A = \frac{1}{2}[(x_i - x_{i-1})(y_{i+1} - y_i) - (x_{i+1} - x_i)(y_i - y_{i-1})] \tag{15}$$

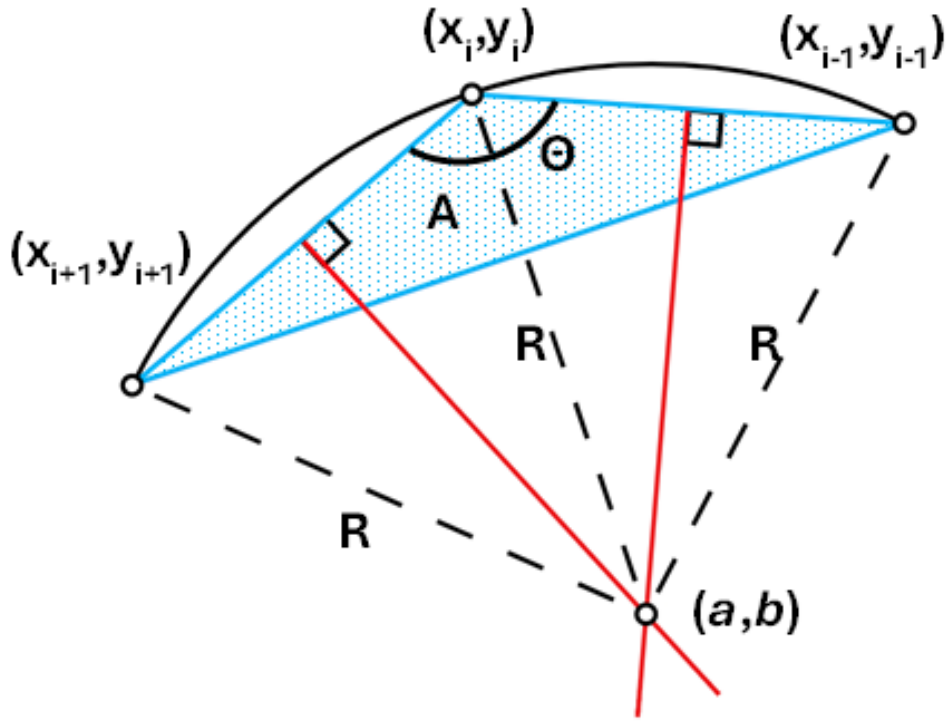


Figure 39: Example of 3 points forming both a triangle and a circle segment. Used and altered with permission from [46].

Since three ordered points can perfectly describe an arc, it is known the end points of the arc will end on the provided data points which guarantees collinearity and using Equation 3 the relative direction of the arc can also be determined.

Circles can also be fit to data using a least squares approximation of a given dataset. The method in this paper is called modified least squares (MLS) and is error tolerant while being computationally efficient and producing reasonable results (i.e. path resembles original geometry). This method has an input of $n \geq 3$ unique points and produces a unique radius and center point if all n points are not colinear. The closed form solution is shown in Equations 16-22, where a (Equation 16) is the center point coordinate in X, and b (Equation 17) is the center point in Y, and where x_i and y_i are the coordinates for a data point in 2D space. The variables B, C, D, E, and F are auxiliary or helper variable.

$$a = \frac{ED - CF}{BD - C^2} \qquad (16), \qquad b = \frac{BF - CE}{BD - C^2} \qquad (17)$$

$$B = n\sum_{i=1}^{n} x_i^2 - \left(\sum_{i=1}^{n} x_i\right)^2 \qquad (18)$$

$$C = n\sum_{i=1}^{n} x_i\, y_i - \left(\sum_{i=1}^{n} x_i\right)\left(\sum_{i=1}^{n} y_i\right) \qquad (19)$$

$$D = n\sum_{i=1}^{n} y_i^2 - \left(\sum_{i=1}^{n} y_i\right)^2 \qquad (20)$$

$$E = \frac{1}{2}\left\{n\sum_{i=1}^{n} x_i y_i^2 - \left(\sum_{i=1}^{n} x_i\right)\left(\sum_{i=1}^{n} y_i^2\right) + n\sum_{i=1}^{n} x_i^3 - \left(\sum_{i=1}^{n} x_i\right)\left(\sum_{i=1}^{n} x_i^2\right)\right\} \qquad (21)$$

$$F = \frac{1}{2}\left\{n\sum_{i=1}^{n} y_i x_i^2 - \left(\sum_{i=1}^{n} y_i\right)\left(\sum_{i=1}^{n} x_i^2\right) + n\sum_{i=1}^{n} y_i^3 - \left(\sum_{i=1}^{n} y_i\right)\left(\sum_{i=1}^{n} y_i^2\right)\right\} \qquad (22)$$

Once a center point is created, the radius r is the average distance from the center to this point as shown in Equation 23.

$$R = \sum_{i=1}^{n} \sqrt{(x_i - a)^2 + (y_i - b)^2}/n \qquad (23)$$

This fitting error is calculated in Equation 24 by summing the squares of the difference between the radius and the distance to the center point for each data point.

$$Error_{fit} = \sum_{i=1}^{n} \left(R - \sqrt{(x_i - a)^2 + (y_i - b)^2} \right)^2 \quad (24)$$

Both fitting methods are utilized to produce the algorithm described in the following section to fulfill the author's design requirements. For illustrative purposes, the process is classified into three steps: point primitive determination, arc initial fit, and arc reorientation. During point primitive determination, for each point in the input array of ordered coordinates following a logic path, each point is determined to be either a line, a corner, or an arc. In this step, proper parameters are assigned to avoid minimum point fits (holistic) and fit arcs only to intended points (selective). For each point, if it is determined to be part of an arc it will enter the following steps. During arc initial fit, the least squares approach is utilized to produce a result that is stable, robust, and intuitive (produces a unique result for any reasonable input, handles error in source data, and has meaningful and intuitive adjustment parameters). Finally, during arc reorientation, the arc center point is repositioned while maintaining the fit radius using the 3-point fit method ensuring continuity while also determining path arc direction relative to center point (aligned).

Point primitive determination

To identify local primitives at each coordinate point in the ordered list, a series of tests are carried out. The input is an array of ordered coordinate points $n \geq 3$ as the points are analyzed in groups of three points starting with $i = 2$. A description of this process is also described in the following pseudocode.

Begin pseudocode

for $i = 2{:}\,n$ *(where* n *is the length of the ordered point array)*

calculate distance between $i - 1$ *to* i *(*L_1*),* i *to* $i + 1$ *(*L_2*), and* $i - 1$ *to* $i + 1$ *(*L_3*)*

find included angle between 3 points (θ*)*

if $(\theta > \theta_{max})$ *or (*L_1 *or* $L_2 > L_{max}$*) or (the segment only contains 2 points)*

then the point must be a ***line***

else if $(\theta > \theta_{min})$ *or* $(\theta == NaN)$

then the point must be a ***corner***

else (conduct 3 into 4 point arc test)

create an initial arc fit using least squares method (R)

calculate the error ($Error$*) for adding the* $i + 2$ *point (4th point)*

find directional radius for fit including the 4th point (R_4)

calculate distance from $i+1$ to $i+2$ (L_4)

if ($Error > Error_{max}$) or ($L_4 > L_3$) or ($R/|R| \neq R_4/|R_4|$)

*then the point must be a **corner***

else if $R > R_{max}$ (arc is of sufficient size that can be assumed safely to be a line)

*then the point must be a **line***

else

*the point must be an **arc***

while ($i \leq n-2$) and ($Error < Error_{max}$)

*the point must be an **arc***

end pseudocode

The code is also described visually in **Figure 40**. For every arc composed of the sequenced points, an initial fit is constructed and then is reoriented to maintain path continuity. The 3 into 4 point arc test is designed to compare how the addition of a 4th point alters the single solution of the 3 point initial point as only a single circle can be fit to 3 non-colinear points. 4 factors are measured in this test, first the change in fit radius, second the error for including the next point from the initial fit, third the error of the 4 point fit, and lastly the relative distance of the 4th point relative to the initial fit point density. If the 4th point implies a different direction of rotation (change in radius sign), or is vastly different than the 3 point fit then the fit must be rejected. If error for adding the point is too high then the fit must be rejected. If the point density varies too much then the fit must also be rejected. This makes this method effectively require a minimum of 4 points for a successful arc fit. This eliminates the edge cases of closely grouped shallow corners and limits the impact of close error points.

Initial arc (least squares)

The initial arc fit is based on a modified least squares method (Equations 4-12) which minimizes error from each point to a center point. This method has an input of $n \geq 3$ points and produces a unique radius and center point if all n points are not colinear. As more points are added, the stability of the fit is improved as each subsequent point is less likely to change the fit. For each new coordinate to be added, a process similar to the 3 into 4-point test are completed as follows. First, the following values are calculated:

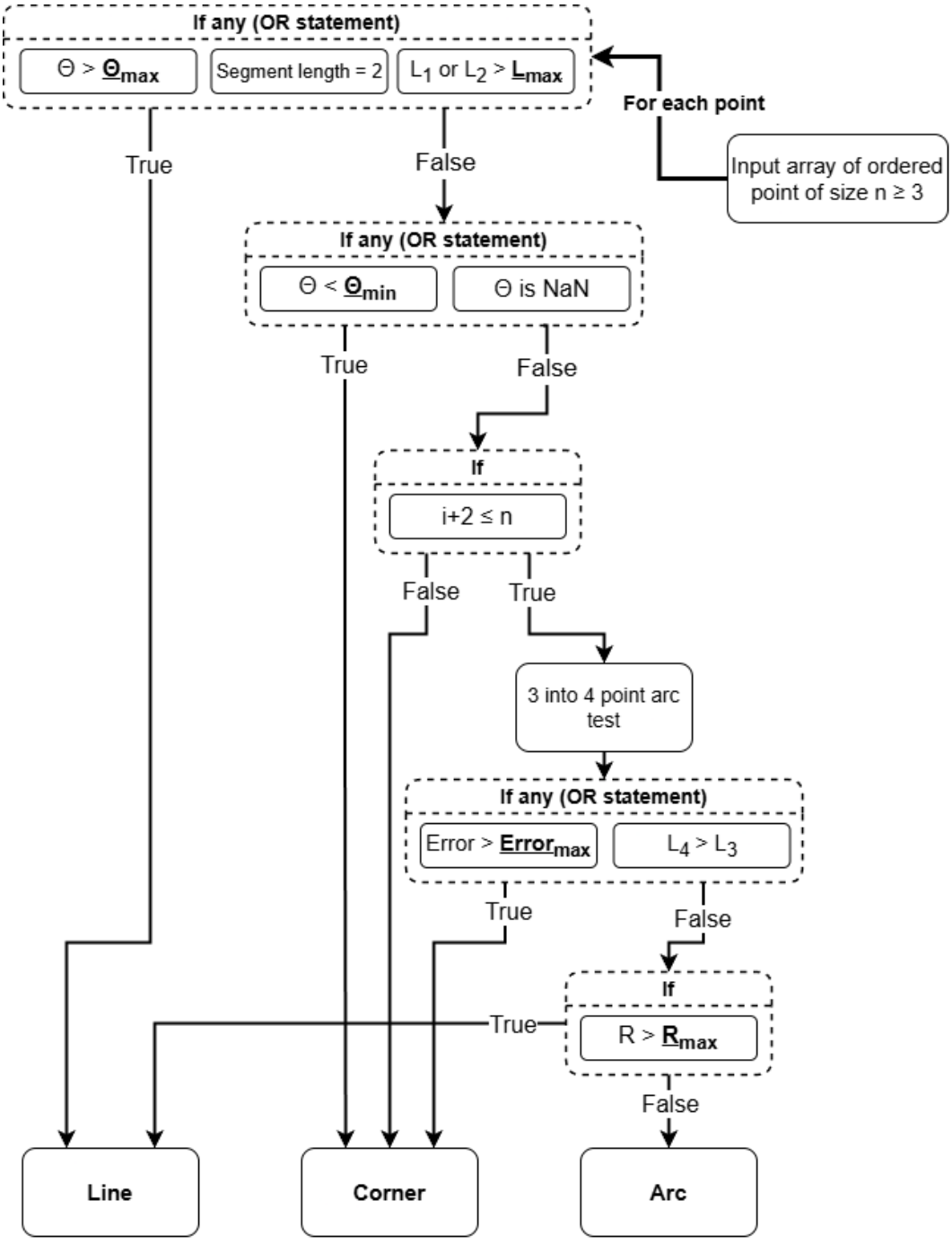


Figure 40: Flowchart of decision logic for primitive determination. Intended adjustable parameters are bolded and underlined.

- Error between the current fit and the next candidate point ($Error$) is calculated by subtracting from the current fit radius (R) the distance between the candidate point and the fit center and taking the absolute value (Equation 13).

$$Error = \left| R - \sqrt{(x_{i+1} - a)^2 - (y_{i+1} - b)^2} \right| \tag{25}$$

- The distance between the current final fit point and the next point (L). For point density comparison with L_{max}.
- The distance between the current first fit point and the next point (d_{Last}). If the first and last point are coincident then the arc direction cannot be calculated meaning the reorientation step cannot occur. This value can be compared to some value near 0.
- Lastly, a new fit is calculated including all prior fit points and the next candidate point ($R_{i+1}, a_{i+1}, b_{i+1}, Error_{fit_{i+1}}$).

If $Error < Error_{max}$, $Error_{fit_{i+1}} < Error_{max}$, $d_{Last} > 0$, $L < L_{max}$, $R_{i+1}/|R_{i+1}| = R/|R|$, and the candidate coordinate is not the last point of a print segment then the candidate is included in the arc fit. If any of these conditions are false, then the included segments are stored in the current fit are stored and each coordinate in the arc are given the same identifier and the radius and center point along with the included points are stored. Once all candidate points have been identified, the selected points enter the reorientation step which is necessary to guarantee path continuity as with noncircular curves the error minimization step does not mean that the arc will begin or stop on a known coordinates as shown in **Figure 41**.

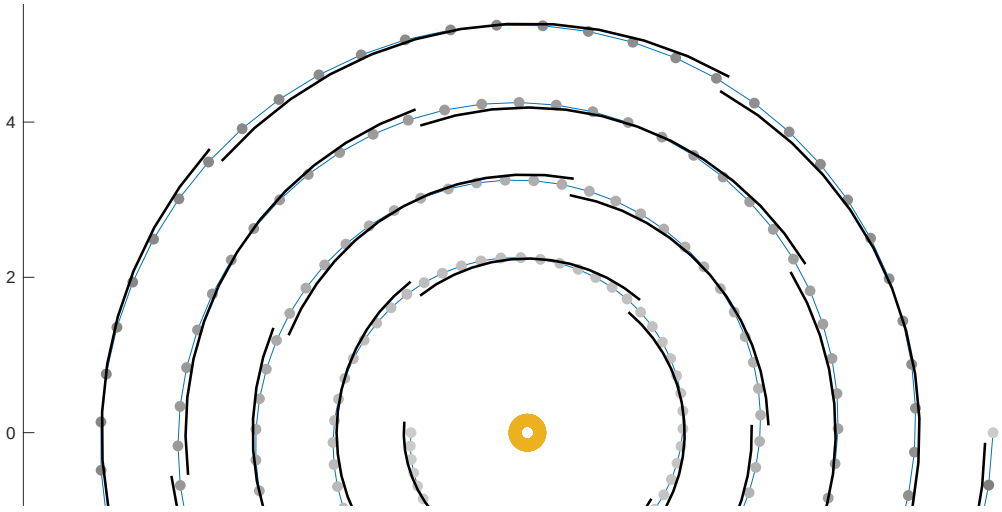


Figure 41: Example of fit arc segments not landing on first and last coordinates on a noncircular arc with rounded data points.

Arc center point reorientation

Two methods for arc reorientation are proposed. The first method uses Equation (14) and solves a new point that matches the fit radius but must fall on the first and last points by definition. The created point is termed the phantom point and in the defined variables is point (x_2, y_2) where the first point is (x_1, y_1) and the last point is (x_3, y_3). Since Equation 14 is noninvertible in x_2 and y_2, the phantom point must be solved for iteratively and the initial guess phantom coordinate can be any value contained in the arc aside from the first and last. Once the phantom point is generated, the center point is solved for once again using the modified least squares method (Equations 16 and 17).

The second method is based off Equation 13. Given a radius and two coordinate points, there are two distinct center points that could be solved (shown in **Figure 42**) for (except in the case of a half circle in which case there is only one solution). Since Equation 13 is noninvertible for a and b, this equation must also be solved for iteratively. The initial guess for the center point is the initial fit center point. This solution is more stable in most cases than the first method and the calculation and verification of the function derivative is simpler. For both cases, the Newton-Raphson root finding method is effective. At a high level, the Newton-Raphson root finding method for finding roots of a real-valued function by using its first derivative to successively refine guesses for where the function equals zero. In this case, it is effective as you only need on value as an initial guess.

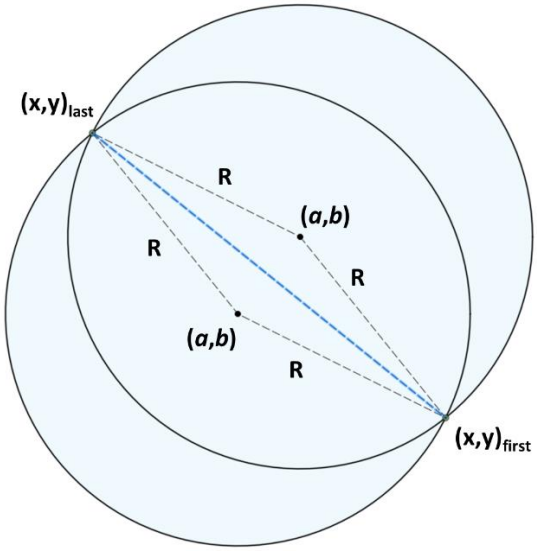


Figure 42: Example of multiple center point solutions for the same radii.

Results and discussion:

In this section several geometries are tested, and their fits are evaluated. Each geometry is sized in the range for large scale processes such as big area additive manufacturing (BAAM), wire-arc additive manufacturing (WAAM), or additive friction stir deposition (AFSD), though, mathematically, the fitting process is not sensitive to scale. For smaller processes, the tuning parameters must be changed. Unless otherwise specified, the fitting parameters shown in **Table 6** were used for all tests. Where the maximum fitting error allowed to enter the arc loop was one fifth that of $Error_{max}$, and Δab_{max} is the maximum difference between the average of the center point coordinates between root finding method (Newton-Raphson in this case) iterations for the reorientation method. All meshes were input as .STL filetype into ORNL Slicer 2 [77] for cross sectioning and point extraction. Test geometries include circular and non-circular arcs, straight and corner components, as well as meshes containing error points.

Geometry 1: Fish Shaped Test Part

The Fish shaped test part is a simple geometry intended to allow for easy error analysis on a smaller number of well-defined curves with some sections that can be challenging for fitting methods. Meshes were exported as STLs with three different error tolerances shown in **Table 7** where surface deviation is the maximum deviation between the original part and the mesh surface and normal deviation is the maximum difference between face normal vectors on a curve. Other settings for STL generation of maximum edge length (300.9 *mm*), which is the maximum length of the longest side of any triangular facet, and aspect ratio (21.5), which is the maximum ratio of the longest side of each triangle to the shortest, are overruled in this case. The low-resolution table of coordinate points is provided in the appendix. The fit results are shown in **Figure 43** where the color of the dots matches the key for each element unique identifier, the arcs are numbered sequentially positive, and the lines numbered sequentially negative. The black line plotted on top is the total fit geometry. Plotted below is a blue line that is the linear only fit though this line cannot be seen from the default view. In **Table 8**, the fits are compared with the known values.

Table 6: Nominal fitting parameters.

Fitting parameters					
$\mathbf{R_{max}}$=7600 *mm*	$\mathbf{L_{max}}$=50 *mm*	$\boldsymbol{\theta_{max}}$=179.9°	$\boldsymbol{\theta_{min}}$=95°	$\mathbf{Error_{max}}$=1.27 μm	$\boldsymbol{\Delta ab_{max}}$=$10^{-9}$ *mm*

Table 7: STL tessellation parameters.

Tessellation Parameters		
STL Resolution	**Surface Deviation**	**Normal Deviation**
Low	0.11980 *mm*	30.0°
Medium	0.04769 *mm*	15.0°
High	0.01508 *mm*	10.0°

Table 8: Fish shaped test part fit errors.

Fish Shaped Test Part Model Dimensions							
Actual	**Radius** (*mm*)	**Error** (*μm*)	**Fit error** (*μm*)	**a** (*mm*)	**Error** (*μm*)	**b** (*mm*)	**Error** (*μm*)
Arc 1	50.800	-	-	203.200	-	50.800	-
Arc 2	88.900	-	-	185.398	-	70.458	-
Arc 3	-44.450	-	-	73.025	-	142.252	-
Fit dimensions							
Low	**Radius** (*mm*)	**Error** (*μm*)	**Fit error** (*μm*)	**a** (*mm*)	**Error** (*μm*)	**b** (*mm*)	**Error** (*μm*)
Arc 1	50.8015	1.4731	0.0005	203.1985	-1.473	50.8015	1.4728
Arc 2	88.8997	-0.2885	0.0018	185.398	-0.0398	70.4587	0.6978
Arc 3	-44.4477	2.2801	0.0001	73.0259	0.8739	142.2504	-1.5803
Medium	**Radius** (*mm*)	**Error** (*μm*)	**Fit error** (*μm*)	**a** (*mm*)	**Error** (*μm*)	**b** (*mm*)	**Error** (*μm*)
Arc 1	50.8053	5.327	0.006	203.1947	-5.327	50.8053	5.327
Arc 2	88.8981	-1.9381	0.0032	185.3991	1.0625	70.4625	4.4942
Arc 3	-44.4562	-6.2428	0.0002	73.0218	-3.1588	142.2589	6.9415
High	**Radius** (*mm*)	**Error** (*μm*)	**Fit error** (*μm*)	**a** (*mm*)	**Error** (*μm*)	**b** (*mm*)	**Error** (*μm*)
Arc 1	50.7990	-1.0445	0.1533	203.201	1.0453	50.7990	-1.0459
Arc 2	88.9195	19.4843	11.5463	185.347	-50.9937	70.4895	31.4599
Arc 3	-44.4348	15.2164	0.0943	73.0116	-13.3537	142.2349	-17.0626

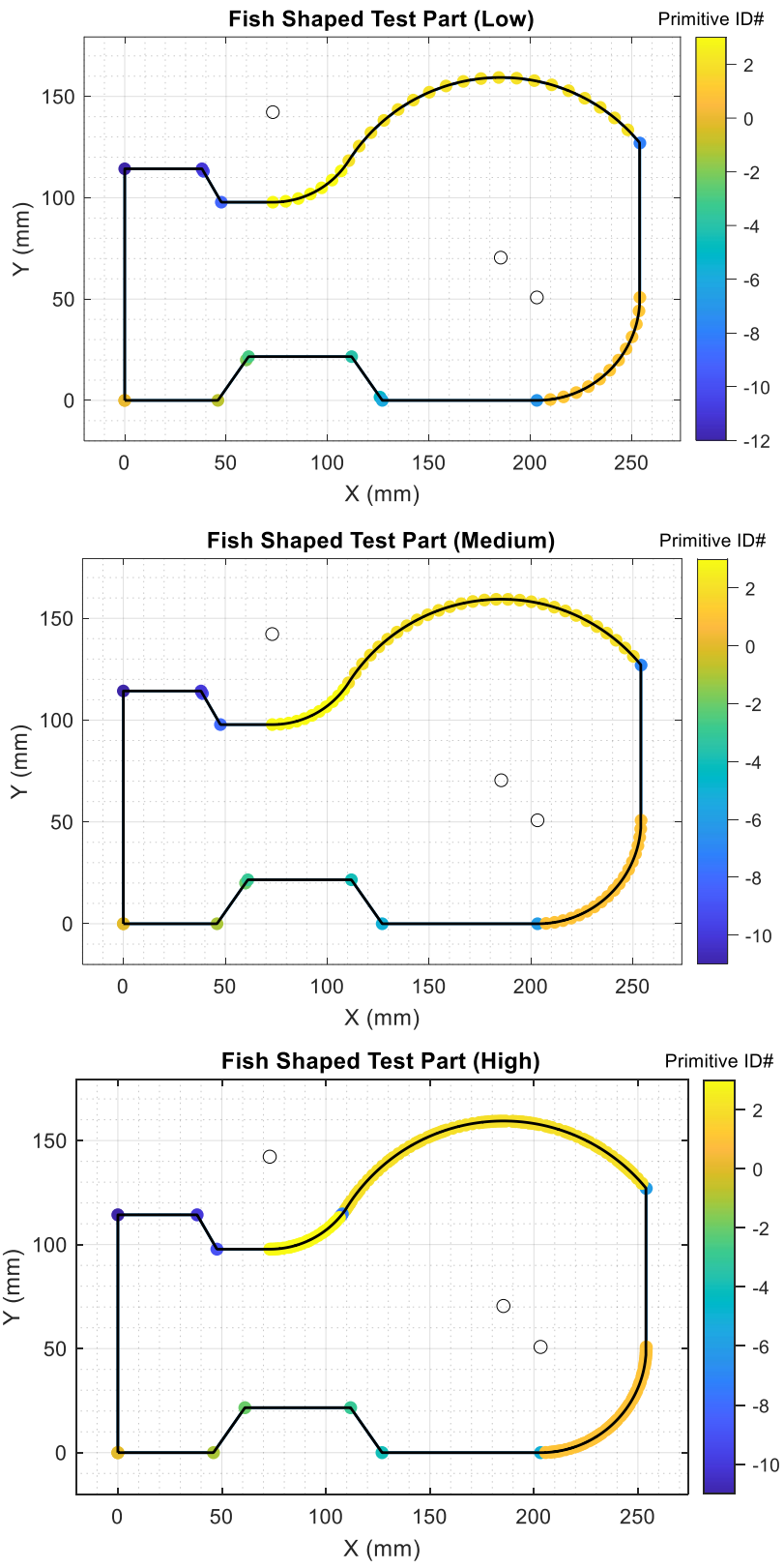


Figure 43: Fish shaped test part fit plots.

From the calculated and fit errors for this geometry, the best case was the low-resolution part. This is likely because the algorithm is less likely to go one or more point too far when fitting consecutive arcs. This issue can be solved using a smoothing algorithm. For all cases, the first arc fit is the best with the lowest error being on the high-resolution case. The highest radius error is in the high-resolution case at a value of 19.5 μm representing an error of 0.02% on the radius. For the low-resolution case, the same arc error is 0.29 μm representing an error of 0.0003% on the radius. However, the error is spread of more points and the impact of error between more closely spaced points is less. With similar results irrespective of resolution, however, it is more advantageous to use the fewest points possible as the decrease in point density with properly fit arcs does not impact the final part surface quality. Further parameter tuning could optimize the results though the purpose is to demonstrate a more robust solution without parameter tuning. Similar testing with more complex geometries should be conducted to further discover the impact of mesh resolution on fit quality.

Geometry 2: Archimedes spiral

The second geometry that is evaluated is an Archimedes spiral to test the fit method's ability to fit to a broad range of continuous curvature. Points were generated for 7 and 180 loops starting from an angle of 180° at two-point densities (30 and 60 points per loop). Each subsequent loop increases the radius from the center by 25.4 mm such that the maximum radius is 4584.7 mm for 180 loop cases and 190.5mm for the 7 loop cases. Each of the 4 cases were evaluated at two fit error maximums ($Error_{max} = 12.7\mu m$, and $Error_{max} = 1.27\mu m$). For these tests, the max allowed point distance before a line was fit had to be increased $L_{max} = 500\ mm$. Results for these tests are tabulated in **Table 9** and plots representing the fits for the higher error tolerance 7 loops tests are shown in **Figure 44**.

All cases exhibited relatively low error, and under the lower error tolerance, the size of the input array did not change the number of arcs, only the number of points per arc. Doubling points increased the fit error in this case because adding points can only increase error as it is the total deviation of all points. The maximum fit error for all cases was 1.3 μm. This method successfully fit arcs continuously to the spiral without forcing fits to the minimum number of points frequently.

Table 9: Archimedes spiral test results

Archimedes Spiral Test				
30 Points per loop	**Initial fit error limit = 12.7** μm		**Initial fit error limit = 1.27** μm	
	5400 points	**210 points**	**5400 points**	**210 points**
Mean fit error (μm)	10.3	9.9	0.536	0.527
Number of arcs	600	24	900	35
Points per arc	9	9	6	6
Calculation time (*ms*)	213.66	10.9	220.97	12.78
60 Points per loop	**Initial fit error limit = 12.7** μm		**Initial fit error limit = 1.27** μm	
	10800 points	**420 points**	**10800 points**	**420 points**
Mean fit error (μm)	13.6	13.2	1.1	1.1
Number of arcs	636	25	900	35
Points per arc	17	17	12	12
Calculation time (*ms*)	356.18	16.21	361.90	16.42

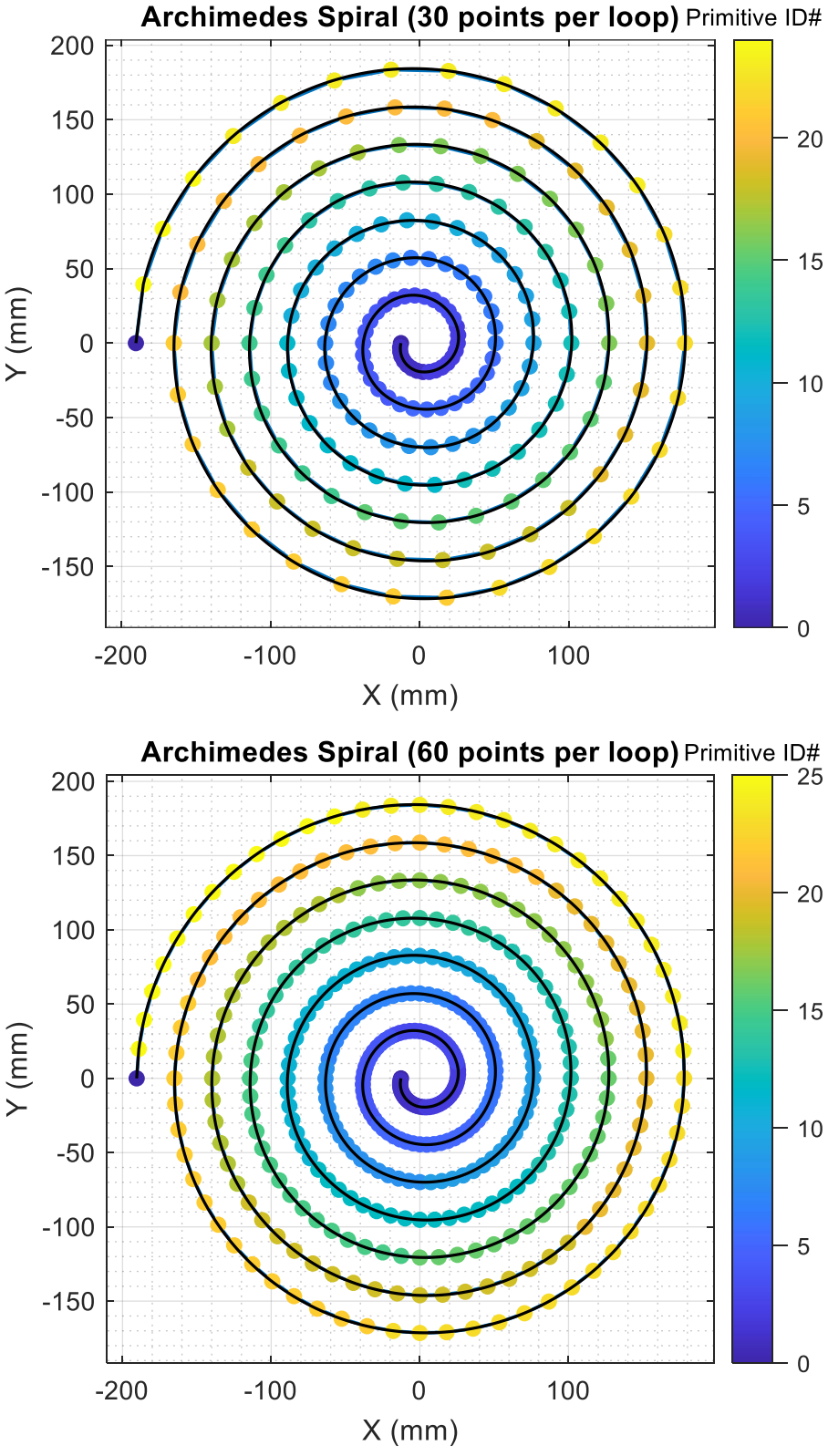


Figure 44: Plotted Archimedes spiral results.

Geometry 3: Spline sprocket

The third geometry is a sprocket as it contains repeated curves and tip flats and are constructed using non-circular curves. This will demonstrate the impact of directionality with this method. This geometry was also selected as a nonideal geometry for the nominal fitting parameters used in the other tests. The fit result using the nominal parameters is shown in **Figure 45**. Each tooth and subsequent gap are fit with four arcs and three-line segments. The arc fit errors for each tooth shown in the order as in **Figure 45:** Section A are [0.8944, 0.00001, 0.00001, 0.2348] µm. In the same order, the arcs each contain these number of points [9 4 4 5]. Because this method uses ordered points, directionality is relevant as the least squares method becomes more stable the more points in the fit. In this geometry, a straight-line segment is missed between the third and fourth arcs. This could be solved by decreasing the maximum length parameter. This fit also has relatively low error.

Geometry 4: Abstract spline

The fourth geometry is constructed using many b-splines. Using the nominal parameters 22 arcs and 83 lines out of 342 points were fit at an average fit error of 0.798 µm and a maximum arc fit error of 1.6 µm. The longer sections of linear moves are due to the initial fit radius being larger than the maximum allowed or the sign of the radius changing during 3 into 4-point arc fit test. In one case, there was an error point which had 2 neighboring points offset by 158 µm. The plotted result of the fit is shown in **Figure 46**.

Geometry 5: Challenge STLs

The fifth and final set of geometries used to evaluate this arc fitting method are three provided challenge STLs which are discussed separately. The first STL is an ideal geometry containing 17 half circles, 8 semi circles and 2 splines. The algorithm fit 29 total arcs and 39 line segments from the 241 points at an average fit error of 0.996 µm and a maximum error of 14.4 µm found on the 14^{th} arc due to an error point. The plotted results are found in **Figure 47**.

The second STL is a hollow geometry with one side being composed of splines. The algorithm fit 14 arcs and 75 line segments to the 272 points with an average fit error of 0.655 µm and a maximum of 2.3 µm. This part would be helped by a smoothing algorithm as sections which likely by design could have had arcs do not because of large error. The plotted results are found in **Figure 48**.

The third STL is a pillar like object with mounting holes. The algorithm fit 6 arcs

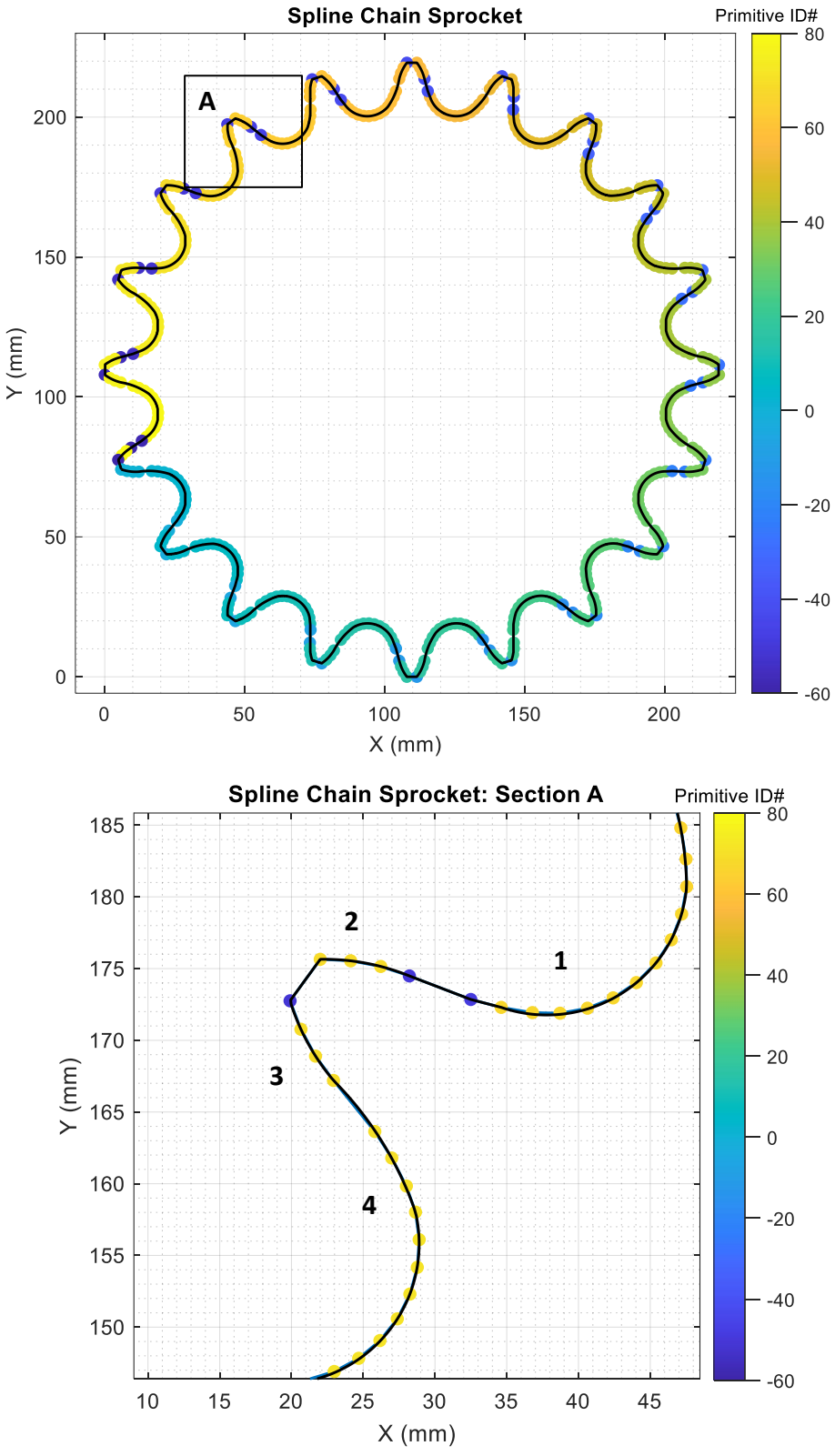


Figure 45: Plotted result of arc fit to spline chain sprocket.

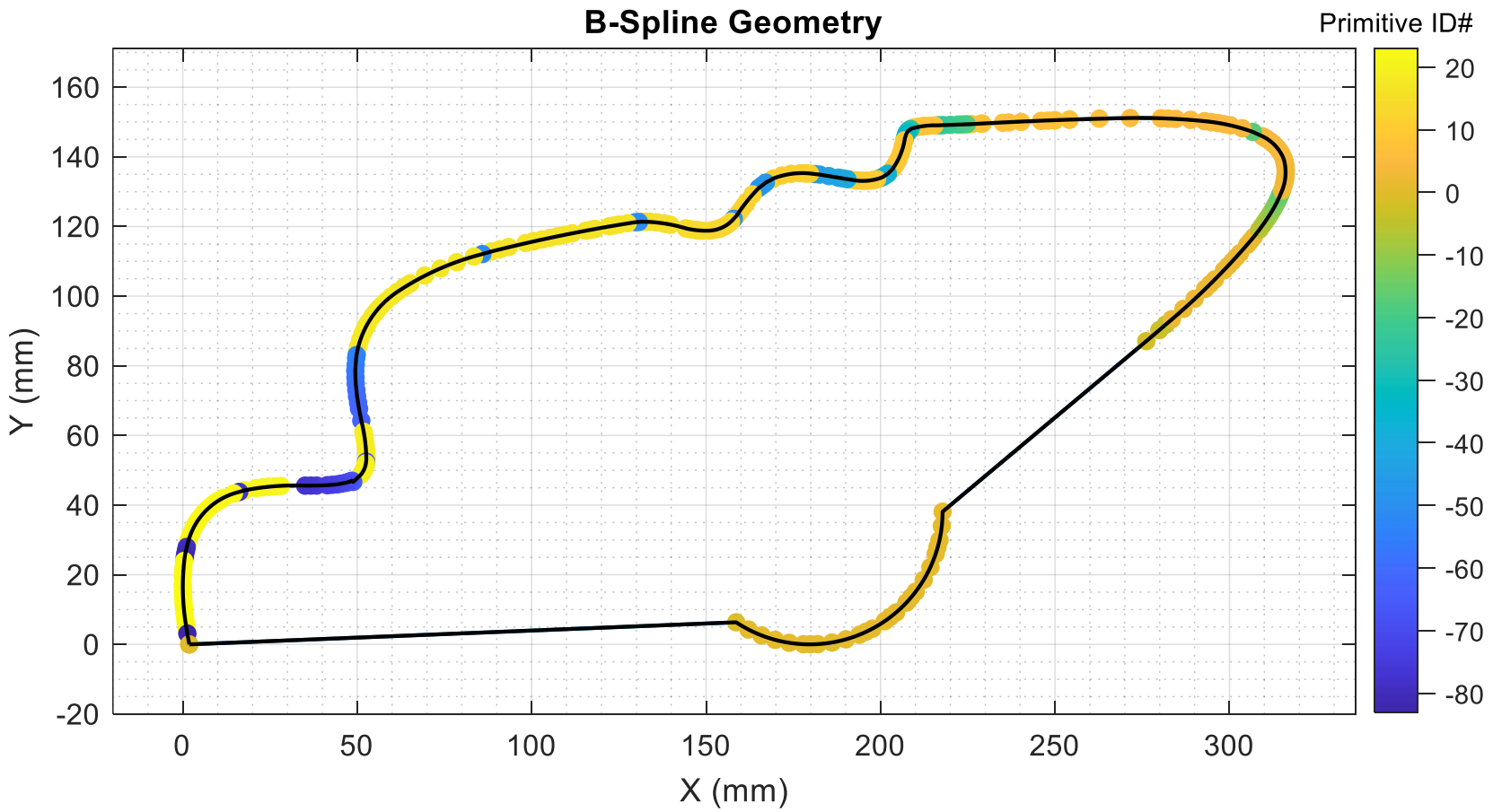


Figure 46: Plotted fit to an abstract b-spline curve geometry.

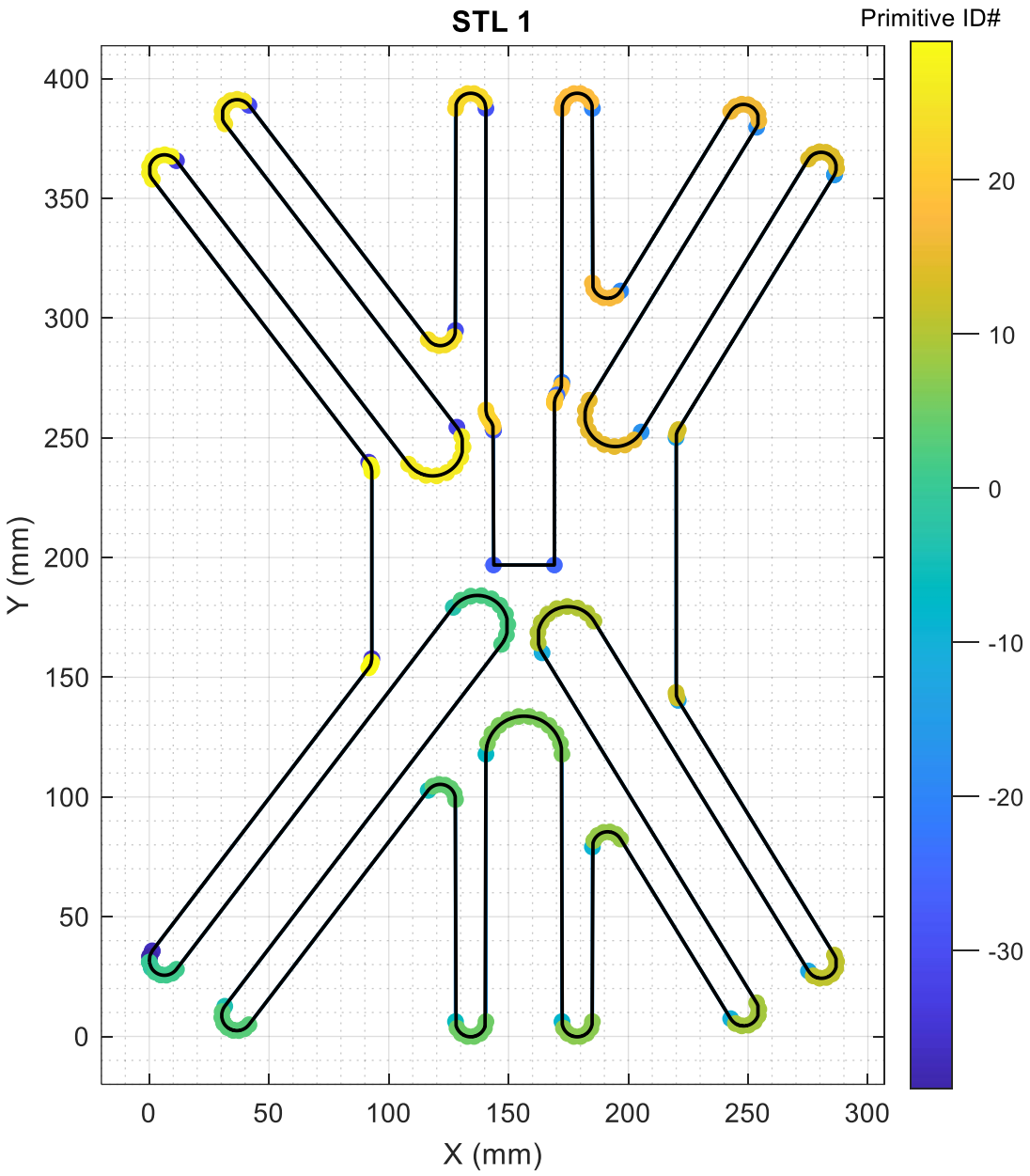


Figure 47: Challenge STL 1 plotted fit.

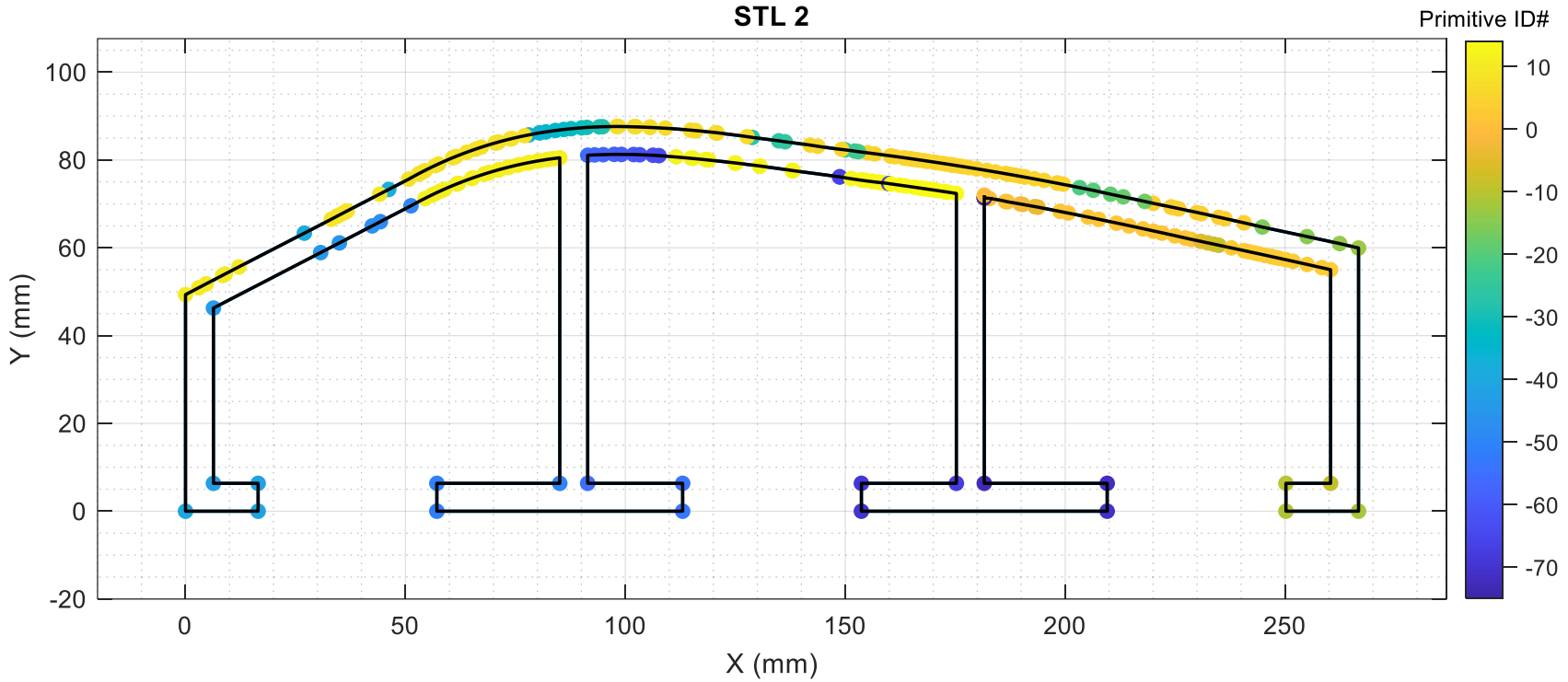


Figure 48: Challenge STL 2 plotted fit.

and 21 line segments to the 319 points with an average fit error of 1.37 µm and a maximum of 8.1 µm due to a duplicate point near the final point of the second arc that the reorientation algorithm is forcing to drive the fit. A slight reduction in maximum error would reject this point bringing the average fit error of 0.04 µm and a maximum of 0.07 µm. The plotted results are found in **Figure 49**.

Summary

To summarize the presented testing and results, many variations and types of geometries of similar scale were used to evaluate the effectiveness of the proposed geometric primitive fitting method. Despite no parameter optimization, sufficient fits were found for all geometries. The algorithm could benefit from some automated parameter optimization schemes or parameter adjustment due to specific geometric elements to improve fits. Based on the results from the first and second geometry sets, this method works best with larger relative point spacings at higher resolutions. Limiting the fitting resolution did not always keep the final error below the desired tolerance, since the reorientation step can increase error in non-circular curves. However, the average error often remained below the threshold, with error points being a common error contributor.

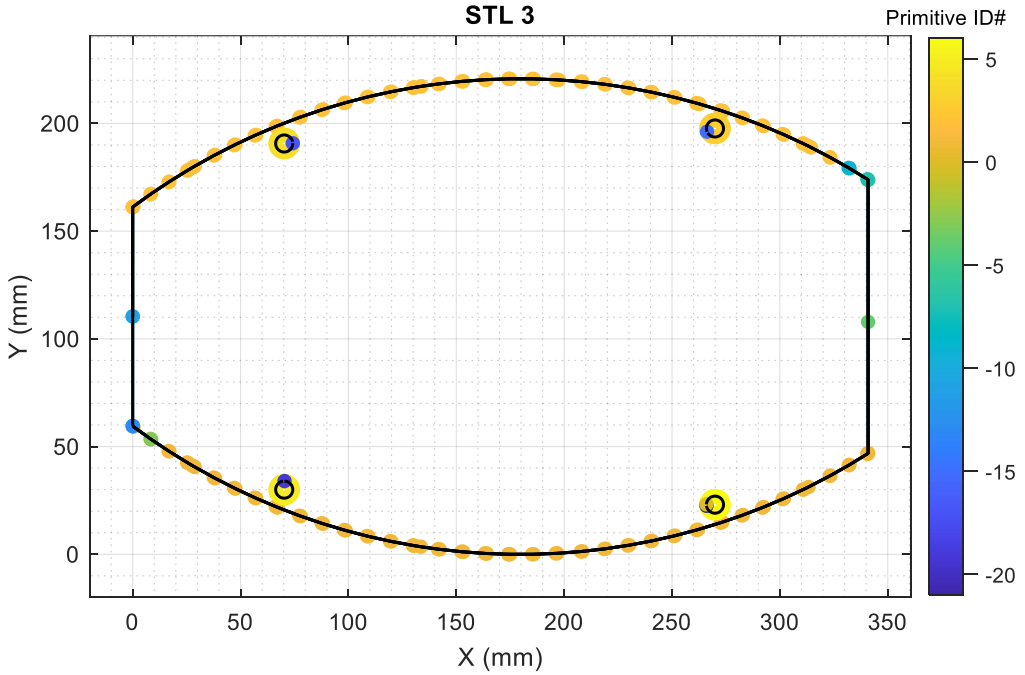


Figure 49: Challenge STL 3 plotted fit.

Conclusions:

An arc fitting method for use in additive manufacturing path planning that takes input of the ordered points output by slicing and sections the data into three geometric primitives which are either an arc, a line, or a corner. The method is described and then tested on various geometries. The arc fitting is accomplished through a least squares approach, which is followed by a refinement step to conserve path continuity with the following design goals:

- Produce a unique result for any reasonable input. (Stable)
- Handle error in source data while producing reasonable results. (Robust)
- Have meaningful, and intuitive adjustment parameters. (Intuitive)
- Be able to maintain path continuity, and report path directionality (Aligned)
- At worst, not fit an arc to a series of points i.e., with proper settings must fail to fit an arc to unintended points. (Selective)
- Avoid minimum point fits. (Holistic)

Despite not optimizing fit parameters to each geometry, an effective fit was found for each which vastly reduced the total number of required motion commands and better described the original geometry.

Future work

To further improve this method, an algorithm should be developed to auto select the L_{max} parameter. Other improvements could be algorithms to assist in the elimination of error points such as post filtering using curvature information after the initial fit for refinement or the inclusion of an L_{min} parameter to remove small disruptive variation early in curve development. More investigation should be done on prefiltering of the ordered point data as this could also improve results.

CHAPTER 5: AUTOMATED AFSD OVERLAP COMPENSATION ALGORITHM FOR AM PATH PLANNING

Introduction

This chapter describes an algorithm which utilizes the overlap methods defined in chapter 3 with the geometric fitting from chapter 4 to create to apply these changes automatically for usage in path planning in AFSD. Following the description will be a couple of example geometries which utilize this algorithm. The part which started foray into path planning in AFSD is shown in **Figure 50**. The component geometry is a cone, and while attempting to deposit this 3D geometry, challenges associated with balancing what can be reasonably coded by hand while pursuing optimal printing paths became apparent. The g-code script used for the bottom half was a parameterized script which decreased the radius of a circular path as the build height increased but was plagued with the creation of squeeze flash on layer transitions. The logical build plan change is to path plan helically. This, however, is difficult to carry out when coding by hand. This print was also completed using a discrete feed system so when and where to reload the feed also became a source of material and time inefficiency. Therefore, a script was developed and utilized which took input of a series of X, Y, and Z cartesian coordinates with paired MFR and TFR. Each coordinate and parameter were coded into a machine script as linear moves, then reloads were planned to improve material and time efficiency. This original script and process are the precursor to the algorithm described in this chapter.

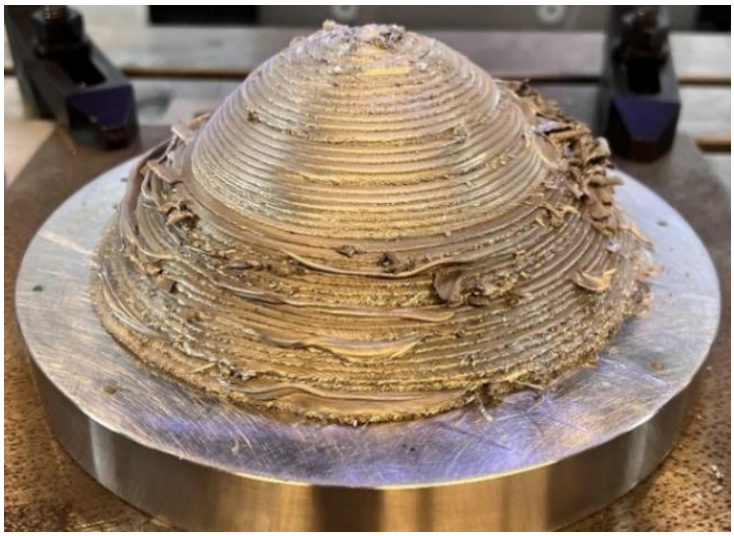


Figure 50: AFSD deposited cone.

Method

This algorithm begins with an array of information that at least minimally defines the AM toolpath in the form of X, Y, and Z cartesian coordinates along with nominal process parameters (MFR and TFR). Local geometry is identified using the process defined in Chapter 4. The presence of overlap conditions is found using a nearest neighbor approach for each classified element in each layer using a point array whose point density has been increased using geometry specific interpolation. With knowledge of geometry and path distance, the appropriate overlap compensation is applied according to the process outlined in Chapter 3. Once the overlap condition is defined, the coordinate matrix is adjusted to compensate for changes in machine Z-axis deflection so that a constant layer height is maintained. New coordinates and corresponding process parameters are produced using this information. A second algorithm is used to code for the specific AFSD machine controller. A flowchart of this process is presented in **Figure 51**.

Method validation: Archimedes spiral

This study was carried out to test and demonstrate the algorithm's ability to fit circular arcs to a curvilinear geometry and effectively compensate the feed parameters. The input point matrix was generated in MATLAB where the radius of the spiral increases by 25.4 mm every full rotation; five layers were deposited in alternating directions using a MELD Manufacturing L3 equipped with a 12.7 mm (0.5 in) square rod discrete feed system. The substrate and feed material were AA6061-T6 rods which were coated in a carbon graphite lubricant. The nominal process parameters were $TFR = 254\ mm/min$ ($10\ ipm$), $MFR = 152.5\ mm/min$ ($6\ ipm$), and $h = 2\ mm$ ($0.080\ in$). MFR was the parameter was adjusted in the overlaps. PID control was used on the build to maintain tool face temperature at $T_{tool} = 420\ °C$. The tool face had four teardrop shaped nubs protruding from the surface to a depth of 2.3 mm (0.090 in). During the deposit there was no evidence of underfeeding, and excess squeeze flash was only generated in the reload locations which occurred due to the discrete feed system requiring a mid-layer reload. The operator only engaged in the process during the reload process. An image of this is shown in **Figure 52**.

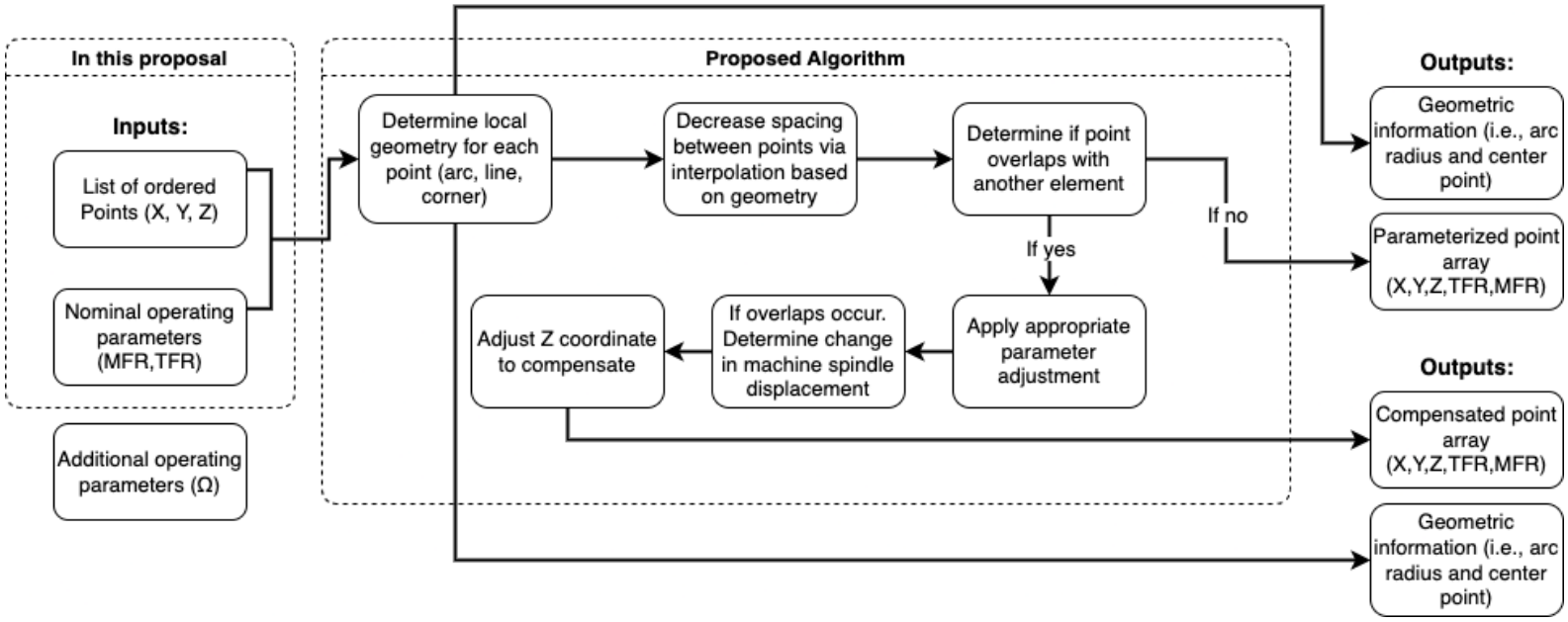


Figure 51: Flowchart of automated overlap compensation algorithm for AFSD.

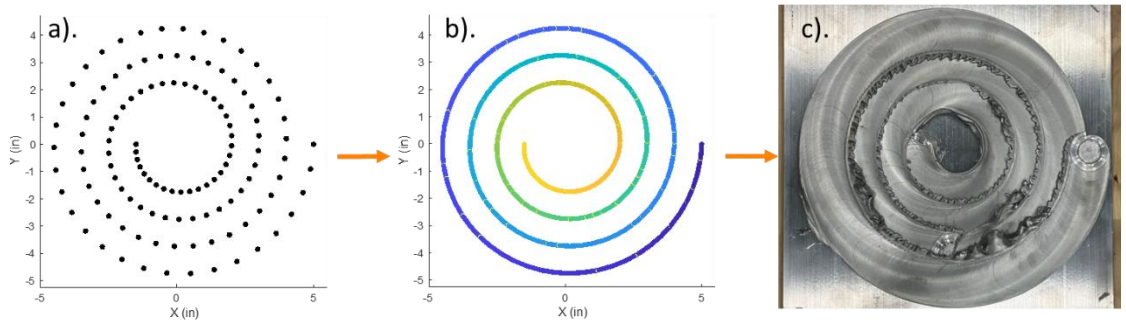


Figure 52: a) Point data describing Archimedes spiral. b). Arcs fit and oriented over toolpath point. c). Deposit from posted code.

Method validation: ogive layup mold

This test was carried out to demonstrate the utility of the algorithm for production of a component using a hybrid manufacturing approach. First, a part model was supplied. Then the model was input into Slicer 2, and a raster path was generated for the entire part. Next, the boundary points from the slicer were input into the algorithm, where process parameters were assigned, and a machine code was output. Note: due to a machine stuttering issue where any change in MFR causes the machine to momentarily pause the sloped parameter changes when moving perpendicular to a build path had to be smoothed as it would cause a severe drop in average TFR. This issue is also why a raster only build path was selected. The build file was then executed on a MELD Manufacturing L3 equipped with a 12.7 mm (0.5 in) square rod discrete feed system. The AA6061-T6 rods were coated in a graphite lubricant. The nominal process parameters were $TFR = 381\ mm/min$ $(15\ ipm)$, $MFR = 228.6\ mm/min$ $(9\ ipm)$, and $h = 2\ mm$ $(0.080\ in)$ MFR was adjusted in the overlaps. PID control was used to maintain tool face temperature at $T_{tool} = 420\ °C$. The tool face had four teardrop shaped nubs protruding from the surface to a depth of 2.3 mm (0.090 in). Following the deposit, a 3D structed light scan of the deposit was taken using a GOM ATOS Q scanner. Using the 3D scan a machining program was made. The hybrid manufacturing process for this part is shown in **Figure 53**.

Three issues are shown in **Figure 54**. The first is a large void found in the top right corner. This issue is related to a machine issue where the control stopped receiving commands causing the steel push rod to create a hole in the build which was unable to be filled during subsequent passes. The second is a small void near the center of the layup surface. This is due to an underestimation of the effect of the corners of the parallel raster paths. The final issue is found in two locations of the bottom left of the mating surface and are related to the algorithm used to smooth the rapid process parameter changes. An under approximation was used in order to prevent corner squeeze flash generation as this would fail the build. However, a slightly aggressive reduction was made such that some exterior regions of the build were underfed on the last three layers.

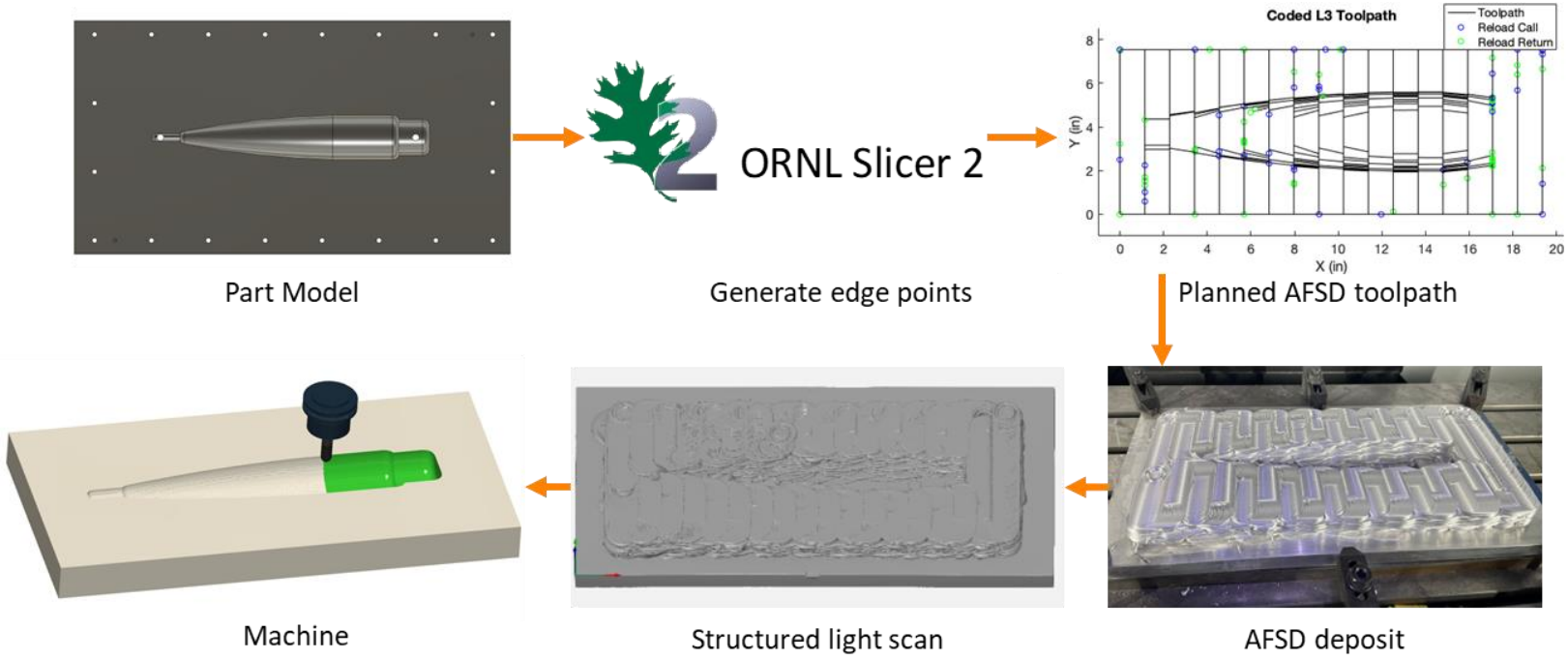


Figure 53: Hybrid manufacturing process flow for the ogive layup mold.



Figure 54: Final ogive mold part.

CHAPTER 6: CONCLUSIONS AND RECOMMENDATIONS

Summary

In AFSD, whenever parallel or neighboring tracks are deposited, they should be allowed to physically interact to ensure that material intermixing occurs. To avoid the creation of defects, namely squeeze flash, process parameters must change (some combination of MFR or TFR). This issue also prevents the traditional framework for slicing and path planning for being utilized to create machine code for part production and therefore many codes are being manually written. This dissertation has outlined a framework which allows for the process parameter changes required for the production of machine code can be automated, including these novel contributions:

- Development of a volume-based approach to calculate the necessary process parameter changes required to prevent squeeze flash generation in overlapping tracks for both linear and curvilinear pathing.
- Development of a robust least squares method for fitting arcs and lines to ordered point data.
- Also, the combination of overlap and point fitting methods into a complete framework for the production of machine code to produce components in AFSD.

These contributions were described in detail and validated through a series of tests intended to simulate real components. This methodology has also already been utilized for the production of large-scale parts outside of the lab environment.

Future work

This dissertation focused on solving issues related to process automation and code generation for AFSD especially in relation to parts containing overlapping track. Additional questions follow which should be explored. First, while the described methods were shown to reduce squeeze flash in overlapping tracks the effect of these process parameter changes material microstructure evolution and resultant material properties is largely unknown and should be researched. Second, another variable for future research consideration is the ratio of process parameter change between MFR and TFR as some combination may be more favorable for different resultant material properties or also for machine kinematic impacts. Most validation studies in this dissertation were limited to

changing only MFR. A third at large question relevant to this dissertation topic is the ratio of material favoring the advancing and how much that impacts squeeze flash development.

LIST OF REFERENCES

[1] H. Z. Yu, "Additive Friction Stir Deposition," *Additive Friction Stir Deposition*, pp. 1–333, Jan. 2022, doi: 10.1016/C2020-0-01505-7.

[2] "Faster – MELD Manufacturing." Accessed: Mar. 29, 2023. [Online]. Available: https://www.meldmanufacturing.com/faster/

[3] H. Z. Yu and R. S. Mishra, "Additive friction stir deposition: a deformation processing route to metal additive manufacturing," *Mater Res Lett*, vol. 9, no. 2, pp. 71–83, Feb. 2021, doi: 10.1080/21663831.2020.1847211.

[4] H. Z. Yu *et al.*, "Non-beam-based metal additive manufacturing enabled by additive friction stir deposition," *Scr Mater*, vol. 153, pp. 122–130, Aug. 2018, doi: 10.1016/j.scriptamat.2018.03.025.

[5] R. S. Mishra and Z. Y. Ma, "Friction stir welding and processing," Aug. 31, 2005. doi: 10.1016/j.mser.2005.07.001.

[6] X. Wang, Y. Gao, M. McDonnell, and Z. Feng, "On the solid-state-bonding mechanism in friction stir welding," *Extreme Mech Lett*, vol. 37, May 2020, doi: 10.1016/j.eml.2020.100727.

[7] H. Schmidt, J. Hattel, and J. Wert, "An analytical model for the heat generation in friction stir welding," *Model Simul Mat Sci Eng*, vol. 12, no. 1, pp. 143–157, Jan. 2004, doi: 10.1088/0965-0393/12/1/013.

[8] K. J. Quintana and J. L. Silveira, "Mechanistic models for the forces in FSW of aluminum alloy 5052-H34," *International Journal of Advanced Manufacturing Technology*, vol. 96, no. 9–12, pp. 3993–4008, Jun. 2018, doi: 10.1007/s00170-018-1859-3.

[9] M. Mijajlović and D. Milčić, "Heat Generation During Friction Stir Welding Process," 2009. [Online]. Available: https://www.researchgate.net/publication/265010421

[10] A. Arora, R. Nandan, A. P. Reynolds, and T. DebRoy, "Torque, power requirement and stir zone geometry in friction stir welding through modeling and

experiments," *Scr Mater*, vol. 60, no. 1, pp. 13–16, Jan. 2009, doi: 10.1016/j.scriptamat.2008.08.015.

[11] H. Schmidt and J. Hattel, "A local model for the thermomechanical conditions in friction stir welding," *Model Simul Mat Sci Eng*, vol. 13, no. 1, pp. 77–93, Jan. 2005, doi: 10.1088/0965-0393/13/1/006.

[12] R. Nandan, G. G. Roy, T. J. Lienert, and T. Debroy, "Three-dimensional heat and material flow during friction stir welding of mild steel," *Acta Mater*, vol. 55, no. 3, pp. 883–895, Feb. 2007, doi: 10.1016/j.actamat.2006.09.009.

[13] D. G. Andrade, C. Leitão, N. Dialami, M. Chiumenti, and D. M. Rodrigues, "Modelling torque and temperature in friction stir welding of aluminium alloys," *Int J Mech Sci*, vol. 182, Sep. 2020, doi: 10.1016/j.ijmecsci.2020.105725.

[14] S. S. Babu, J. Livingston, and J. C. Lippold, "Physical simulation of deformation and microstructure evolution during friction stir processing of Ti-6Al-4V alloy," *Metall Mater Trans A Phys Metall Mater Sci*, vol. 44, no. 8, pp. 3577–3591, Aug. 2013, doi: 10.1007/s11661-013-1782-z.

[15] A. Arora, Z. Zhang, A. De, and T. DebRoy, "Strains and strain rates during friction stir welding," *Scr Mater*, vol. 61, no. 9, pp. 863–866, Nov. 2009, doi: 10.1016/j.scriptamat.2009.07.015.

[16] M. Abbasi, A. Abdollahzadeh, H. Omidvar, B. Bagheri, and M. Rezaei, "Incorporation of SiC particles in FS welded zone of AZ31 Mg alloy to improve the mechanical properties and corrosion resistance."

[17] D. Storjohann, O. M. Barabash, S. S. Babu, S. A. David, P. S. Sklad, and E. E. Bloom, "Fusion and Friction Stir Welding of Aluminum-Metal-Matrix Composites."

[18] Gang Chen, Kai Wu, Yu Wang, Zhi-Xiong Zhu, Pan Nie, and Feng-Feng Hu, "Effect of rotational speed and feed rate on microstructure and mechanical properties of 6061aluminum alloy manufactured by additive friction stir deposition".

[19] K. Anderson-Wedge *et al.*, “Characterization of the fatigue behavior of additive friction stir-deposition AA2219,” *Int J Fatigue*, vol. 142, Jan. 2021, doi: 10.1016/j.ijfatigue.2020.105951.

[20] D. Z. Avery *et al.*, “Evaluation of Microstructure and Mechanical Properties of Al-Zn-Mg-Cu Alloy Repaired via Additive Friction Stir Deposition,” *J Eng Mater Technol*, vol. 144, no. 3, Jul. 2022, doi: 10.1115/1.4052816.

[21] H. Ghadimi *et al.*, “Hardness Distribution of Al2050 Parts Fabricated Using Additive Friction Stir Deposition,” *Materials*, vol. 16, no. 3, Feb. 2023, doi: 10.3390/ma16031278.

[22] M. E. J. Perry, R. J. Griffiths, D. Garcia, J. M. Sietins, Y. Zhu, and H. Z. Yu, “Morphological and microstructural investigation of the non-planar interface formed in solid-state metal additive manufacturing by additive friction stir deposition,” *Addit Manuf*, vol. 35, Oct. 2020, doi: 10.1016/j.addma.2020.101293.

[23] M. E. J. Perry *et al.*, “Tracing plastic deformation path and concurrent grain refinement during additive friction stir deposition,” *Materialia (Oxf)*, vol. 18, Aug. 2021, doi: 10.1016/j.mtla.2021.101159.

[24] C. J. T. Mason *et al.*, “Process-Structure-Property Relations for As-Deposited Solid-State Additively Manufactured High-Strength Aluminum Alloy,” Feb. 2021. Accessed: Jan. 31, 2023. [Online]. Available: https://www.osti.gov/pages/biblio/1781824

[25] J. K. Yoder, R. J. Griffiths, and H. Z. Yu, “Deformation-based additive manufacturing of 7075 aluminum with wrought-like mechanical properties,” *Mater Des*, vol. 198, Jan. 2021, doi: 10.1016/J.MATDES.2020.109288.

[26] P. Agrawal *et al.*, “Processing-structure-property correlation in additive friction stir deposited Ti-6Al-4V alloy from recycled metal chips,” *Addit Manuf*, vol. 47, Nov. 2021, doi: 10.1016/j.addma.2021.102259.

[27] B. J. Phillips *et al.*, “Microstructure-deformation relationship of additive friction stir-deposition Al–Mg–Si,” *Materialia (Oxf)*, vol. 7, p. 100387, Sep. 2019, doi: 10.1016/J.MTLA.2019.100387.

[28] G. R. Merritt, M. B. Williams, P. G. Allison, J. B. Jordon, T. W. Rushing, and C. A. Cousin, “Closed-Loop Temperature and Force Control of Additive Friction Stir Deposition,” *Journal of Manufacturing and Materials Processing*, vol. 6, no. 5, Oct. 2022, doi: 10.3390/jmmp6050092.

[29] J. Glenn, L. Dean, A. Wright, and Y. Hovanski, “Closed-Loop PID Temperature Control of Additive Friction Stir Deposition,” pp. 15–25, 2023, doi: 10.1007/978-3-031-22661-8_2.

[30] T. Schmitz *et al.*, “Embedded QR code for part authentication in additive friction stir deposition,” *Manuf Lett*, vol. 35, pp. 16–19, Jan. 2023, doi: 10.1016/J.MFGLET.2022.11.003.

[31] J. Kincaid, R. Zameroski, T. No, J. Bohling, B. Compton, and T. Schmitz, “Hybrid Manufacturing: Combining Additive Friction Stir Deposition, Metrology, and Machining,” pp. 3–13, 2023, doi: 10.1007/978-3-031-22661-8_1.

[32] R. J. Griffiths *et al.*, “Solid-state additive manufacturing of aluminum and copper using additive friction stir deposition: Process-microstructure linkages,” *Materialia (Oxf)*, vol. 15, Mar. 2021, doi: 10.1016/j.mtla.2020.100967.

[33] B. J. Phillips *et al.*, “Effect of parallel deposition path and interface material flow on resulting microstructure and tensile behavior of Al-Mg-Si alloy fabricated by additive friction stir deposition,” *J Mater Process Technol*, vol. 295, p. 117169, Sep. 2021, doi: 10.1016/J.JMATPROTEC.2021.117169.

[34] D. Garcia *et al.*, “In situ investigation into temperature evolution and heat generation during additive friction stir deposition: A comparative study of Cu and Al-Mg-Si,” *Addit Manuf*, vol. 34, Aug. 2020, doi: 10.1016/j.addma.2020.101386.

[35] B. J. Phillips, C. Jacob Williamson, R. P. Kinser, J. Brian Jordon, K. J. Doherty, and P. G. Allison, “Microstructural and mechanical characterization of additive friction stir-deposition of aluminum alloy 5083 effect of lubrication on material anisotropy,” *Materials*, vol. 14, no. 21, Nov. 2021, doi: 10.3390/ma14216732.

[36] L. P. Cahalan *et al.*, “Parametric Investigation of Parallel Deposition Passes on the Microstructure and Mechanical Properties of 7075 Aluminum Alloy Processed

with Additive Friction Stir Deposition," *Applied Sciences*, vol. 14, no. 1, p. 457, Jan. 2024, doi: 10.3390/app14010457.

[37] G. G. Stubblefield, K. Fraser, B. J. Phillips, J. B. Jordon, and P. G. Allison, "A meshfree computational framework for the numerical simulation of the solid-state additive manufacturing process, additive friction stir-deposition (AFS-D)," *Mater Des*, vol. 202, Apr. 2021, doi: 10.1016/j.matdes.2021.109514.

[38] G. G. Stubblefield *et al.*, "Elucidating the influence of temperature and strain rate on the mechanics of AFS-D through a combined experimental and computational approach," *J Mater Process Technol*, vol. 305, Jul. 2022, doi: 10.1016/j.jmatprotec.2022.117593.

[39] K. C. Kincaid, D. W. MacPhee, G. Stubblefield, J. B. Jordon, T. W. Rushing, and P. Allison, "A Finite Volume Framework for the Simulation of Additive Friction Stir Deposition," *J Eng Mater Technol*, pp. 1–30, Jul. 2023, doi: 10.1115/1.4056642.

[40] K. C. Kincaid, M. B. Williams, D. W. Macphee, J. B. Jordon, T. W. Rushing, and P. G. Allison, "A Finite Volume Method for Simulating Multi-layer Depositions in Solid-State Additive Manufacturing." [Online]. Available: https://ssrn.com/abstract=4333465

[41] T. Shi, J. Wu, M. Ma, E. Charles, and T. Schmitz, "AFSD-Nets: A Physics-informed Machine Learning Model for Predicting the Temperature Evolution During Additive Friction Stir Deposition," *SSRN Electronic Journal*, 2023, doi: 10.2139/ssrn.4627557.

[42] T. Z. Shi *et al.*, "AFSD-Physics: Exploring the governing equations of temperature evolution during additive friction stir deposition by a human-AI teaming approach", doi: 10.13140/RG.2.2.34468.65929.

[43] A. Roschli *et al.*, "Designing for Big Area Additive Manufacturing," *Addit Manuf*, vol. 25, no. C, pp. 275–285, Nov. 2018, doi: 10.1016/J.ADDMA.2018.11.006.

[44] A. Roschli, M. Borish, A. Barnes, T. Feldhausen, P. Wang, and E. MacDonald, *Motion and Path Planning for Additive Manufacturing*. Elsevier, 2023.

[45] J. C. Steuben, A. P. Iliopoulos, and J. G. Michopoulos, “Implicit slicing for functionally tailored additive manufacturing,” *Proceedings of the ASME Design Engineering Technical Conference*, vol. 1A-2016, 2016, doi: 10.1115/DETC2016-59638.

[46] C. Wade and M. Borish, “Hybrid Curve Fitting For Reducing Motion Commands In Object Construction.” [Online]. Available: http://energy.gov/downloads/doe-public-access-plan

[47] R. L. S. Drysdale, G. Rote, and A. Sturm, “Approximation of an Open Polygonal Curve with a Minimum Number of Circular Arcs and Biarcs.”

[48] P. Huang, C. C. L. Wang, and Y. Chen, “Intersection-free and topologically faithful slicing of implicit solid,” *J Comput Inf Sci Eng*, vol. 13, no. 2, Jun. 2013, doi: 10.1115/1.4024067/371419.

[49] A. B. Forbes, “Least squares best fit geometric elements,” Springer US, 1990. doi: 10.1007/978-1-4899-3442-0_28.

[50] D. Umbach and K. N. Jones, “A Few Methods for Fitting Circles to Data,” 2000.

[51] M. K. Yeung and D. J. Walton, “Curve fitting with arc splines for NC tool path generation,” 1994.

[52] M. Yang and C. Kim, “A CAD/CAM System for Precision Cams with Three CNC Interpolation Methods,” 1994.

[53] M.-Y. Yang, T.-Y. Shon, T.-M. Lee, and T.-M. Lee, “Cam profile machining by triarc curve fitting,” *Int J Prod Res*, vol. 36, no. 7, pp. 1767–1778, Jul. 1998, doi: 10.1080/002075498192959.

[54] Z. Wu and T. Liu, “A double circular arc fitting algorithm for CNC machining of non-uniform scroll components,” *International Journal of Advanced Manufacturing Technology*, vol. 104, no. 9–12, pp. 4485–4495, Oct. 2019, doi: 10.1007/s00170-019-04304-x.

[55] J.-H. Horng and J. T. Li, “A dynamic programming approach for fitting digital planar curves with line segments and circular arcs,” 2001, [Online]. Available: www.elsevier.nl/locate/patrec

[56] J. G. Dunham, “Optimum Uniform Piecewise Linear Approximation of Planar Curves,” 1986.

[57] E. Bodansky and A. Gribov, “Approximation of a Polyline with a Sequence of Geometric Primitives,” 2006.

[58] J. Jiang and Y. Ma, “Path Planning Strategies to Optimize Accuracy, Quality, Build Time and Material Use in Additive Manufacturing: A Review,” *Micromachines 2020, Vol. 11, Page 633*, vol. 11, no. 7, p. 633, Jun. 2020, doi: 10.3390/MI11070633.

[59] Y. an Jin, Y. He, J. zhong Fu, W. feng Gan, and Z. wei Lin, “Optimization of tool-path generation for material extrusion-based additive manufacturing technology,” *Addit Manuf*, vol. 1, pp. 32–47, Oct. 2014, doi: 10.1016/j.addma.2014.08.004.

[60] Y. Jin, Y. He, and J. Du, “A novel path planning methodology for extrusion-based additive manufacturing of thin-walled parts,” *https://doi.org/10.1080/0951192X.2017.1307526*, vol. 30, no. 12, pp. 1301–1315, Dec. 2017, doi: 10.1080/0951192X.2017.1307526.

[61] Y. Jin, J. Du, Z. Ma, A. Liu, and Y. He, “An optimization approach for path planning of high-quality and uniform additive manufacturing,” *International Journal of Advanced Manufacturing Technology*, vol. 92, no. 1–4, pp. 651–662, Sep. 2017, doi: 10.1007/s00170-017-0207-3.

[62] D. Ding, Z. Pan, D. Cuiuri, and H. Li, “A tool-path generation strategy for wire and arc additive manufacturing,” *International Journal of Advanced Manufacturing Technology*, vol. 73, pp. 173–183, 2014, doi: 10.1007/s00170-014-5808-5.

[63] D. Ding, L. Yuan, R. Huang, Y. Jiang, X. Wang, and Z. Pan, “Corner path optimization strategy for wire arc additive manufacturing of gap-free shapes,” *J Manuf Process*, vol. 85, pp. 683–694, Jan. 2023, doi: 10.1016/j.jmapro.2022.12.014.

[64] K. N. Krishnan, “On the formation of onion rings in friction stir welds,” 2002. [Online]. Available: www.mecheng.

[65] Z. W. Chen and S. Cui, “On the forming mechanism of banded structures in aluminium alloy friction stir welds,” *Scr Mater*, vol. 58, no. 5, pp. 417–420, Mar. 2008, doi: 10.1016/j.scriptamat.2007.10.026.

[66] H. Ghadimi, M. Talachian, H. Ding, S. Emanet, and S. Guo, “The Effects of Layer Thickness on the Mechanical Properties of Additive Friction Stir Deposition-Fabricated Aluminum Alloy 6061 Parts,” *Metals (Basel)*, vol. 14, no. 1, p. 101, Jan. 2024, doi: 10.3390/met14010101.

[67] W. Gong *et al.*, “Influence of Preheating Temperature on the Microstructure and Mechanical Properties of 6061/TA1 Composite Plates Fabricated by AFSD,” *Materials*, vol. 16, no. 17, Sep. 2023, doi: 10.3390/ma16176018.

[68] L. P. Martin, A. Luccitti, and M. Walluk, “Repair of aluminum 6061 plate by additive friction stir deposition”, doi: 10.1007/s00170-021-07953-z/Published.

[69] J. K. Yoder, H. Z. Yu, W. T. Reynolds, W. Cai, L. Li, and V. Blacksburg, “Origins of Embrittlement of an Al-Zn-Mg-Cu Alloy Post Additive Friction Stir Deposition,” 2022.

[70] H. Ding *et al.*, “Peak microhardness recovery via T6 heat treatment with extremely soft annealed Al7075 feedstock in additive friction stir deposition,” *Journal of Materials Research and Technology*, vol. 32, pp. 2993–3003, Sep. 2024, doi: 10.1016/j.jmrt.2024.08.132.

[71] W. D. Hartley *et al.*, “Solid-state cladding on thin automotive sheet metals enabled by additive friction stir deposition,” *J Mater Process Technol*, vol. 291, May 2021, doi: 10.1016/j.jmatprotec.2021.117045.

[72] Y. Xiong *et al.*, “Process planning for adaptive contour parallel toolpath in additive manufacturing with variable bead width,” *International Journal of Advanced Manufacturing Technology*, vol. 105, no. 10, pp. 4159–4170, Dec. 2019, doi: 10.1007/s00170-019-03954-1.

[73] Z. Hu, X. Qin, Y. Li, J. Yuan, and Q. Wu, “Multi-bead overlapping model with varying cross-section profile for robotic GMAW-based additive manufacturing,” *J*

Intell Manuf, vol. 31, no. 5, pp. 1133–1147, Jun. 2020, doi: 10.1007/s10845-019-01501-z.

[74] J. Burdick, “Image of a raftlike trial scale build produced on the Jointless Hull Subsection Tool using AFSD,” Detroit MI.

[75] H. S. Valdivieso, “Polyline defined NC trajectories parametrization. A compact analysis and solution focused on 3D Printing,” Aug. 2018, [Online]. Available: http://arxiv.org/abs/1808.01831

[76] R. Johnson, *Modern geometry: An Elementary Treatise on the Geometry of the Triangle and the Circle*. Cambridge, Massachusetts: The Riverside Press Cambridge, 1929. Accessed: Feb. 18, 2025. [Online]. Available: https://babel.hathitrust.org/cgi/pt?id=wu.89043163211&seq=109

[77] A. Roschli *et al.*, “ORNL Slicer 2 - Open Source Copyright,” May 06, 2024, *USDOE Office of Energy Efficiency and Renewable Energy (EERE), Energy Efficiency Office. Advanced Materials & Manufacturing Technologies Office (AMMTO)*. Accessed: Mar. 11, 2025. [Online]. Available: https://www.osti.gov/doecode/biblio/97742

APPENDICES

A: Coordinate points for low resolution fish shaped test part:

This table contains a list of 3D coordinate points for the fish shaped test part described in chapter 4.

Table 10: Coordinates points for fish shaped test part.

X (*mm*)	**Y** (*mm*)	**Z** (*mm*)
0.0000	0.0000	3.8250
46.1270	0.0000	3.8250
60.1749	20.0609	3.8250
61.3147	21.6878	3.8250
112.3122	21.6878	3.8250
126.3602	1.6269	3.8250
127.5000	0.0000	3.8250
203.9924	0.0000	3.8250
210.6606	0.4361	3.8250
217.1988	1.7366	3.8250
223.5126	3.8786	3.8250
229.5000	6.8340	3.8250
235.0437	10.5366	3.8250
240.0621	14.9379	3.8250
244.4634	19.9563	3.8250
248.1686	25.5000	3.8250
251.1164	31.4798	3.8250
253.2635	37.8012	3.8250
254.5640	44.3394	3.8250
255.0000	51.0051	3.8250
255.0000	127.5000	3.8250
249.0432	134.0382	3.8250
242.4693	139.9517	3.8250
235.3421	145.1894	3.8250
227.7252	149.6978	3.8250
219.7106	153.4259	3.8250
211.3568	156.3431	3.8250
202.7582	158.4213	3.8250
193.9989	159.6377	3.8250
185.1581	159.9794	3.8250
176.3402	159.4464	3.8250
167.6013	158.0388	3.8250
159.0435	155.7770	3.8250
150.7611	152.6787	3.8250
142.8281	148.7772	3.8250

Table 10: Continued.

135.3158	144.1107	3.8250
128.3033	138.7200	3.8250
121.8569	132.6561	3.8250
116.0429	125.9930	3.8250
110.9123	118.7790	3.8250
107.1051	113.6663	3.8250
102.6018	109.1451	3.8250
97.4942	105.3074	3.8250
91.8969	102.2423	3.8250
85.9172	100.0034	3.8250
79.6748	98.6442	3.8250
73.3176	98.1878	3.8250
47.8125	98.1878	3.8250
38.9666	113.5082	3.8250
38.2500	114.7500	3.8250
0.0000	114.7500	3.8250
0.0000	0.0000	3.8250

B: sample arc fitting function code written in MATLAB

This sections contains sample code written for the purposes of fitting arcs to coordinate data.

Begin code

```
function [Gc,Gc_crnr,Gdata_arc,Gdata_line] = GeomID(Coord,pickups, r_max, L_max,
line_ang , corn_ang, err_contrib_max, err_lim,
Arc_Re0_num_err_tol,Arc_Re0_Max_iter)
% Identify lines, circular segments & corners from a list of ordered points
% This function takes input of 3 equal length vectors of ordered [X, Y, Z]
% coordinates and outputs list of grouped coordinates by circular arc,
% lines and corners


% Check for pickups as input
if size(Coord,2) < 3
   error('number of columns in coordinate array is of an unexpected value (m>3)');
end
```

```
Gc = NaN(length(Coord),1);
if exist('pickups','var')
   Gc = NaN(length(Coord),1);
   Gc(pickups==true) = 0;
end
Gc(1) = 0;

if ~exist('Arc_Re0_num_err_tol','var')
   Arc_Re0_num_err_tol = 10^-9;
end
if ~exist('Arc_Re0_Max_iter','var')
   Arc_Re0_Max_iter = 25;
end
if ~exist('err_contrib_max','var')
   err_contrib_max = 0.00005;
end
if ~exist('r_max','var')
   r_max = 100;
end
if ~exist('L_max','var')
   L_max = 1.995;
end
if ~exist('err_lim','var')
   err_lim = 0.0001;
end
if ~exist('line_ang','var')
   line_ang = 179.5;
end
```

```
if ~exist('corn_ang','var')
   corn_ang = 95;
end

% Geometric ID

% Take coordinates out for readability
X = Coord(:,1);
Y = Coord(:,2);
Z = Coord(:,3);

% Determine layer bounds
LayerID = 0;
n = 2;
h = 0.080;
for i = 2:length(Z)
   if Z(i) ~= Z(i-1) && mod(Z(i),h) == 0
      LayerID(n) = i;
      n = n + 1;
   end
   %P_LocID(i,1) = n-1;
end
LayerID(n) = length(Z);

% Initialize main loop
Gc_crnr = false(length(Gc),1);
Gdata_arc = zeros(1,6);
Gdata_line = zeros(1,2);
j1 = 1; % Current Gdata_arc row indice
```

```
j2 = 1; % Current Gdata_line row indice
i = 2;
n = size(Coord,1);
% Main loop.
% Length of C vector must be greater than
for k=2:(length(LayerID))
   nl = LayerID(k);
   while i < nl%-1
      %  Colinear?
      L1 = sqrt((X(i-1)-X(i))^2 + (Y(i-1)-Y(i))^2); % Length from point i-1 to i  + (Z(i-1)-
Z(i))^2
      L2 = sqrt((X(i+1)-X(i))^2 + (Y(i+1)-Y(i))^2); % Length from point i to i+1  +
(Z(i+1)-Z(i))^2
      L3 = sqrt((X(i+1)-X(i-1))^2 + (Y(i+1)-Y(i-1))^2); % Length from point i-1 to i+1  +
(Z(i+1)-Z(i-1))^2
      angle = acosd((L1^2+L2^2-L3^2)/(2*L1*L2));
      % Straight line?
      if angle>=line_ang || L1>=L_max || L2>=L_max || Gc(i-1)==0 && Gc(i+1)==0 %
Change these values to default by input parser
         Gc(i) = -j2;
         i = i+1;
         Gdata_line(j2,:) = [L1 mod(atan2d(Y(i)-Y(i-1),X(i)-X(i-1))+360,360)];
         j2 = j2+1;
      % Corner?
      elseif angle<=corn_ang || isnan(angle)
         Gc_crnr(i) = true;
         Gc(i) = -j2;
         Gdata_line(j2,:) = [L1 mod(atan2d(Y(i)-Y(i-1),X(i)-X(i-1))+360,360)];
         j2 = j2+1;
```

```
        i = i+1;
    % arc?
    elseif i+2<nl
        % 3 into 4 point arc test
        [r, a, b, errT] = Arc_Fit(Coord((i-1):(i+1),1:3));
        err = (r-sqrt((X(i+2) - a)^2 + (Y(i+2) - b)^2))^2;
        L4 = sqrt((X(i+2)-X(i+1))^2 + (Y(i+2)-Y(i+1))^2); % Length from point i+1 to
i+2
        [r4, ~, ~, errT4] = Arc_Fit(Coord((i-1):(i+2),1:3));
        if err>err_contrib_max || L4>L3 % must be a corner (edge case: shallow corner
with line after that somehow perfectly matches up with arc fit)
            Gc_crnr(i) = true;
            Gc(i) = -j2;
            Gdata_line(j2,:) = [L1 mod(atan2d(Y(i)-Y(i-1),X(i)-X(i-1))+360,360)];
            j2 = j2+1;
            i = i+1;
        elseif r/abs(r)~=r4/abs(r4) || abs((r-r4)/r)*100>8 || errT4>err_contrib_max
            Gc_crnr(i) = true;
            Gc(i) = -j2;
            Gdata_line(j2,:) = [L1 mod(atan2d(Y(i)-Y(i-1),X(i)-X(i-1))+360,360)];
            j2 = j2+1;
            i = i+1;
        elseif r>r_max % radius could be so big that we want it to be a line
            Gc(i) = -j2;
            i = i+1;
            Gdata_line(j2,:) = [L1 mod(atan2d(Y(i)-Y(i-1),X(i)-X(i-1))+360,360)];
            j2 = j2+1;
        else % must be an arc
            Gdata_arc(j1,:) = [r a b errT i-1 i+1];
```

```
            Gc(i) = j1;
            i = i+1;
            Stpr = 0;
            while Stpr == 0 && i+1 < nl
               err = (r-sqrt((X(i+1) - a)^2 + (Y(i+1) - b)^2))^2;
               dist = sqrt((X(i+1)-X(Gdata_arc(j1,5)))^2+(Y(i+1)-Y(Gdata_arc(j1,5)))^2);
               L = sqrt((X(i+1)-X(i))^2 + (Y(i+1)-Y(i))^2);
               [r_next, a_next, b_next, errT_next] =
Arc_Fit(Coord(Gdata_arc(j1,5):Gdata_arc(j1,6)+1,1:3));
               if abs(err)<=err_lim && abs(errT)<=err_lim*0.5 && isnan(Gc(i+1)) &&
dist>10^-9 && L<=L_max && r/abs(r)==r_next/abs(r_next)
                  r = r_next;
                  a = a_next;
                  b = b_next;
                  errT = errT_next;
                  Gdata_arc(j1,:) = [r a b errT Gdata_arc(j1,5) i+1];
                  Gc(i) = j1;
               else
                  Stpr = 1;
                  [XcP, YcP, Ro, Error] =
Arc_Re0(Coord(Gdata_arc(j1,5):Gdata_arc(j1,6),1:3),Gdata_arc(j1,1),Gdata_arc(j1,2),G
data_arc(j1,3), Arc_Re0_num_err_tol,Arc_Re0_Max_iter);
                  Gdata_arc(j1,1:4) = [Ro XcP YcP Error];
                  Gc(i) = j1;
                  j1 = j1+1;
               end
               i = i+1;
               if isnan(Gc(i+1))
               end
```

```
            end
        end
    else
        Gc_crnr(i) = true;
        Gc(i) = -j2;
        Gdata_line(j2,:) = [L1 mod(atan2d(Y(i)-Y(i-1),X(i)-X(i-1))+360,360)];
        j2 = j2+1;
        i = i+1;
    end
end
clear r4 a4 b4 errT4
if j1<=size(Gdata_arc,1)
    %[XcP, YcP, Ro, Error] = Arc_Re0(C(Gdata(j,5):Gdata(j,6),1:3),Gdata(j,1));
    %Gdata(j,1:4) = [Ro XcP YcP Error];
    j1 = j1+1;
end
end


Gc(n) = 0;

% Functions
function [R, CpX, CpY, err] = Arc_Fit(Cm)
nf = size(Cm,1); % check number of point
if nf<3
    error('Arc calculation requires a minimum of 3 coordinate points')
end
% Extract X,Y, and Z from coord matrix for readability
Xf = Cm(:,1);
```

```
Yf = Cm(:,2);
% Z = C(:,3);
% Measure process time (order of 1/1000 sec)

% Coefficient calculations from MLS eqn
% A = ;
A1 = 0;
A2 = 0;
for i_f = 1:nf
   A1 = A1 + Xf(i_f)^2;
   A2 = A2 + Xf(i_f);
end
A = nf*A1 - A2^2;

% B = ;
B1 = 0;
B2x = 0;
B2y = 0;
for i_f = 1:nf
   B1 = B1 + Xf(i_f)*Yf(i_f);
   B2x = B2x + Xf(i_f);
   B2y = B2y + Yf(i_f);
end
B = nf*B1 - B2x*B2y;
clear B1 B2x B2y

% C_ = ;
C1 = 0;
C2 = 0;
```

```
for i_f = 1:nf
   C1 = C1 + Yf(i_f)^2;
   C2 = C2 + Yf(i_f);
end
C = nf*C1 - C2^2;

% D = ;
D1 = 0;
D2 = 0;
for i_f = 1:nf
   D1 = D1 + Xf(i_f)*(Yf(i_f)^2);
   D2 = D2 + Xf(i_f)^3;
end
D = 0.5*(nf*D1 - A2*C1 + nf*D2 - A1*A2);
clear D1 D2

% E = ;
E1 = 0;
E2 = 0;
for i_f = 1:nf
   E1 = E1 + Yf(i_f)*(Xf(i_f)^2);
   E2 = E2 + Yf(i_f)^3;
end
E = 0.5*(nf*E1 - C2*A1 + nf*E2 - C1*C2);
clear E1 E2
clear A1 A2 C1 C2

% Calculate approx arc ceterpoint
CpX = (D*C - B*E)/(A*C - B^2); % Centerpoint in X
```

```
CpY = (A*E - B*D)/(A*C - B^2); % Centerpoint in Y

% Calculate approx arc radius
R = 0;
for i_f = 1:nf
   R = R + sqrt((Xf(i_f) - CpX)^2 + (Yf(i_f) - CpY)^2)/nf;
end

% Calculate error (total sum of deviation from point to centerpoint from expected radius)
err = 0;
for i_f = 1:nf
   err = err + (R-sqrt((Xf(i_f) - CpX)^2 + (Yf(i_f) - CpY)^2))^2;
end
end

%
function [CpX, CpY, Ro, err] = Arc_Re0(Cm, R, a , b, err_tol, max_iter)
% Function section 2
if ~exist('err_tol','var')
   err_tol = 1*10^-9;
end
if ~exist('max_iter','var')
   max_iter = 25;
end

Xf = Cm(:,1);
Yf = Cm(:,2);

X1 = Cm(1,1);
```

```
Y1 = Cm(1,2);
X3 = Cm(end,1);
Y3 = Cm(end,2);
L3f = sqrt((X3-X1).^2 + (Y3-Y1).^2);

for abcd = 1:1
   if L3f>=R-2*err_tol && L3f<=R+2*err_tol
      % Find the bisector and set circle center here
   else
      A = [a;
          b];
      err(1:2) = 100;
      n_func = 1;
      while err(n_func)>err_tol
         if n_func>max_iter
            warning('Midpoint solver was unable to resolve solution within prescribed
maximum iterations (%i). Setting center to initial guess. Error=%f, R=%.4f
Coord_1=(%.4f , %.4f , %.4f), Coord_f=(%.4f , %.4f ,
%.4f)',max_iter,err(n_func),R,Cm(1,1),Cm(1,2),Cm(1,3),Cm(end,1),Cm(end,2),Cm(end,
3))
            A = [a, b];
            break
         end
         J = [((A(1)-X1)/sqrt((X1-A(1))^2+(Y1-A(2))^2)) (A(2)-Y1)/sqrt((X1-
A(1))^2+(Y1-A(2))^2) ;
              ((A(1)-X3)/sqrt((X3-A(1))^2+(Y3-A(2))^2)) (A(2)-Y3)/sqrt((X3-
A(1))^2+(Y3-A(2))^2)];
         F = [sqrt((X1-A(1))^2+(Y1-A(2))^2)-R;
             sqrt((X3-A(1))^2+(Y3-A(2))^2)-R];
```

```
        A0 = A;
        A = A0 + -inv(J)*F;
        n_func = n_func+1;
        err(n_func) = (abs(A(1)-A0(1))+abs(A(2)-A0(2)))/2;
      end
      CpX = A(1);
      CpY = A(2);
   end
end

A = 0;
for i_func=1:length(Xf)-2
   A = A + 0.5*((((Xf(i_func)-a).*(Yf(i_func+1)-Yf(i_func)))-((Xf(i_func+1)-
Xf(i_func)).*(Yf(i_func)-b))));
end
sign = A/abs(A);
Ro = R*sign;

end
err = 0;
for i_f = 1:length(Cm)
   err = err + (R-sqrt((Xf(i_f) - CpX)^2 + (Yf(i_f) - CpY)^2))^2;
end
end

end
```

VITA

Joshua Kincaid who hails originally from Cookeville, TN earned a B.S. in Aerospace Engineering from The University of Tennessee in 2021. He then began his PhD work focusing on developing path planning methods for additive friction stir deposition to bridge the gap between part conceptualization to part creation for this solid-state additive manufacturing process. The specific focus was on process parameter optimization for overlapping beads. Upon graduation he accepted a role as an Assistant Professor of Engineering at Wheaton College in Wheaton IL.